



MINISTÉRIO DA CIÊNCIA, TECNOLOGIA, INOVAÇÕES E COMUNICAÇÕES
INSTITUTO NACIONAL DE PESQUISAS ESPACIAIS

sid.inpe.br/mtc-m21c/2018/06.19.17.40-TDI

THE INFLUENCE OF OCEANIC AND ATMOSPHERIC LARGE-SCALE VARIABILITIES ON THE ATLANTIC MERIDIONAL MODE DECADAL TIME SCALE

Sandro Miguel Ferreira Veiga

Doctorate Thesis of the Graduate
Course in Earth System Science,
guided by Dr. Carlos Afonso
Nobre, approved in May 23, 2018.

URL of the original document:

[<http://urlib.net/8JMKD3MGP3W34R/3RATA2H>](http://urlib.net/8JMKD3MGP3W34R/3RATA2H)

INPE
São José dos Campos
2018

PUBLISHED BY:

Instituto Nacional de Pesquisas Espaciais - INPE

Gabinete do Diretor (GBDIR)

Serviço de Informação e Documentação (SESID)

CEP 12.227-010

São José dos Campos - SP - Brasil

Tel.:(012) 3208-6923/7348

E-mail: pubtc@inpe.br

**COMMISSION OF BOARD OF PUBLISHING AND PRESERVATION
OF INPE INTELLECTUAL PRODUCTION (DE/DIR-544):****Chairperson:**

Dr. Marley Cavalcante de Lima Moscati - Centro de Previsão de Tempo e Estudos Climáticos (CGCPT)

Members:

Dra. Carina Barros Mello - Coordenação de Laboratórios Associados (COCTE)

Dr. Alisson Dal Lago - Coordenação-Geral de Ciências Espaciais e Atmosféricas (CGCEA)

Dr. Evandro Albiach Branco - Centro de Ciência do Sistema Terrestre (COCST)

Dr. Evandro Marconi Rocco - Coordenação-Geral de Engenharia e Tecnologia Espacial (CGETE)

Dr. Hermann Johann Heinrich Kux - Coordenação-Geral de Observação da Terra (CGOBT)

Dra. Ieda Del Arco Sanches - Conselho de Pós-Graduação - (CPG)

Silvia Castro Marcelino - Serviço de Informação e Documentação (SESID)

DIGITAL LIBRARY:

Dr. Gerald Jean Francis Banon

Clayton Martins Pereira - Serviço de Informação e Documentação (SESID)

DOCUMENT REVIEW:

Simone Angélica Del Ducca Barbedo - Serviço de Informação e Documentação (SESID)

André Luis Dias Fernandes - Serviço de Informação e Documentação (SESID)

ELECTRONIC EDITING:

Marcelo de Castro Pazos - Serviço de Informação e Documentação (SESID)

Murilo Luiz Silva Gino - Serviço de Informação e Documentação (SESID)



MINISTÉRIO DA CIÊNCIA, TECNOLOGIA, INOVAÇÕES E COMUNICAÇÕES
INSTITUTO NACIONAL DE PESQUISAS ESPACIAIS

sid.inpe.br/mtc-m21c/2018/06.19.17.40-TDI

THE INFLUENCE OF OCEANIC AND ATMOSPHERIC LARGE-SCALE VARIABILITIES ON THE ATLANTIC MERIDIONAL MODE DECADAL TIME SCALE

Sandro Miguel Ferreira Veiga

Doctorate Thesis of the Graduate
Course in Earth System Science,
guided by Dr. Carlos Afonso
Nobre, approved in May 23, 2018.

URL of the original document:

<<http://urlib.net/8JMKD3MGP3W34R/3RATA2H>>

INPE
São José dos Campos
2018

Cataloging in Publication Data

Veiga, Sandro Miguel Ferreira.

V533i The influence of oceanic and atmospheric large-scale variabilities on the Atlantic Meridional Mode decadal time scale / Sandro Miguel Ferreira Veiga. – São José dos Campos : INPE, 2018.

xxiv + 151 p. ; (sid.inpe.br/mtc-m21c/2018/06.19.17.40-TDI)

Thesis (Doctorate in Earth System Science) – Instituto Nacional de Pesquisas Espaciais, São José dos Campos, 2018.

Guiding : Dr. Carlos Afonso Nobre.

1. Atlantic Meridional Mode. 2. Decadal variability. 3. Atlantic Meridional overturning circulation. 4. North Atlantic oscillation. 5. BESM-OA2.5. I.Title.

CDU 551.510.411(261)



Esta obra foi licenciada sob uma Licença [Creative Commons Atribuição-NãoComercial 3.0 Não Adaptada](#).

This work is licensed under a [Creative Commons Attribution-NonCommercial 3.0 Unported License](#).

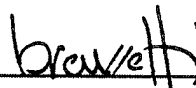
Aluno (a): **Sandro Miguel Ferreira Veiga**

Título: **"THE INFLUENCE OF OCEANIC AND ATMOSPHERIC LARGE-SCALE VARIABILITIES ON THE ATLANTIC MERIDIONAL MODE DECADEAL TIME SCALE".**

Aprovado (a) pela Banca Examinadora
em cumprimento ao requisito exigido para
obtenção do Título de *Doutor(a)* em

Ciência do Sistema Terrestre

Dr. João Antônio Lorenzetti



Presidente / INPE / SJCampos - SP

() Participação por Video - Conferência

Dr. Carlos Afonso Nobre



Orientador(a) / INPE / São José dos Campos - SP

() Participação por Video - Conferência

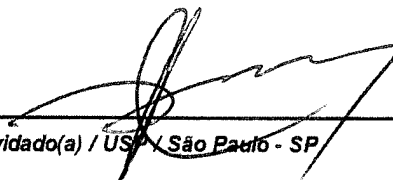
Dr. Paulo Nobre



Membro da Banca / INPE / Cachoeira Paulista - SP

() Participação por Video - Conferência

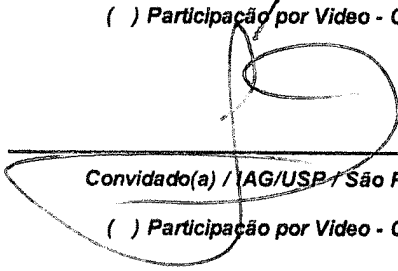
Dr. Edmo José Dias Campos



Convidado(a) / USP / São Paulo - SP

() Participação por Video - Conferência

Dr. Tércio Ambrizzi



Convidado(a) / AG/USP / São Paulo - SP

() Participação por Video - Conferência

Este trabalho foi aprovado por:

() maioria simples

(✓) unanimidade

“Look again at that dot. That's here. That's home. That's us.”

-Carl Sagan, Pale Blue Dot: A Vision of the Human Future in Space-

(In Portuguese)

Em memória do meu Pai, que sempre incentivou-me a estudar.

À minha Mãe e minha irmã, que de longe apoiaram-me incondicionalmente.

À minha esposa, pelo seu amor e valioso apoio.

A meu filho, que veio dar-me uma motivação extra.

AKNOWLEDGMENTS

(In Portuguese):

Agradecimentos

Agradeço ao Doutor Carlos Nobre pela sua orientação no decorrer deste projeto e pela oportunidade de trabalhar neste tópico. Agradeço ao Doutor Paulo Nobre pela orientação e disponibilidade para importantes discussões sobre diversos assuntos que foram surgindo ao longo deste trabalho. Quero agradecer ao Doutor Emanuel Giarolla pelo apoio e pelas discussões sobre várias dificuldades técnicas.

Agradeço ao Doutor João Corte-Real por todo apoio e incentivo para vir fazer o doutorado no Brasil.

Agradeço o apoio e boa convivência que me foi proporcionado pelo grupo "BESM", nomeadamente Manoel Baptista, Helena Soares, André Lanfer, Marcus Bottino.

Gostava de reconhecer o excelente ambiente de trabalho e convívio proporcionado pelos amigos do Centro de Ciência do Sistema Terrestre (CCST), nomeadamente pela minha turma de 2013.

Agradeço à Coordenação de Aperfeiçoamento de Pessoal de Nível Superior (CAPES) pelo financiamento da minha bolsa de doutorado e pela oportunidade de fazer pesquisa no Brasil.

Ao CCST e ao Instituto Nacional de Pesquisas Espaciais (INPE), agradeço a boa recepção e hospitalidade durante toda a minha vida de inpeano.

Por fim, agradeço profundamente aos meus pais e minha irmã pelo apoio constante e incondicional; e todo o valioso apoio e motivação dado pela minha esposa durante estes anos. Agradeço a todos os meus familiares e amigos.

ABSTRACT

The Atlantic Meridional Mode (AMM) is a prominent coupled ocean-atmosphere mode of variability that manifests itself in the tropical Atlantic, mainly in the boreal spring although in some years it maintains itself active throughout the boreal summer and fall. The AMM impacts in continental land regions are due to its modulation of the Intertropical Convergence Zone, which tends to be located over the warmer hemisphere during the AMM peak phase. It also influences the conditions in the Atlantic hurricane Main Development Region. Many AMM features remain to be understood, from what determines its dominant decadal variability to the complex physical processes that sustain it. In this study, it is investigated the influence of the Atlantic Ocean variability and atmospheric large-scale variabilities on the dominant decadal periodicity that characterizes the AMM. Since we are interested in investigating the link between AMM and different phenomena at decadal time scale, observational and reanalysis datasets consisting of long record are used in this study. Through statistical analysis, it is shown that the sea surface temperature decadal variability in the Atlantic Ocean is linked to the AMM by the AMO. The AMO precedes the AMM. To further understand the ocean influence, the ocean heat content (0–300m) decadal variability is analyzed. The results show that there is no significant relationship between the ocean heat content and the AMM. Regarding the atmospheric large-scale variabilities, it is concluded that El Niño-Southern Oscillation and the Interdecadal Pacific Oscillation do not significantly impact the AMM on decadal time scale. In this work is shown that the NAO is an important external forcing on the AMM, both at interannual and decadal time scale. In order to reinforce the conclusions, data from CMIP5 models are also used. The new version of the Brazilian Earth System Model (BESM-OA2.5) is one of the models used. Therefore the evaluation of its historical simulation is presented. The last topic studied is related to the potential changes of the AMM in a perturbed climate scenario. To this purpose, the idealized $4\times\text{CO}_2$ experiments performed by four models are used. Two models show that the AMM maintains its spatio-temporal pattern under a perturbed climate scenario, while the Atlantic Meridional Overturning Circulation changes profoundly its structure.

Key-words: Atlantic Meridional Mode, Decadal variability, Atlantic Meridional Overturning Circulation, North Atlantic Oscillation, BESM-OA2.5

A INFLUÊNCIA DE VARIABILIDADES OCEÂNICAS E ATMOSFÉRICAS DE LARGA-ESCALA NO MODO MERIDIONAL DO ATLÂNTICO À ESCALA DECENAL

RESUMO

O Modo Meridional do Atlântico (MMA) é um modo de variabilidade importante do sistema acoplado oceano-atmosfera que se manifesta no Atlântico tropical, principalmente na primavera boreal, embora em alguns anos se mantenha ativo durante o verão e outono boreal. Durante sua fase de pico, o MMA impacta as regiões continentais devido à sua modulação da Zona de Convergência Intertropical, que tende a estar localizada sobre o hemisfério com águas mais quentes e também por sua influência nas condições da Região Principal de Desenvolvimento de furacões do Atlântico. Muitas características da MMA ainda carecem de compreensão, desde a razão que determina sua dominante variabilidade decenal até aos complexos processos físicos que o sustentam ativo. Neste estudo, investigou-se a influência da variabilidade do Oceano Atlântico e das variabilidades atmosféricas de larga-escala na periodicidade predominantemente decenal que caracteriza o MMA. Uma vez que o interesse se prende em investigar as relações entre o MMA e diferentes fenômenos na escala decenal, são utilizados neste estudo dados observacionais e de Reanálise com longo registro. Através de análise estatística, mostra-se que a variabilidade decenal da temperatura da superfície do mar no Oceano Atlântico está ligada à MMA pela Oscilação Multidecenal do Atlântico (OMA). A OMA precede o MMA. Para entender melhor a influência do oceano, a variabilidade decenal do conteúdo de calor oceânico (0 a 300m) é analisada. Os resultados mostram que não há relação significativa entre a variabilidade do conteúdo de calor oceânico e o MMA. Em relação às variabilidades atmosféricas de larga-escala, conclui-se que o El Niño-Oscilação do Sul e a Oscilação Interdecenal do Pacífico não afetam significativamente o MMA na escala de tempo decenal. Neste trabalho é mostrado que a Oscilação do Atlântico Norte é um forçamento externo importante no MMA, tanto na escala de tempo interanual quanto decenal. Para reforçar as conclusões, mesmas análises são efetuadas utilizando dados de modelos do CMIP5. Dentre esses modelos é utilizada a nova versão do Modelo Brasileiro do Sistema Terrestre (BESM-OA2.5). Dedicar-se um capítulo para a avaliação da rodada histórica do BESM-OA2.5. O último tópico estudado está

relacionado às possíveis mudanças do MMA em um cenário climático perturbado. Para este propósito são utilizados experimentos $4\times\text{CO}_2$ realizados por quatro modelos. Dois modelos mostram que o MMA mantém seu padrão espaço-temporal sob um cenário climático perturbado, no qual a Circulação Meridional de Revolvimento do Atlântico altera profundamente sua estrutura.

Palavras-chave: Modo Meridional do Atlântico, Variabilidade decenal, Circulação Meridional de Revolvimento do Atlântico, Oscilação do Atlântico Norte, BESM-OA2.5

LIST OF FIGURES

Figure 1.1 - Projected population growth for the year 2050.....	3
Figure 2.1 - The Atlantic Meridional Mode.....	10
Figure 2.2 - The description of the AMM physical mechanism based on the WES positive feedback process during an AMM positive phase event..	13
Figure 3.1 - The scheme of principal simulations carried out by BESM-OA2.5 using different forcing conditions according to CMIP5 protocols.	30
Figure 3.2 - NAO normalized index for DJFM based on dataset obtained from Hurrell, (2017).	32
Figure 4.1 - The Atlantic Meridional Overturning Circulation simulated by BESM-OA2.5.	41
Figure 4.2 - The leading EOF modes of the detrended monthly SST anomalies over the Tropical Pacific region (30° S–30° N; 240°–70° W).....	43
Figure 4.3 - Spatial maps with the monthly correlation between Niño-3 index and global SST anomalies.	44
Figure 4.4 - Spatial maps with the correlation between SST and precipitation (seasonal average DJF) over the South Ocean (40° S–10° N; 70° W–20° E).	46
Figure 4.5 - The leading EOF modes of the boreal winter (DJF) seasonal averaged SLP anomalies for the Euro-Atlantic region (20°–80° N; 100° W–30° E).	47
Figure 4.6 - One-point correlation map for North Pacific.	49
Figure 4.7 - The second and third EOF modes of the monthly mean 500 hPa geopotential height field for the Southern Hemisphere (20°–90° S).	50
Figure 4.8 - The leading EOF modes of the monthly mean 500 hPa geopotential height fields for the Southern Hemisphere (20°–90° S).	51
Figure 4.9 - The EOF modes of the detrended monthly SST anomalies for the North Pacific (20°–60° N).....	53
Figure 4.10 - The Principal Component time series of the PDO modes.....	54
Figure 5.1 - The Atlantic Meridional Mode simulated by BESM-OA2.5.	61
Figure 5.2 - The Atlantic Meridional Mode simulated by CanESM2.	63
Figure 5.3 - The Atlantic Meridional Mode simulated by HadGEM2-ES.	65

Figure 5.4 - The Atlantic Meridional Mode simulated by MPI-ESM-MR.....	67
Figure 6.1 - Relationship between AMM-SST and SST.	73
Figure 6.2 - Relationship between AMM-SST and OHC300.....	76
Figure 6.3 - Relationship between SST and OHC300.	79
Figure 6.4 - Scatter plot using as coordinates normalized NAO and Niño3.4 indices averaged for the trimesters FMA and DJF, respectively.	82
Figure 6.5 - Relationship between AMM-SST and Niño3.4.	85
Figure 6.6 - Relationship between AMM-SST and IPO.....	86
Figure 6.7 - Relationship between AMM-SST and MSLP.....	87
Figure 6.8 - Relationship between AMM-SST and NAO.....	88
Figure 6.9 - Lead-lag regression maps of SST (shaded 0.05 °C), MSLP (contour 0.2 hPa) and 10-m wind components (vectors) onto unfiltered AMM-SST index.	90
Figure 6.10 - Lead-lag regression maps of SST (shaded 0.05 °C), MSLP (contour 0.2 hPa) and 10-m wind components (vectors) onto low-pass filtered NAO index.....	93
Figure 6.11 - Lead-lag regression maps of SST (shaded 0.05 °C), MSLP (contour 0.2 hPa) and 10-m wind components (vectors) onto AMM index.	98
Figure 6.12 - Latitudinal hovmoller diagrams for zonally averaged (50 °W-10 °E) SST difference between NAO positive and negative composites.	101
Figure 7.1 - Monthly time series of global mean surface air temperature for the 4×CO ₂ (red line) and the piControl (black line) simulations.	106
Figure 7.2 - AMOC averaged over the period 91–150 yr simulated by BESM-OA2.5.	110
Figure 7.3 - AMOC averaged over the period 91–150 yr simulated by BNU-ESM.....	111
Figure 7.4 - AMOC averaged over the period 91–150 yr simulated by CanESM....	112
Figure 7.5 - AMOC averaged over the period 91–150 yr simulated by HadGEM2-ES.....	113
Figure 7.6 - Atlantic SST difference between the 4×CO ₂ and piControl simulations.....	115
Figure 7.7 - The leading maximum covariance analysis (MCA) mode between SST anomalies (shading, °C) and 10-m wind anomalies (arrows, m s ⁻¹) over tropical Atlantic (30° S–30° N) simulated by BESM-OA2.5....	119

- Figure 7.8 - The leading maximum covariance analysis (MCA) mode between SST anomalies (shading, °C) and 10-m wind anomalies (arrows, m s^{-1}) over tropical Atlantic (30° S–30° N) simulated by BNU-ESM.....120
- Figure 7.9 - The leading maximum covariance analysis (MCA) mode between SST anomalies (shading, °C) and 10-m wind anomalies (arrows, m s^{-1}) over tropical Atlantic (30° S–30° N) simulated by CanESM2.....121
- Figure 7.10 - The leading maximum covariance analysis (MCA) mode between SST anomalies (shading, °C) and 10-m wind anomalies (arrows, m s^{-1}) over tropical Atlantic (30° S–30° N) simulated by HadGEM2-ES..122

LIST OF TABLES

Table 5.1 - The description of the models used to compute the AMM.	58
Table 5.2 - Models results.....	69
Table 6.1 - Summarized relation between NAO index, Niño3.4 index and the phases of the AMM-SST based on the scatter plot of Figure 6.4, for the period 1900-2010.	83
Table 7.1 - The description of the models used.	105

LIST OF ABBREVIATIONS AND ACRONYMS

AABW	Antarctic Bottom Water
AMM	Atlantic Meridional Mode
AMO	Atlantic Multidecadal Oscillation
AMOC	Atlantic Meridional Overturning Circulation
AZM	Atlantic Zonal Mode
BESM-OA2.5	Brazilian Earth System Model – coupled ocean-atmosphere version 2.5
CanESM2	Canadian Earth System Model version 2
CHOR_RL	CMCC Historical Ocean Reanalysis system
CLIVAR	Climate and Ocean: Variability, Predictability and Change
CMIP5	Coupled Model Intercomparison Project Phase 5
CPTEC	Centro de Previsão de Tempo e Estudos Climáticos/Center for Weather Forecasting and Climate Studies
ENSO	El Niño-Southern Oscillation
ERSSTv4	Extended Reconstructed Sea Surface Temperature version 4
GFDL	Geophysical Fluid Dynamics Laboratory
GPCP	Global Precipitation Climatology Project
HadGEM2-ES	Hadley Centre Global Environmental Model 2-Earth System
INPE	Instituto Nacional de Pesquisas Espaciais/Brazilian National Institute for Space Research
IPO	Interdecadal Pacific Oscillation
NAO	North Atlantic Oscillation
NOAA	The National Oceanic and Atmospheric Administration
MPI-ESM-MR	Max Planck Institute – Earth System Model – Medium Resolution
MSLP	Mean Sea Level Pressure
PDO	Pacific Decadal Oscillation
PNA	Pacific-North American pattern
PSA	Pacific-South American pattern
QBO	Quasi-Biennial Oscillation
PIRATA	Pilot Research Moored Array in the Tropical Atlantic (initially) / Prediction and Research Moored Array in the Tropical Atlantic (now)

RAPID-MOCHA or RAPID	United Kingdom–United States Rapid Climate Change, Meridional Overturning Circulation and Heat flux Array
SACZ	South Atlantic Convergence Zone
SAM	Southern Annular Mode
SST	Sea Surface Temperature
TACE	Tropical Atlantic Climate Experiment
TNA	Tropical North Atlantic
TPI	IPO Tripole Index
TSA	Tropical South Atlantic
WES	Wind-Evaporation-Sea Surface Temperature feedback
20CRv2	NOAA-CIRES 20th Century Reanalysis

CONTENTS

1	INTRODUCTION	1
1.1	Motivation	1
1.2	Objectives	3
2	LARGE-SCALE VARIABILITIES: A REVIEW	7
2.1	Atlantic Meridional Mode	7
2.1.1	Physical Mechanism	12
2.1.2	External Forcings	15
2.1.3	AMM Climate Impacts	21
2.2	Atlantic Meridional Overturning Circulation	22
2.3	El Niño-Southern Oscillation	23
2.4	South Atlantic Convergence Zone	23
2.5	North Atlantic Oscillation	24
2.6	Pacific-North America Pattern	24
2.7	Pacific-South America Modes	25
2.8	Southern Annular Mode	25
2.9	Pacific Decadal Oscillation	25
3	DATA AND METHODS	27
3.1	Data	27
3.2	Model	28
3.2.1	BESM-OA2.5	28
3.2.2	Experiments Design	29
3.3	Numerical Experiments	31
3.4	Analysis methods	33
3.4.1	Data pre-processing	33
3.4.2	Empirical Orthogonal Functions	33
3.4.3	Maximum Covariance Analysis	35
3.4.4	Other statistical analyses	36
4	CLIMATE VARIABILITY SIMULATED BY BESM-OA2.5	39
4.1	Atlantic Meridional Overturning Circulation	39
4.2	El Niño-Southern Oscillation	41
4.3	South Atlantic Convergence Zone	45
4.4	North Atlantic Oscillation	46

4.5	Pacific-North America Pattern	48
4.6	Pacific-South America Modes	49
4.7	Southern Annular Mode	50
4.8	Pacific Decadal Oscillation	51
4.9	BESM Simulation Summary	55
5	AMM IN FOUR STATE-OF-THE-ART MODELS	57
5.1	Models Results	58
5.2	AMM Simulation Summary	69
6	INFLUENCE OF LARGE-SCALE VARIABILITY ON THE AMM DECADAL TIME SCALE	71
6.1	Introduction	71
6.2	Relationship between the AMM and SST	71
6.3	Relationship between the AMM and OHC300	74
6.4	Revisiting the NAO and ENSO influence on the AMM	80
6.5	On the interpretation of NAO and AMO influences	89
6.6	NAO influence on AMM in four state-of-the-art models	96
6.7	Influence of NAO phases on the tropical North Atlantic SST	99
6.8	Section Summary	102
7	SIMULATED AMM IN THE IDEALIZED ABRUPT 4xCO ₂ EXPERIMENT 103	
7.1	Introduction	103
7.2	Surface Air Temperature Response	105
7.3	AMOC Response	106
7.4	SST Response	114
7.5	AMM response	115
7.6	Section Summary	123
8	CONCLUSIONS	125
	REFERENCES	131

1 INTRODUCTION

1.1 Motivation

The last four decades of research have revealed the influence of the ocean-atmosphere coupled system variability within the tropical Atlantic basin in the climate conditions observed on the adjacent continental regions (HASTENRATH; HELLER, 1977; LAMB, 1978; MOURA; SHUKLA, 1981; HASTENRATH, 1990; NOBRE; SHUKLA, 1996; XIE; CARTON, 2004). Therefore, a more accurate understanding of the tropical Atlantic variability shall contribute to improve climate prediction over these regions, benefiting their populations. Recent studies have also shown that atmospheric perturbations generated by the ocean-atmosphere coupled variability within the tropical Atlantic basin act as forcing conditions to El Niño-Southern Oscillation (ENSO; HAM; KUG; PARK, 2013; RODRÍGUEZ-FONSECA et al., 2009; WANG et al., 2009; WU et al., 2007), North Atlantic Oscillation (NAO; OKUMURA et al., 2001; WU et al., 2007) and Indian monsoon (KUCHARSKI et al., 2008; POTTAPINJARA et al., 2016). So, in a broader spectrum, further understanding of tropical Atlantic ocean-atmosphere coupled variability and its interaction with diverse large-scale phenomena shall allow reducing the uncertainties related to the climatic changes which may occur in a warmer planet.

The coupling of the ocean and atmosphere within the tropical Atlantic basin has been a relevant subject of Climate Science. Earlier studies have shown the influence of the sea surface temperatures anomalies (SSTA) in the position of the Intertropical Convergence Zone (ITCZ) and the related impact on the precipitation in the western Africa (LAMB, 1978; HASTENRATH, 1990) and in the northeastern Brazil (HASTENRATH; HELLER, 1977; MOURA; SHUKLA, 1981; NOBRE; SHUKLA, 1996). Thus, understanding the patterns of variability of the sea surface temperature (SST) and its coupling with the atmosphere, and potential teleconnections is a major scientific task in Climate Science. Such a task demands deep research on the dynamics of ocean and atmosphere, ocean-atmosphere interaction and the teleconnections that may influence the region.

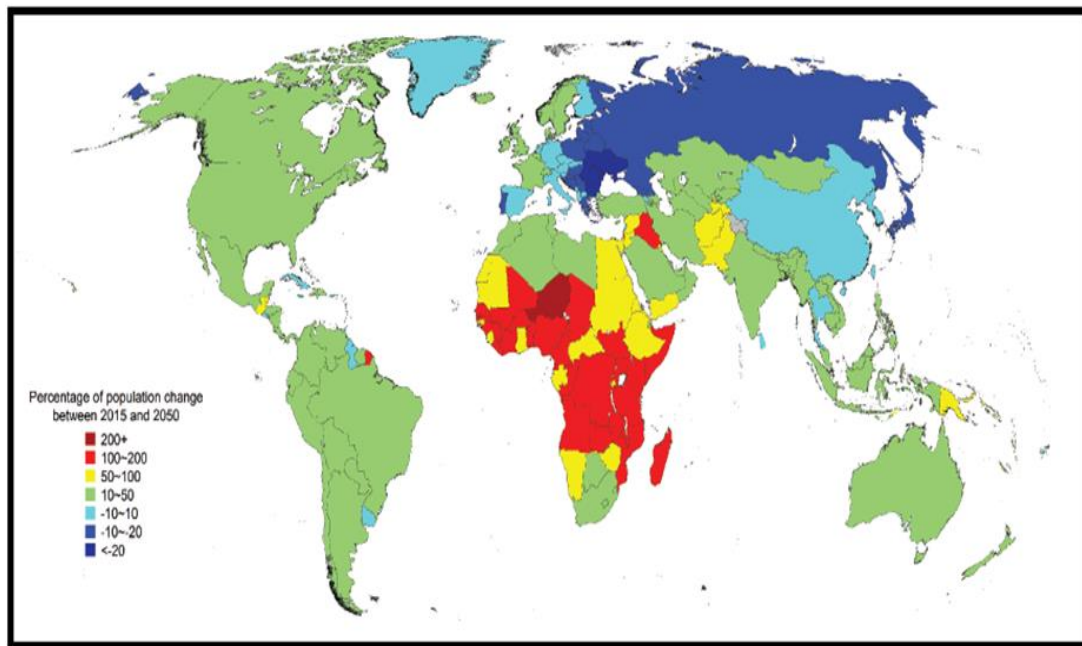
Besides the seasonal cycle forced by the Earth's position relative to the Sun, there are two ocean-atmosphere coupled variabilities within the tropical Atlantic basin: the

Atlantic Zonal Mode (AZM; ZEBIAK, 1993) and the Atlantic Meridional Mode (AMM; CHIANG; VIMONT, 2004; NOBRE; SHUKLA, 1996). The former has an interannual periodicity whereas the latter is characterized by interannual and decadal periodicities. Both phenomena are defined as patterns of the tropical Atlantic variability (TAV) and they have distinct climatic impacts in the surrounding land regions.

Although the AMM is characterized by an interannual and decadal time scales periodicities, the decadal periodicity with a spectral peak at ~11–13 years is the dominant temporal pattern (WAINER; SOARES, 1997; TOURRE; RAJAGOPALAN; KUSHNIR, 1999). Despite significant advances in the understanding of the AMM features, the reason for its dominant decadal variability remains to be explained (LIU, 2012). The present work aims to investigate the potential influences of large-scale phenomena on the AMM decadal periodicity. For this aim are analyzed ocean and atmospheric large-scale variabilities that can impact the AMM. My interest is to contribute to the understanding of the sources of the AMM decadal predictability and ultimately contribute to the decadal prediction of the precipitation regimes in the Tropical Atlantic continental regions.

It is estimated by the United Nations a significant increase in the population in Sub-Saharan Africa and in lower magnitude in South America by the year 2050 (Figure1.1). Therefore, the advance in the understanding of climatic phenomena over the Tropical Atlantic is extremely important in the short and long-term climate prediction. Such an advance will help a more efficient management of economic sectors of the countries of the region.

Figure 1.1 - Projected population growth for the year 2050.



The growth is represented by the percentage of population change between 2015 and 2050.
Source: United Nations (2015).

Currently, there are three ongoing projects which aim to study tropical Atlantic variability. Since 1998 the PIRATA program collects oceanic and atmospheric data near the surface through a moored array system and cruises, with the aim of understanding the ocean-atmosphere interactions (<https://www.pmel.noaa.gov/gtmba/pirata>). A project associated to NOAA which studies the mechanisms which can generate the interannual and decadal variability of the AMM and its interaction with other modes of variability within the basin (<http://www.aoml.noaa.gov/phod/research/tav/tcv/amm/index.php>). And CLIVAR which is a broader research program that investigates the dynamics and predictability of the coupled ocean-atmosphere system in different regions of the planet. TACE was a CLIVAR subprogram which aims to advance the understanding of the climatic processes in the tropical Atlantic (<http://www.clivar.org/clivar-panels/atlantic/tace>).

1.2 Objectives

As mentioned earlier, this work aims to study the influence of different ocean and atmosphere large-scale phenomena on the AMM, focusing in its dominant decadal periodicity. Firstly, the ocean variability is addressed. Vimont and Kossin (2007) shows that the Atlantic Multidecadal Oscillation (AMO) excited the AMM on decadal

time scale. From this result, it is hypothesized whether there is a physical mechanism triggered by the AMO that excite the AMM, or instead, the AMO and AMM are both excited by an external variability on decadal time scale. The latter hypothesis is analyzed by testing the potential link between the upper ocean heat content (OHC) in the Atlantic basin and the AMM on lower frequencies. Seidov et al., (2017) shows that upper OHC and AMO are highly correlated in the North Atlantic. Therefore, this part of the work can be summarized by the question: does the upper OHC variability in the Atlantic influence AMM on decadal time scale?

Previous studies have suggested that the ENSO and NAO impacts in tropical Atlantic can generate conditions to force the AMM (CZAJA; VAN DER VAART; MARSHALL, 2002; CHIANG; VIMONT, 2004). Nevertheless, regarding the NAO, some studies have questioned whether NAO is an effective AMM forcing (RUIZ-BARRADAS; CARTON; NIGAM, 2000; WAINER; SERVAIN; CLAUZET, 2008; DOI; TOZUKA; YAMAGATA, 2010). Therefore, the second aim of the study is to revisit the ENSO and NAO influence on the AMM. Here, a particular focus is given to the NAO and AMM relationship, since their connection still rises debate. The potential influence of the NAO on the AMM is the second hypothesis analyzed. Results of numerical experiments carried out to assess the impact of the NAO on the SST over the tropical Atlantic are shown.

A third hypothesis is explored in this work. This hypothesis is related to the question: what changes the spatio-temporal variability of the AMM may suffer under a perturbed climate scenario? The aim is to infer whether the AMM maintains its structure when forced by a warmer climate and different Atlantic Ocean circulation, through idealized simulations.

This thesis is organized by the following sections. In section 1 (present section) the motivation to study this topic and the objectives addressed are presented. In section 2 a review of the processes analyzed in this work are presented. In section 3 the observed and reanalysis datasets are presented; the Brazilian Earth System Model version 2.5 (BESM-OA2.5), the experimental design, and the numerical experiments are described; and the statistical methods used are described. Section 4 presents the evaluation of BESM-OA2.5 historical simulation, in which the most important atmospheric and oceanic large-scale phenomena of the climate system are evaluated.

Section 5 presents the AMM simulated by four state-of-the-art models. Section 6 presents the results of the analysis performed to address the first and second objectives. Section 7 presents the results of the analysis performed to address the third objective. Finally, section 8 presents the conclusions.

2 LARGE-SCALE VARIABILITIES: A REVIEW

This chapter presents a review of important oceanic and atmospheric large-scale variabilities. Special attention is given to the Atlantic Meridional Mode, focusing on its variability features, physical mechanism, external forcings that influence it and its impact on the surrounding land regions. More complete and comprehensive reviews about the tropical Atlantic variability can be found in Xie and Carton (2004) and in Chang et al., (2006b).

2.1 Atlantic Meridional Mode

The AMM is one of the predominant modes of covariability between the ocean and the atmosphere in the tropical Atlantic (NOBRE; SHUKLA, 1996; CHIANG; VIMONT, 2004). Historically, AMM has also been coined as the Gradient Mode of tropical Atlantic (CHIANG; KUSHNIR; GIANNINI, 2002), as the Atlantic Inter-hemispheric Mode (NOBRE; SHUKLA, 1996) and as the Atlantic dipole (XIE; CARTON, 2004). Throughout this work, the term Atlantic Meridional Mode will be used (SERVAIN et al., 1999; CHIANG; VIMONT, 2004; STOCKER et al., 2013).

The AMM can be obtained, following Chiang and Vimont (2004) and Amaya et al., (2017), by performing a maximum covariance analysis (MCA; BRETHERTON et al., 1992) in the SSTA and the 10-m wind components (U and V) anomalies over the tropical Atlantic region (30° S–30° N). The MCA consists of applying a singular value decomposition on the cross-covariance matrix between SSTA and 10-m wind components anomalies, which results in two time series called as expansion coefficients related to SST (AMM-SST) and 10-m wind components (AMM-Wind), respectively. The original SSTA and 10-m wind components anomalies are regressed onto the SST expansion coefficient at each grid point and presented in a regression map (Figure 2.1a). Prior to MCA application, the anomalies were obtained by removing the annual cycle subtracting climatological monthly means from the respective individual month and the datasets were also detrended for the period 1900–2010. The detrended datasets were obtained by removing the linear trend based on a least squares regression. The SST and the 10-m wind components are smoothed through a 3-month running mean at each grid point and the linear ENSO influence is removed by removing the cold tongue index (CTI; SST anomalies averaged over

Pacific region 6° S–6° N and 180°– 90° W) at each grid point based on a least squares regression, and finally, each field is normalized by its corresponding long-term standard deviation at each grid point. The analysis is performed for the period 1900–2010.

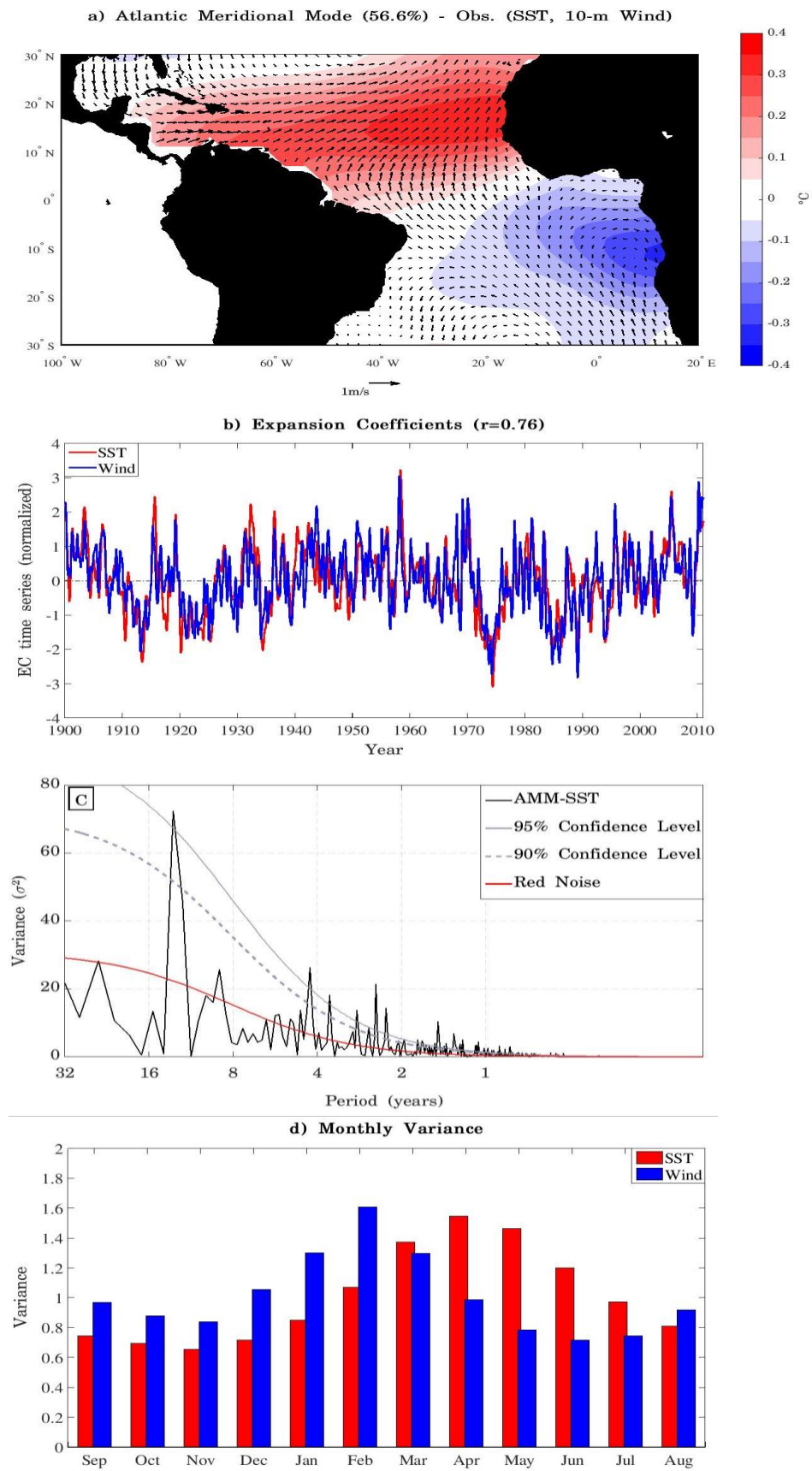
This mode represents the leading zero-lagged coupled variability between SSTA and 10-m wind anomalies. The AMM is characterized by an interhemispheric SST gradient centered in the thermal equator ($\sim 5^\circ$ N), reaching maxima anomalies of $\sim \pm 0.5^\circ$ C, with the centers of the gradient lobes being more prominent at 15° N/S in the eastern part of the basin. The low-level winds respond to the SST gradient by anomalously crossing the equator from the cooler hemisphere towards the warmer hemisphere. Figure 2.1b shows the normalized AMM-SST and AMM-Wind time series. The AMM is an interannual and decadal time scales mode of variability, with a dominant power spectrum at ~ 11 – 13 years (Figure 2.1c). In this case, it is used the AMM-SST, but a similar result is obtained using AMM-Wind. One of the AMM features that remains to be explained is the cause of its dominant decadal variability (see table 1 LIU, 2012).

The ITCZ over the Atlantic is modulated by the AMM dynamics moving towards the warmer hemisphere (HASTENRATH; HELLER, 1977; NOBRE; SHUKLA, 1996; DESER et al., 2010). The maximum amplitude of the AMM is observed mainly in the boreal spring (March-April-May [MAM]; CZAJA, 2004; SUTTON; JEWSON; ROWELL, 2000) influencing significantly the precipitation in Northeast Brazil (HASTENRATH; HELLER, 1977; NOBRE; SHUKLA, 1996), although some years show a persistent signal during the Atlantic hurricane season, i.e. throughout the boreal summer (HU; HUANG, 2006). Figure 2.1d illustrates the month-to-month variance in which the AMM-SST peaks in MAM and the AMM-Wind peaks in JFM. The AMM phase-locked to the boreal spring can be the result of the external forcings that the North Atlantic Oscillation (NAO) and ENSO exert on it (CZAJA; VAN DER VAART; MARSHALL, 2002; CZAJA, 2004). Moreover, in boreal spring the mean SST is spatially homogeneous over a more extended area over the tropical Atlantic, therefore the ITCZ is more sensitive to small SST perturbations in the meridional direction (CHIANG; KUSHNIR; GIANNINI, 2002). The AMM-Wind leads the AMM-SST by a month with a correlation of ~ 0.78 , meaning that the wind drives the SST variability (Figure 2.1e). Nonetheless, the cross-correlation structure is roughly

symmetric, indicating that there is a significant coupling between SST and 10-m wind (CHIANG; VIMONT, 2004). By convention, the AMM is in its positive phase when the SSTA in the TNA are warmer than in the tropical South Atlantic (the case of Figure 2.1a), being the negative phase the opposite SSTA gradient.

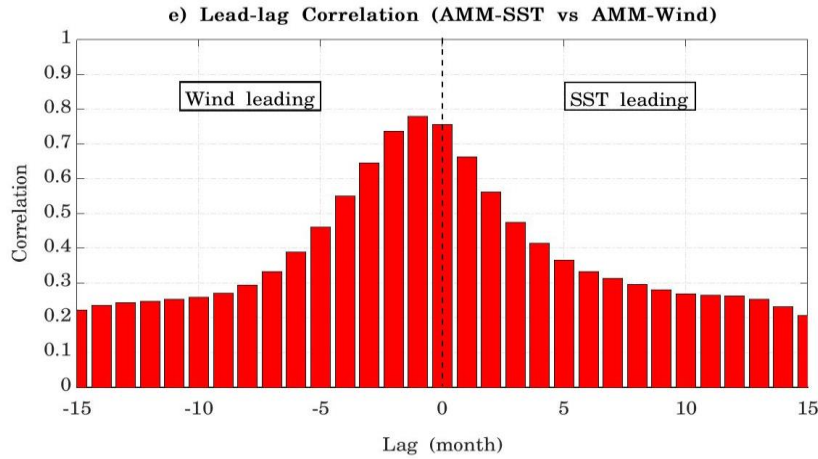
In this case the datasets used and the period analyzed are different from the references, nonetheless, the results are very similar, with a correlation for the period 1948–2010 of 0.90 between the AMM-SST computed and from Chiang and Vimont (2004). The AMM time series and more information about the mode can be found in the webpages <https://www.esrl.noaa.gov/psd/data/timeseries/monthly/AMM/> and <http://www.aos.wisc.edu/~dvimont/MModes/Home.html>.

Figure 2.1 - The Atlantic Meridional Mode.



continue

Figure 2.1 – Conclusion.



a) The leading maximum covariance analysis (MCA) mode between SSTA (shading, °C) and 10-m wind anomalies (arrows, m s^{-1}) over tropical Atlantic (30°S – 30°N). The mode is shown as the SSTA and 10-m wind anomalies regressed onto the SST normalized expansion coefficient (AMM-SST) time series (°C per standard deviation) for the period 1900–2010. The contour interval is 0.05°C . The squared covariance fraction of the mode is 56.6%. b) The normalized AMM-SST (red) and AMM-Wind (blue) time series. Their correlation is 0.76. c) The power spectrum of the AMM-SST time series. The solid red line represents the theoretical red noise spectrum, the dashed and solid gray lines represent the 90% and 95% confidence level, respectively. d) The month-to-month variance of the AMM-SST (red) and AMM-Wind (blue). e) The cross-correlation between the AMM-SST and AMM-Wind time series. Datasets are provided by the 20CRv2 and ERSSTv4 reanalysis.

Source: by the author.

Early studies applying the Empirical Orthogonal Functions (EOF) to the SSTA found an asymmetric interhemispheric SST dipole in tropical Atlantic (SERVAIN, 1991). However, it was suggested that this can be an EOF artifact (DOMMENGET; LATIF, 2002), with several studies showing that the SSTA at each hemisphere are not significantly anticorrelated (HOUGHTON; TOURRE, 1992; RAJAGOPALAN; KUSHNIR; TOURRE, 1998; DOMMENGET; LATIF, 2000). It is established that the AMM is not an asymmetric interhemispheric SST dipole but instead an interhemispheric SST gradient (MAHAJAN; SARAVANAN; CHANG, 2010; FOLTZ; MCPHADEN; LUMPKIN, 2012) and should be regarded as a coupled ocean-atmosphere mode (CHANG; KI; LI, 1997; CHIANG; VIMONT, 2004; MAHAJAN; SARAVANAN; CHANG, 2010; NOBRE; SHUKLA, 1996; RUIZ-BARRADAS; CARTON; NIGAM, 2000).

In the Pacific Ocean, there is an AMM counterpart coined as Pacific Meridional Mode (PMM; CHIANG; VIMONT, 2004; YUKIMOTO et al., 2000). Chiang and Vimont

(2004) obtains the PMM by applying the same methodology as AMM for the tropical Pacific.

Most of the CMIP5 models are capable of simulating an AMM-like pattern over the tropical Atlantic for the 20th century, although they tend to underestimate the SSTA variability and to put the tropical North Atlantic (TNA) SSTA too close to the equator (IPCC, 2013). Amaya et al. (2017) using the current definition to access the AMM, as defined by Chiang and Vimont (2004), shows that CMIP5 models underestimate the covariance explained (35% for a multi-model mean) and poorly generates the Wind-Evaporation-SST positive feedback (WES feedback; XIE; PHILANDER, 1994), the key role thermodynamic process to generate the AMM.

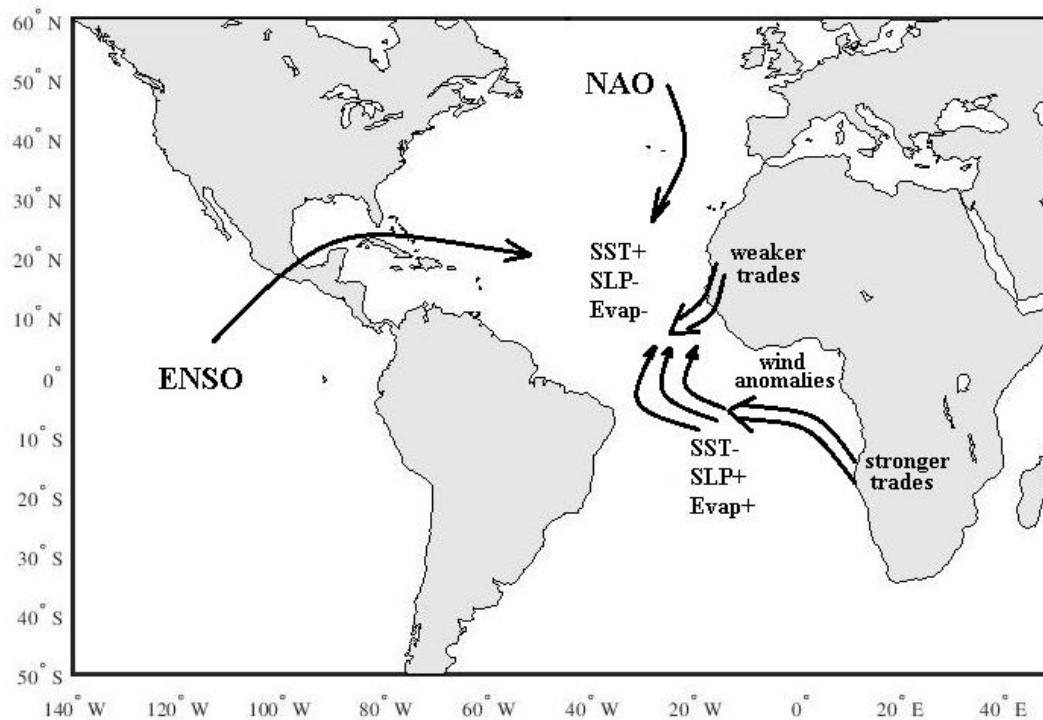
2.1.1 Physical Mechanism

Early studies showed competing results about the nature of AMM. Some studies suggest that AMM is just the response of the lower atmosphere to the SST interhemispheric gradient (MEHTA, 1998; SUTTON; JEWSON; ROWELL, 2000) opposing to studies that suggest that the AMM is an ocean-atmosphere coupled mode that rises from thermodynamic coupling (NOBRE; SHUKLA, 1996; CHANG; KI; LI, 1997; XIE, 1999; RUIZ-BARRADAS; CARTON; NIGAM, 2000). Recent studies using observational datasets and/or coupled atmosphere-ocean general circulation models (AOGCM) indicate that indeed the AMM is likely to be generated by an ocean-atmosphere thermodynamic coupling system (AMAYA et al., 2017; CHIANG; VIMONT, 2004; MAHAJAN; SARAVANAN; CHANG, 2010, 2011). In fact, numerical experiments show that the AMM growth rate is significantly more impacted by the coupling of surface heat flux with SST than by the coupling with momentum flux (CARTON et al., 1996; CHANG; KI; LI, 1997).

The physical mechanism established in explaining the growth and spatial propagation of the AMM is the WES feedback. Carton et al. (1996) suggest that change in ocean surface heat flux induced by low-level winds is an important mechanism in off-equatorial SST variability. Chang et al. (1997) and Xie (1999) successfully simulate the AMM applying the mechanism suggested by Carton et al. (1996) and the WES positive feedback mechanism. Studies using either coupled models (CHANG; KI; LI, 1997; MAHAJAN; SARAVANAN; CHANG, 2009, 2010) or idealized models (VIMONT, 2010; XIE, 1999) are able to simulate the SST gradient growth through

the WES feedback. Such results suggest that AMM is an ocean-atmosphere coupled mode of variability, in which the WES feedback has a crucial role in the coupling system. Numerical experiments in which the WES feedback is suppressed show a significant reduction of the meridional SST gradient magnitude, reinforcing this thermodynamic feedback as a key role process (WU; LIU, 2002; WU; ZHANG; LIU, 2004; MAHAJAN; SARAVANAN; CHANG, 2010). Nevertheless, the WES feedback process is more efficient in the deep tropics (10° N to equatorward) and external forcing is needed to trigger and sustain the process from the subtropical regions (XIE, 1999; CHANG; JI; SARAVANAN, 2001; CHIANG; KUSHNIR; GIANNINI, 2002; CZAJA; VAN DER VAART; MARSHALL, 2002; HU; HUANG, 2006; YANG et al., 2017). ENSO and NAO have been proposed as dominant external forcings (ENFIELD; MAYER, 1997; XIE; TANIMOTO, 1998; CZAJA; VAN DER VAART; MARSHALL, 2002; CHIANG; VIMONT, 2004).

Figure 2.2 - The description of the AMM physical mechanism based on the WES positive feedback process during an AMM positive phase event.



The arrows show the wind direction and the external forcings exerted by ENSO and NAO. The acronyms SST, SLP and Evap mean sea surface temperature, sea level pressure and ocean surface evaporation, respectively.

Source: by the author.

Following the interpretation of the Figure 2.2, the established physical mechanism that explains the AMM is resumed as follow: an initial gradient of positive (negative) SSTA in the tropical North (South) Atlantic induces a southward cross-equatorial pressure gradient due to the hydrostatic adjustment to the differential heating of the boundary layer (LINDZEN; NIGAM, 1987). Such conditions generate anomalous northward cross-equatorial low-level winds which are deflected eastward in the TNA due to the Coriolis force. The winds deflection reduces the background southeasterly trade winds in the TNA while the northeasterly trade winds in the tropical South Atlantic (TSA) enhance due to the southward cross-equatorial pressure gradient. Such a change in the intensity of the winds leads to a decrease (increase) in ocean surface evaporation, which leads to an enhancing of the initial anomalous SST in both hemispheres. Thus, further enhancing the anomalous SST gradient and subsequent wind response, reducing (enhancing) the background southeasterly (northeasterly) trade winds, consequently continuing to decrease (increase) the ocean surface evaporation, leading to an amplification of the initial SST gradient anomalies. This positive feedback mechanism is known as WES feedback. Therefore, the AMM results from a thermodynamic coupling between the wind speed, the sea surface evaporation induced by the wind stress and the SST (XIE, 1999; KUSHNIR et al., 2002; MAHAJAN; SARAVANAN; CHANG, 2009, 2010; VIMONT, 2010; AMAYA et al., 2017). The ocean-atmosphere coupling system is damped by SSTA advection caused by ocean currents (CHANG; KI; LI, 1997; SEAGER et al., 2001) and by surface Ekman flow (XIE, 1999; KUSHNIR et al., 2002). Tanimoto and Xie (2002) indicates the cloud role, acting as negative feedback over the positive SSTA lobe since in this lobe there is an enhancement of cloud formation which reduces the radiation that reaches the sea surface. They also suggest that in the subtropical region there is cloud formation over negative SSTA, acting as positive feedback since it reduces the radiation that reaches the sea surface, enhancing the cooling effect. The mechanisms explained above are related to the AMM positive phase.

Theoretical models can generate the AMM-like pattern but fail to correctly simulate the time scale periodicity, indicating that the meridional mode is a damped system and requires external forcing for their evolution (VIMONT, 2010; XIE, 1999). The ENSO and the NAO are the main external forcings that can excite an AMM formation, in particular by forcing winds anomalies in the TNA (NOBRE; SHUKLA, 1996; XIE,

1999; CZAJA; VAN DER VAART; MARSHALL, 2002). Atmospheric circulation anomalies over the TNA seems to be the main source of AMM interannual to decadal variability (HU; HUANG, 2006; MARTINEZ-VILLALOBOS; VIMONT, 2016; SMIRNOV; VIMONT, 2012; TANIMOTO; XIE, 2002; XIE; TANIMOTO, 1998), although the TSA high pressure system has also been highlighted as an external forcing of the AMM, by potentially exciting WES feedback processes (MÉLICE; SERVAIN, 2003; BARREIRO et al., 2004).

2.1.2 External Forcings

2.1.2.1 El Niño-Southern Oscillation

ENSO phenomenon is the dominant coupled ocean-atmosphere variability in the tropical Pacific, impacting the weather/climate conditions in different regions of the planet through atmospheric teleconnections (see MCPHADEN et al., 2006). ENSO has its peak phase in boreal winter (DJF) and its influence in the TNA lags by 4–5 months (ENFIELD; MAYER, 1997; CZAJA; VAN DER VAART; MARSHALL, 2002; HANDOY et al., 2006; AMAYA; FOLTZ, 2014), therefore in the boreal spring AMM peak season. Numerical experiments using an atmospheric model coupled to a mixed layer ocean model and imposing an ENSO-like external forcing signal are able to capture the basic features of the evolving SSTA which are observed in the TNA during the boreal spring (ALEXANDER; SCOTT, 2002; SARAVANAN; CHANG, 2004; BARREIRO; CHANG; SARAVANAN, 2005; MAHAJAN; SARAVANAN; CHANG, 2010). Studies regressing the SST over the Atlantic onto Niño index (an ENSO variability index) found that the meridional mode is the leading response to ENSO events, accounting for 30% of the AMM variability (ENFIELD; MAYER, 1997; RUIZ-BARRADAS; CARTON; NIGAM, 2000; SARAVANAN; CHANG, 2000). However, ENSO seems to significantly influence the AMM in the interannual time scales only (RUIZ-BARRADAS; CARTON; NIGAM, 2000; CZAJA; VAN DER VAART; MARSHALL, 2002; NOBRE; ZEBIAK; KIRTMAN, 2003; LIU; ZHANG; WU, 2004; WU; ZHANG; LIU, 2004)

The ENSO forcing can influence the SST over the Atlantic through the teleconnections Pacific-North America pattern (HANDOY et al., 2006; NOBRE; SHUKLA, 1996), changes in the Walker and Hadley tropical circulation cells

(KLEIN; SODEN; LAU, 1999; SARAVANAN; CHANG, 2000) and the tropospheric temperature mechanism (CHIANG; LINTNER, 2005; CHIANG; SOBEL, 2002).

The ENSO influence on TNA SST via the Pacific-North America (PNA) pattern is caused by the reducing (increasing) of the PNA pressure center over the southeastern United States (PNA fourth lobe) during El Niño (La Niña) events. Associated with the reducing (increasing) of the PNA pressure center, anomalous southwesterlies (northeasterlies) drives changes in the ocean surface latent heat flux over the subtropical North Atlantic and warms (cools) the ocean mixed layer (NOBRE; SHUKLA, 1996; ENFIELD; MAYER, 1997; GIANNINI; KUSHNIR; CANE, 2000; AMAYA; FOLTZ, 2014). Along with the PNA teleconnection, during an El Niño event, the Walker circulation cell adjustment forces anomalous subsidence over the equatorial Atlantic. As response to this Walker circulation cell adjustment, the Hadley circulation cell reduces its meridional circulation and therefore the wind trades over the TNA. Such anomalous circulation patterns reinforce latent heat flux anomalies and consequently favors the warming of the ocean mixed layer (KLEIN; SODEN; LAU, 1999; SARAVANAN; CHANG, 2000; WANG, 2004). This external forcing can trigger the WES feedback process and ultimately the formation of the AMM (ENFIELD; MAYER, 1997; XIE; CARTON, 2004).

The tropospheric temperature mechanism has a stronger impact near the equatorial Atlantic than in the subtropical areas (CHIANG; SOBEL, 2002). The mechanism can be summarized as follows. A strong El Niño event anomalously warms the free troposphere over the eastern equatorial Pacific, which then propagates to the Atlantic as eastward Kelvin wave. Consequently, the free troposphere over equatorial Atlantic warms and forces a downward stable atmosphere by reducing the local moist convection. In such conditions, the boundary layer energy increases through the latent heat flux from the ocean surface evaporation. However, the persistence of anomalous troposphere positive temperature and accumulation of water vapor in the boundary layer leads to a reduction of the ocean surface evaporation which results in the warming of the equatorial Atlantic mixed layer (see CHANG et al., 2006a).

However, for the specific case of El Niño events, Lee et al., (2008) has shown that only events that persist at least until March impacts significantly the TNA SST in the boreal spring and summer seasons. Studies using numerical models (HUANG;

SCHOPF; PAN, 2002; HUANG, 2004) and observations (ENFIELD; MAYER, 1997; RUIZ-BARRADAS; CARTON; NIGAM, 2000; HUANG; ROBERTSON; KUSHNIR, 2005) conclude that the ENSO influence is stronger in the TNA SST than in the equatorial and TSA SSTs areas, where ocean-atmosphere local interaction may superimpose to the external forcing.

2.1.2.2 North Atlantic Oscillation

The NAO is the dominant atmospheric mode in the North Atlantic/European sector, consisting of a meridional sea level pressure dipole with a high pressure over the Azores and a low pressure center over Iceland, with peak phase in the boreal winter (see HURRELL; DESER, 2009). Studies using observations datasets suggest that the NAO variability during the boreal winter forces the AMM, through its southern lobe (Azores high), by inducing anomalous trade winds in the subtropical North Atlantic, which subsequently forces anomalous latent heat flux and leads to SSTA, in a similar way to the ENSO influence in the TNA, and ultimately can trigger and sustain the WES feedback process (XIE; TANIMOTO, 1998; CZAJA; VAN DER VAART; MARSHALL, 2002; CHIANG; VIMONT, 2004; HANDOH et al., 2006; PENLAND; HARTTEN, 2014). Huang and Shukla (2005) shows that NAO variability in boreal winter can originate the SSTA similar to the observed in the TNA through the variation of the trade winds in the equatorward side of the Azores high by carrying out an AOGCM experiment in which the Atlantic is coupled and the remaining ocean basins are uncoupled.

Although the NAO has been regarded as a potential external forcing to AMM, some studies point out its influence on AMM is not significant (RUIZ-BARRADAS; CARTON; NIGAM, 2000; WAINER; SERVAIN; CLAUZET, 2008). Furthermore, it is shown that the AMM can influence the NAO by weakening the subtropical high (RAJAGOPALAN; KUSHNIR; TOURRE, 1998; RUIZ-BARRADAS; CARTON; NIGAM, 2000; OKUMURA et al., 2001). Doi et al. (2010) through a composite analysis of AOGCM simulations find no clear relation between NAO and AMM. Modeling works using AOGCM suggest that the AMM generates from local ocean-atmosphere processes, while external forcing like ENSO and NAO modulate the AMM periodicity and enhance its variance, in which NAO forcing might be more important in the AMM decadal variability (WU; LIU, 2002; WU; ZHANG; LIU,

2004). Nevertheless, decadal variability tends to show more complex behavior response to remote forcings, which likely implies a more complex mechanism than a passive linear response one (LIU; ZHANG; WU, 2004).

2.1.2.3 Atlantic Multidecadal Oscillation and Aerosol Concentration

Along with the influence of ENSO and NAO on AMM, which have been identified since earlier studies, other features of the Atlantic basin have also been proposed recently, as the AMO and the concentration of atmospheric aerosol over the TNA.

The AMO is characterized by the warming and cooling of the North Atlantic SST on multidecadal time scales (~60–70 years; see DELWORTH; MANN, 2000) and excites the AMM on decadal time scale. Vimont and Kossin (2007) shows that the AMO leads AMM by a year with a maximum correlation of ~0.84 (decadal low-pass filter data). Tourre et al. (2010) through zero-lag correlation analysis found that both variabilities are more correlated in boreal spring and summer seasons.

More recently, the effect of advected mineral aerosols in the atmosphere from North Africa on the TNA SSTA has been explored (FOLTZ; MCPHADEN, 2008a, 2008b, EVAN et al., 2009, 2011; EVAN; FOLTZ; ZHANG, 2012). The aerosols influence SSTA through the reduction in surface solar insolation by their scattering sunlight effect. For the period 1984–2000, Foltz and McPhaden (2008b) observed that changes in aerosol concentration over the TNA explained ~35% of the observed interannual SST variability during boreal summer, the season when climatological aerosol concentrations are highest. Evan et al. (2011) through a theoretical model found that aerosol concentration variability over TNA leads the AMM by two years with a correlation of 0.57 (5-years low-pass filtered data). These studies advance that North African dust outbreak events can be seen as an effective way of AMM variability modulation.

2.1.2.4 Ocean Influences

The ocean component has not received much attention as the atmospheric counterpart. In fact, the AMM basic features are simulated using atmospheric model coupled to a motionless slab ocean model, i.e. a mixed layer ocean model with 50 m depth generally (MAHAJAN; SARAVANAN; CHANG, 2009, 2010). Some studies suggest that the subsurface ocean dynamics has a passive role in the AMM-like pattern

evolution (CARTON et al., 1996; SEAGER et al., 2001; MÉLICE; SERVAIN, 2003). So, these results reinforce the scenario that the formation of the AMM during the boreal spring is led by an external influence via the atmosphere and the consequent development of the WES feedback process. However, as mentioned by Chang et al., 2006b, some numerical experiments using an atmospheric model coupled to a slab ocean model indicates that without the ocean dynamics the WES feedback tends to unrealistically enhance the coupling variability (BARREIRO et al., 2005; SARAVANAN; CHANG, 2004). Such results suggest that the ocean has a damping role in the tropical Atlantic, therefore the ocean component has not a passive role in the AMM evolution as previous works suggest.

Cross-equatorial mean currents advecting sea water from the southern hemisphere towards the northern hemisphere, as the South Equatorial Current and the North Brazil Current, can act as damping mechanism of the established anomalous SST gradient associated with AMM (CHANG; KI; LI, 1997; CHANG; JI; SARAVANAN, 2001; SEAGER et al., 2001; LEE; WANG, 2008). The Ekman flow induced by the climatological wind trades acts to dampen the gradient as it advects the SSTA poleward (XIE, 1999). Ocean dynamics induced by atmospheric pattern associated with AMM have also been described as damping mechanism. Joyce et al., (2004) suggests that as a response to the anomalous westerly wind associated inter-hemispheric SSTA gradient (assuming, for instance, the AMM positive phase) anomalous wind stress curl is generated in the NH. Such negative rotational induces Sverdrup transport that advects warmer waters from NH towards SH, consequently damping the gradient. However, Foltz et al., (2012) using observational datasets observed that in response to WES positive feedback, the anomalous southeasterly (northwesterly) winds that occur in the positive (negative) phase generate Ekman pumping, i.e. upwelling, in deep TSA (TNA) causing the thermocline to shoaling and enhance the negative SSTA. This coupled wind-Ekman pumping-SST feedback can be a way along with the WES feedback of AMM growth and sustaining. This result reinforces the view that ocean dynamics is relevant in the deep tropics (CARTON et al., 1996; FOLTZ; MCPHADEN, 2006).

Recent works have focused on the Guinea Dome (GD) variability, a region of upwelling located in the western African coast (8° – 20° N), as potential AMM preconditioning (DOI; TOZUKA; YAMAGATA, 2009, 2010). The studies propose

that a weak (strong) Ekman pumping causes anomalously weaker (stronger) GD and an associated deeper (shallower) mixed layer depth during the boreal summer and fall seasons. Such condition reduces (increases) the mixed layer temperature sensitive to the atmospheric cooling that occurs in winter, resulting in positive (negative) SSTA. These anomalies can then be amplified by WES feedback, leading to AMM formation in the following boreal spring. Moreover, in the case of positive AMM phase, with anomalous northward ITCZ migration in the NH, the anomalous westerly winds induces Ekman upwelling in the GD due to the positive rotational of the wind stress curl. This acts as negative feedback and can lead to AMM decay. Nevertheless, the authors highlight that the GD has a periodicity of about two years; therefore this mechanism could not explain the AMM decadal periodicity. Another important feature of the Atlantic Ocean is the Meridional Overturning Circulation (MOC). However, numerical experiments in which the Atlantic MOC is shut down, the AMM remains unaltered (HAARSMA et al., 2008).

The interaction between AMM and Atlantic Zonal Mode (AZM) has also been investigated and their interaction seems to be mainly through the ocean pathway. Servain et al., (1999) shows that both modes are linked, being AZM influenced by changes in the climatic conditions generated by the AMM. However, the correlation between the two modes in their respective months' peak is only about -0.3 for the period 1982–2009 (FOLTZ; MCPHADEN, 2010). In spite of that, Foltz and McPhaden (2010) suggests that an AMM event leads two competing situations, (1) wind stress anomalies in the western part of the tropical Atlantic generate equatorial Kelvin waves that reinforce the thermocline depth anomalies in the eastern tropical Atlantic (positive feedback) and (2) wind stress anomalies in the central and western part of the tropical Atlantic generate equatorial Rossby waves that reflect at the coast of South America and propagate eastward as equatorial Kelvin waves exerting an opposite forcing in the thermocline depth anomalies in the eastern tropical Atlantic (negative feedback). Also, based on wind field anomalies on the western part of the basin, Zhu et al., (2012) shows that the ocean heat content accumulation anomalies over the tropical Atlantic associated to AMM peak phase is discharged into the eastern equatorial Atlantic through an equatorial waveguide and can stimulate the AZM.

2.1.3 AMM Climate Impacts

It is well documented the influence that AMM exerts over the Northeast Brazil region (NEB). Several studies analyzing the relation of dry/wet years and the Atlantic SST patterns, concluded that droughts in the region are associated to anomalous Northern migration of the ITCZ in response to an anomalous interhemispheric SST gradient, with warmer water in the TNA and cooler water in the TSA, therefore positive phase of the AMM (HASTENRATH; HELLER, 1977; MOURA; SHUKLA, 1981; SERVAIN, 1991; NOBRE; SHUKLA, 1996; POLZIN; HASTENRATH, 2014). The AMM has a strong impact in the NEB precipitation regime since both peaks at the same season (March to May). Nonetheless, recent works show that the NEB precipitation is also modulated by the ENSO, through either direct atmospheric influence or its impact on the tropical Atlantic SST (RODRIGUES et al., 2011; HASTENRATH, 2012).

The West Africa Sahel precipitation regime is also influenced by different phases of the AMM (LAMB, 1978; FOLLAND; PALMER; PARKER, 1986; GIANNINI; BIASUTTI; VERSTRAETE, 2008; HASTENRATH; POLZIN, 2011, 2014). However, for this region, the AMM impact is weaker than the observed in the NEB. The Sahelian precipitation variability has shown a complex behavior suggesting multiple competing external physical influences (for a recent review, see NICHOLSON, 2013). In fact, several studies have shown that different large-scale phenomena have influence on the Sahelian precipitation regime, as the AMO (HOERLING et al., 2006; MOHINO; JANICOT; BADER, 2011), slow variations of the Indian Ocean SSTA (GIANNINI; SARAVANAN; CHANG, 2003; HOERLING et al., 2006) and Pacific Ocean SSTA (FOLLAND; PALMER; PARKER, 1986; PALMER, 1986; GIANNINI; SARAVANAN; CHANG, 2003), and also by the Mediterranean sea (RODRÍGUEZ-FONSECA et al., 2011). Along with the oceanic role, the magnitude of the Sahelian precipitation variability observed in the 20th century is enhanced by local land-atmosphere interaction processes (CHARNEY; STONE; QUIRK, 1975; ZENG et al., 1999; GIANNINI; SARAVANAN; CHANG, 2003).

More recently, the potential link between the AMM and hurricanes activities (i.e. frequency, duration and intensity) in the North Atlantic has been analyzed. Hurricanes

and their respective intensity are strongly correlated to TNA SST on decadal time scales (EMANUEL, 2005). In particular, the AMM is associated with large-scale local climatic conditions which manifest in Atlantic hurricane Main Development Region (MDR; 90°–20°W, 5°–25°N) influencing the Atlantic hurricane season activity on interannual and decadal time scales (KOSSIN; VIMONT, 2007; VIMONT; KOSSIN, 2007). Vimont and Kossin (2007) found that during the AMM positive phase there are above normal hurricanes with longer duration, but a weaker relationship is observed with the hurricanes intensity. Smirnov and Vimont (2011) shows that during a very active hurricane season the boreal summer AMM tend to have the physical features of its predominant boreal spring season. Besides the AMM influence, the importance of both AMM and ENSO events in the Atlantic hurricane season activity is observed (PATRICOLA; SARAVANAN; CHANG, 2014). As a remote forcing, Zhang et al. (2017) found that the AMM also modulates the tropical cyclone activity in the western Pacific.

2.2 Atlantic Meridional Overturning Circulation

The MOC plays an important role in transporting heat from the tropics to higher latitudes of both hemispheres by the ocean. In the case of the Atlantic basin the Atlantic MOC (AMOC), unlike the Pacific and Indian basins, transports heat northward from Southern Hemisphere to high-latitudes of the Northern Hemisphere, where it has a profound impact on the climate of the surrounding continents by releasing heat into the atmosphere (BUCKLEY; MARSHALL, 2015). The AMOC (or MOC in general) is defined as zonally and vertically integrated volume transport at depth coordinates and is presented in a latitude/depth plane (LOZIER, 2012; BUCKLEY; MARSHALL, 2015); given by the following equation:

$$\Psi(y, z) = \int_z^\eta \int_{x_w}^{x_e} v dx dz \quad (m^3 s^{-1}), \quad (2.1)$$

in which v is the meridional velocity, z is the vertical coordinate increasing upward (from the bottom to the surface), η is the height of the free surface, and $x_w(z)$ and $x_e(z)$ are the westward and eastward positions of the bathymetry at a certain depth (BUCKLEY; MARSHALL, 2015). The strength of the AMOC at each latitude

consists of the maximum value of the AMOC observed over the water column. The maximum strength of the AMOC is defined in the latitude and depth where the AMOC has its maximum value.

The present-day AMOC consists of two overturning cells (RAHMSTORF, 2002; LUMPKIN; SPEER, 2007; DELWORTH et al., 2008). The upper overturning cell is the cell which transports warmer and salty waters northward on its upper limb, that fills the upper ~1000 m. The warmer and salty waters reach the subpolar and polar regions, where they cool down by releasing heat into the atmosphere and subsequently losing buoyancy and sinking, generating the North Atlantic Deep Water (NADW). The NADW forms the lower limb of the upper overturning cell that transport cooler waters southward at depths ranging from ~1500 to ~4500 m. The lower overturning cell consists of the Antarctic Bottom Waters (AABW) that transports cool waters northward from depths of ~4,500 m to the ocean floor. The AABW rise into the lower part of the NADW and close the lower overturning cell.

2.3 El Niño-Southern Oscillation

The El Niño-Southern Oscillation (ENSO) is one of the most prominent climate variability phenomena at interannual time scales, with strong impacts on regions surrounding the Indian and Pacific Oceans and regions that are influenced by its teleconnections (MCPHADEN; ZEBIAK; GLANTZ, 2006). It is a coupled ocean-atmosphere phenomenon characterized by the variation of SST anomalies over the central and eastern tropical Pacific; in which positive equatorial SST anomalies are associated to El Niño events and negative SST anomalies to La Niña events. As a coupled response, changes in the tropical wind patterns forces the equatorial-tropical SST anomalies to persist, imposing atmospheric pressure variations over the Indo-Pacific region (referred as Southern Oscillation), which causes changes in the intertropical convection and induces planetary teleconnections.

2.4 South Atlantic Convergence Zone

The South Atlantic Convergence Zone (SACZ) is characterized by an intense NW-SE oriented cloud band that extends from the Amazon Basin to the South Atlantic subtropics, mainly during austral summer (NOGUÉS-PAEGLE; MO, 1997; CARVALHO; JONES; LIEBMANN, 2004; DE OLIVEIRA VIEIRA;

SATYAMURTY; ANDREOLI, 2013). The formation of the SACZ has a strong influence on the precipitation over southeast South America and is considered, together with the convection activity over the Amazon Basin, the main component of the South American Monsoon System (JONES; CARVALHO, 2002). The southern part of the SACZ usually lies over cooler SST (ROBERTSON; MECHOSO, 2000; GRIMM, 2003). Chaves and Nobre, (2004) suggesting that the formation of SACZ over the ocean tend to block the solar radiation by clouds, cooling the SST beneath. AGCM are not able to simulate the precipitation over cooler SST caused by SACZ (MARENGO et al., 2003; NOBRE et al., 2006, 2012), since such models tend to increase the precipitation over warmer SST, as a hydrostatic response. Nobre et al., (2012) has shown that coupled AOGCMs are able to simulate the SACZ formation over colder SST anomalies, as this class of models englobes the atmosphere-ocean surface thermodynamic coupling.

2.5 North Atlantic Oscillation

The North Atlantic Oscillation (NAO) is a major atmospheric variability pattern occurring in the North Atlantic, which is characterized by the oscillation of the difference on the sea level pressure (SLP) between Iceland and Portugal (WANNER et al., 2001; HURRELL et al., 2003). NAO has a great impact in the Euro-Atlantic region (HURRELL et al., 2003; HURRELL; DESER, 2010), with the notable work of (NAMIAS, 1972) relating droughts over the Northeast Brazil to NAO variations. Recent studies also show its teleconnections to the East Asia (WU et al., 2012; YU; ZHOU, 2004). The NAO's influence on a rapid climate change in the Northern Hemisphere has been highlighted in Delworth et al. (2016), which increases the importance of its correct simulation. The NAO's largest amplitude of variation occurs mainly during the boreal winter.

2.6 Pacific-North America Pattern

Jointly, the NAO and the Pacific-North American pattern (PNA) are the dominant atmospheric internal modes over the boreal hemisphere. The PNA is characterized by four centers of high pressure anomalies in the North Pacific and North America, respectively; over Hawaii, to the south of the Aleutian Islands, in the intermountain region of North America, and in the Gulf Coast region of the U.S.A., representing the

centers of action of a stationary wave train extending from the tropical Pacific into North America (WALLACE; GUTZLER, 1981). It exerts a significant influence on surface temperature and precipitation over North America (LEATHERS et al., 1991). Some studies have shown that, although the PNA is an internal atmospheric variability phenomenon, it is influenced by other climate variabilities, as the ENSO and the Pacific Decadal Oscillation (PDO) (see STRAUS; SHUKLA, 2002; YU; ZWIERS, 2007).

2.7 Pacific-South America Modes

The Pacific-South America (PSA) teleconnection modes are characterized by the second and third EOF of 500 hPa geopotential height over the Southern Hemisphere (20°–90° S) (MO; PEAGLE, 2001). PSA modes are stationary Rossby wave trains extending from central Pacific to Argentina, in which the PSA1 (EOF2) is a response to ENSO and the PSA2 (EOF3) is associated to the quasi-biennial component of ENSO (KAROLY, 1989; MO; PEAGLE, 2001). These patterns have a significant impact on rainfall anomalies over South America (MO; PEAGLE, 2001).

2.8 Southern Annular Mode

The Southern Annular Mode (SAM) is the dominant atmospheric variability in the Southern Hemisphere, occurring in the extra-tropics and in the high latitudes (KIDSON, 1988). It is also referred to as Antarctic Oscillation (AAO; GONG; WANG, 1999). SAM variability is characterized by anomalies variation in the polar low-pressure and in the surrounded zonally high-pressure belt. It can be captured through the first EOF applied to different atmospheric variables, as the sea level pressure, different geopotential height levels or the surface air temperature (ROGERS; VAN LOON, 1982; KIDSON, 1988; THOMPSON; WALLACE, 2000).

2.9 Pacific Decadal Oscillation

Observed SST anomalies over the North Pacific have shown an oscillatory pattern in the central and western parts in relation to the tropical part and along the North American west coast. This oscillatory shift of SST anomalies with interdecadal periodicity was termed Pacific Decadal Oscillation (PDO) and it is defined as the leading EOF of the monthly SST anomalies over North Pacific (MANTUA et al.,

1997). The positive phase of PDO is defined when negative SST anomalies predominate over the central and western parts of North Pacific, and positive SST anomalies predominate over the Tropical Pacific and along the North American west coast; being the negative phase the reverse pattern. Many studies have connected the PDO with variations on precipitation regimes in different regions around the world, as South China monsoon (WU; MAO, 2016), Indian monsoon (KRISHNAMURTHY; KRISHNAMURTHY, 2016) and together with ENSO in the precipitation regime in North America (see HU; HUANG, 2009). There are different mechanisms that modulate PDO, in which one of them is the response of the Northern Pacific SST to the ENSO variability via the “atmospheric bridge” (for a detailed review, see NEWMAN et al., 2016).

3 DATA AND METHODS

3.1 Data

Throughout this thesis, several analyses are performed using different atmospheric and ocean variables. The datasets are provided by reanalysis products. The atmospheric fields, mean sea level pressure (MSLP), surface wind components (10-m wind), are from the Twentieth-Century Reanalysis dataset version 2 (20CRv2; COMPO et al., 2011) with a global horizontal resolution of $2^\circ \times 2^\circ$ and 24 vertical levels, spanning from 1871 to 2012 (https://www.esrl.noaa.gov/psd/data/gridded/data.20thC_ReanV2.html). The Sea Surface Temperatures (SST) are obtained from the Extended Reconstructed Sea Surface Temperature version 4 (ERSSTv4; HUANG et al., 2015) available on a $2^\circ \times 2^\circ$ grid resolution, spanning from 1854 to the present (<https://www.esrl.noaa.gov/psd/data/gridded/data.noaa.ersst.v4.html>). The precipitation dataset is obtained from Global Precipitation Climatology Project version 2.2 Combined Precipitation Dataset (GPCP; ADLER et al., 2003; HUFFMAN et al., 2009) with global horizontal resolution of $2.5^\circ \times 2.5^\circ$, spanning from 1979 to the present (<http://rda.ucar.edu/datasets/ds728.2/#!description>). Observations of the Atlantic Meridional Overturning Circulation (AMOC) are conducted by the RAPID-WATCH MOC monitoring project (MCCARTHY et al., 2015). The AMOC dataset from 2004 to the present can be obtained in the webpage <http://www.rapid.ac.uk/rw/>. The ocean heat content in the upper 300 meters is obtained from the ocean reanalysis CHOR_RL (YANG; MASINA; STORTO, 2017) and covers the period 1900–2010. Since the original dataset is not in regular grid resolution, the OHC300 is interpolated into $1^\circ \times 1^\circ$ grid resolution. The CHOR_RL reanalysis (CHOR_RL) assimilates vertical profile data by being nudged to monthly Hadley Centre global sea Ice coverage and SST (HadISST) reconstructed fields, while the atmospheric forcings are from the 20CRv2 reanalysis (YANG; MASINA; STORTO, 2017). Finally, outputs from CMIP5 models are available in <https://esgf-node.llnl.gov/projects/cmip5/>.

3.2 Model

3.2.1 BESM-OA2.5

The atmospheric component of BESM-OA2.5 is the Brazilian Global Atmospheric Model (BAM; FIGUEROA et al., 2016) developed at Center for Weather Forecasting and Climate Studies (CPTEC/INPE). It is a primitive equation model with spectral representation with triangular truncation at the wave number 62, corresponding to a grid resolution of approximately $1.875^\circ \times 1.875^\circ$, and 28 sigma levels in the vertical, with uneven increment between the levels, i.e. T62L28 resolution. As mentioned before, it is in the atmospheric component which resides the main differences between BESM-OA2.5 and BESM-OA2.3 (NOBRE et al., 2013). The new version shows a key improvement in the energy balance at the top of the atmosphere, by reducing the mean global bias from -20 W m^{-2} in version BESM-OA2.3 to 2 W m^{-2} in the current version. Version 2.5 of BESM incorporates the formulation presented in JIMÉNEZ et al., 2012 for the representation of the wind, humidity and temperature in the surface layer. The model runs without flux correction or adjustment. The physics parameterizations for the continental processes are based on the Simplified Simple Biosphere Model (SSiB) land surface model (XUE et al., 1991), in shortwave radiation Clirad scheme (CHOU; SUAREZ, 1999; TARASOVA; BARBOSA; FIGUEROA, 2006), in longwave radiation Harshvardhan scheme (HARSHVARDHAN et al., 1987), in Cloud microphysics Ferrier scheme (FERRIER et al., 2002), in the turbulence level 2 module (MELLOR; YAMADA, 1982), in the gravity wave module (ANTHES, 1977), in the deep convection module (ARAKAWA; SCHUBERT, 1974; GRELL, GEORG AND DÉVÉNYI, 2002), and in the shallow convection module (TIEDTKE, 1983). More details can be found in Figueroa et al., (2016).

The oceanic component of BESM-OA2.5 is the Modular Ocean Model version 4p1 (MOM4p1; GRIFFIES, 2009) developed at GFDL, which includes the Sea Ice Simulator (SIS) built-in ice model (WINTON, 2000). There are no changes in the physics parameterizations from those used in BESM-OA2.3. The horizontal grid resolution in the zonal direction is 1° and in the meridional direction it varies uniformly from $1/4^\circ$ between 10° S and 10° N to 1° of resolution at 45° and to 2° of resolution at 90° , in both hemispheres. The vertical resolution has 50 levels with

approximately 10 m resolution in the upper 220 m, increasing gradually to about 370 m resolution at deeper levels. The oceanic model spin-up was done in a manner similar to that of Nobre et al. (2013) and Giarolla et al. (2015), in which begins the spin-up run from rest, and the T-S structure of the oceans of Levitus and Boyer (1994). The initial stage of the ocean model spin-up was done over a 13 years period, forced by climatological atmospheric fields (winds, solar radiation, air temperature and humidity, and precipitation). It was then integrated by an additional 58 years period, forced by interannually varying atmospheric fields from Large and Yeager (2009), while the river discharges and the sea ice variables were kept at their respective monthly mean climatological values. The forced ocean model run was used to save the oceanic dynamical and thermodynamical structures in order to be used in the initialization of future coupled model experiments.

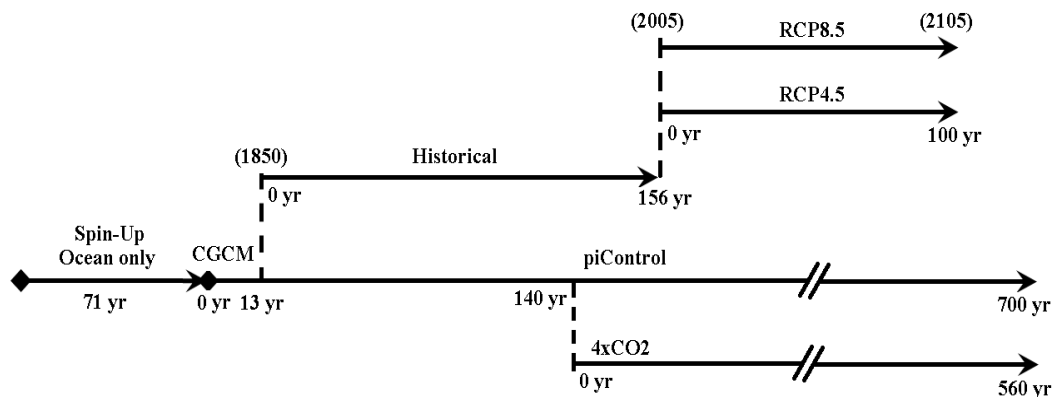
The atmospheric and oceanic models are coupled via the Flexible Modeling System (FMS) coupler, which was also developed at GFDL and incorporated in MOM4p1. The atmospheric model receives SST and ocean albedo from the ocean and sea ice models at hourly time steps. On the other hand, the oceanic model receives information about freshwater (liquid and solid precipitation), momentum fluxes (winds at 10 m), specific humidity, heat, vertical diffusion of velocity components and surface pressure, all also at hourly time steps. Wind stress fields are computed within MOM4p1 using Monin-Obukhov scheme (OBUKHOV, 1971). In coupled simulations, the ocean temperature and salinity restoration options are turned off.

3.2.2 Experiments Design

A set of numerical experiments were carried out with the coupled ocean-atmosphere version of BESM-OA2.5 by the BESM team, following the CMIP5 experiment design protocol (TAYLOR; STOUFFER; MEEHL, 2012), and shown schematically in Figure 3.1. Out of those experiments listed below, the Historical, the piControl and the Abrupt 4×CO₂ simulations are used in this thesis:

- Historical: the simulation runs over the period 1850–2005 (156 years), forced by atmospheric equivalent CO₂ observed historical concentration (greenhouse gas only) over this period, based on CMIP5 protocol.
- piControl: it runs for 700 years, forced by invariant pre-industrial atmospheric CO₂ concentration level (280 ppmv).
- Abrupt 4×CO₂: it runs for 460 years, consisting of an abrupt quadruplication of the atmospheric CO₂ concentration level from the piControl simulation.
- RCP4.5: it runs over the period 2006–2105 (100 years), forced by the time series of greenhouse gases level projected by the Representative Concentration Pathways 4.5 (RCP4.5), based on CMIP5 protocol. This simulation continues the historical simulation throughout the 21st century, reaching the radiative atmospheric forcing of 4.5 W m⁻² in 2100.
- RCP8.5: same as the RCP4.5 simulation, but forced by the time series of greenhouse gases level projected by the Representative Concentration Pathways 8.5 (RCP8.5), based on CMIP5 protocol; i.e., reaching the radiative atmospheric forcing of 8.5 W m⁻² in 2100.

Figure 3.1 - The scheme of principal simulations carried out by BESM-OA2.5 using different forcing conditions according to CMIP5 protocols.



The date for the Historical and RCPs simulations are from actual calendar years.
Source: Veiga et al. (2018).

3.3 Numerical Experiments

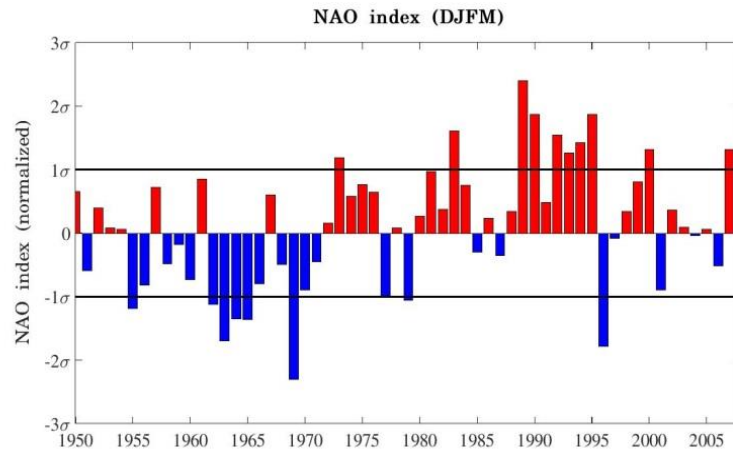
Three numerical experiments forced by specific atmospheric conditions are analyzed to assess the impact of different NAO phases on the SSTs over the tropical North Atlantic. In the first numerical experiment, the ocean model is forced by the observed atmospheric conditions from 1950 to 2007 (hereafter, Ocean-INTER). The Ocean-INTER simulation was already available. The ocean model is forced at each 6h by the atmospheric variables, surface air temperature (10 m), surface humidity (10 m), surface zonal and meridional wind components (10 m), sea level pressure (10 m) and is forced monthly by the precipitation; is forced daily by the solar radiation. The atmospheric forcing datasets are provided by Large and Yeager, (2009). The ocean model spin-up starts from rest and uses Levitus and Boyer (1994) climatology as the initial thermohaline structure. The model runs for 13 years with climatological atmospheric forcing fields, and then an additionally simulation of 58 years (1950–2007) forced by interannual atmospheric fields is performed. For both river discharges and sea ice forcings, are fixed to the climatological values. This is the Ocean-INTER simulation.

Additionally, two numerical experiments were carried out using the ocean-only model forced by the atmospheric fields constructed in a manner to simulate the effect of persisting the NAO-like conditions of the positive (Ocean-POS) and negative (Ocean-NEG) phases.

The outputs of the Ocean-INTER simulation are grouped in positive NAO composite and negative NAO composite. The NAO composite are based on the station-based Hurrell's NAO index (HURRELL, 2017), that is based on the difference of normalized sea level pressure between Lisbon, Portugal and Reykjavik, Iceland. Since the NAO is more active during the boreal winter, the NAO year consists from July to June, in which the year number is indicated by January (HURRELL et al., 2003). So, the NAO index value for a certain year is defined as the December-January-February-April (DJFM) averaged value, being January the reference for the year. The normalized NAO index time series with different phases is illustrated in Figure 3.2. Here, it is interested in positive NAO phase (i.e. $NAO > \sigma$) and in negative NAO phase (i.e. $NAO < -\sigma$). From Figure 3.2, the positive NAO composite are defined based on the years: 1973, 1983, 1989, 1990, 1992, 1993, 1994, 1995, 2000, 2007.

Conversely, the negative NAO composite are defined based on the years: 1955, 1962, 1963, 1964, 1965, 1969, 1977, 1979 and 1996. The SSTs and the atmospheric variables composites are averaged for the two NAO composite years listed above.

Figure 3.2 - NAO normalized index for DJFM based on dataset obtained from Hurrell, (2017).



Source: by the author.

In the case of Ocean-POS and Ocean-NEG experiments, the atmospheric forcing fields are constructed to resemble the NAO-like conditions of the positive (Ocean-POS) and negative (Ocean-NEG) phases. The years defined as NAO composites are used to construct the atmospheric composites for forcing conditions in the Ocean-POS and Ocean-NEG simulations. The atmospheric variables that force the ocean model are averaged over the composite years in order to generate average conditions of NAO positive and negative phases. These atmospheric fields are then cycled for a period of 60 years of simulation. Both experiments start from rest and use Levitus and Boyer (1994) climatology as the initial thermohaline structure.

In the case of Ocean-INTER, the first year to be included in a NAO composite is the year 1955, so the first 5 years of simulation outputs are discarded for the Ocean-INTER experiment. Regarding Ocean-POS and Ocean-NEG outputs, the first 5 years are also discarded.

3.4 Analysis methods

3.4.1 Data pre-processing

All analyses presented in the thesis are done using detrended datasets anomalies. Analysis using monthly datasets, the annual cycle was removed by subtracting climatological monthly means from the respective individual month. Detrended datasets are obtained by removing the linear trend based on a least squares regression. Prior to performing the analysis, all model's datasets were interpolated to the grid resolution of the respective reanalysis datasets used. In case of studies using different reanalysis datasets, the ERSSTv4 is used as the reference and the remaining variables were interpolated to its grid resolution.

3.4.2 Empirical Orthogonal Functions

To identify the main modes of climate variability the Empirical Orthogonal Function analysis (EOF; HANNACHI; JOLLIFFE; STEPHENSON, 2007) is used. The EOF is used in particular in section 4 to analyze the capacity of the model in simulating major modes of climate variability and compare them with observations. The EOF method is widely used in Climate Science due to its ability to compact information of the spatial and temporal variability of the original data series into new statistical modes. These statistical modes are linear combinations of the original data series, in which the linear combinations represent the maximum possible fraction of the spatial and temporal variability of the original data series. Generally, the first statistical modes, i.e. the ones which represent greater fraction of the variability, are the most important and they are likely to be the manifestation of a real phenomenon. Usually, in Climate Science the EOFs refer to the spatial mode and Principal Components (PCs) refer to the respective temporal mode. The EOF can be performed by firstly computing the covariance matrix of the original detrended data series anomalies ($[X']_{p \times n}$),

$$[C]_{p \times p} = \frac{1}{n-1} [X'] [X']^T, \quad (3.1)$$

with,

$$[X'] = \begin{bmatrix} x'_{11} & x'_{12} & \dots & x'_{1n} \\ x'_{21} & x'_{22} & \dots & x'_{2n} \\ \vdots & \vdots & \dots & \vdots \\ x'_{p1} & x'_{p2} & \dots & x'_{pn} \end{bmatrix}, \quad (3.2)$$

with p the number of spatial locations and n the number of samples measured at each location. Then, through the eigenvalue decomposition of $[C]$, the eigenvalues and eigenvectors of $[C]$ are obtained from:

$$[C]_{p \times p} [a]_{p \times m} = [a]_{p \times m} [\Lambda]_{m \times m}, \quad (3.3)$$

$m \leq \min(p, n)$ and represents the first m non-zero eigenvalues. The eigenvalues are generally sorted in the decreasing order. The k^{th} EOF is given by the k^{th} column of the eigenvector matrix $[a]$ and the respective k^{th} eigenvalue of the diagonal matrix $[\Lambda]$ represents the fraction of explained variance by this EOF mode. The percentage of the fraction of explained variance can be computed as:

$$\frac{\lambda_k}{\sum_{i=1}^m \lambda_i} \times 100\%, \quad (3.4)$$

in which λ_k is the k^{th} eigenvalue of $[\Lambda]$. Thus, this represents the variance explained by the k^{th} EOF mode. To compute the corresponding k^{th} PC (temporal mode), the original detrended data series anomalies ($[X']_{p \times n}$) is projected into the k^{th} EOF mode:

$$[PC]_{m \times n} = [EOF]^T_{m \times p} [X']_{p \times n}. \quad (3.5)$$

An important feature of the EOF analysis is the fact that the EOFs vectors are spatially orthogonal between each other and the PCs are uncorrelated at zero-lag between each other.

In this thesis, the EOFs are computed through the Singular Value Decomposition method (SVD). The application of the SVD to the data matrix $[X']$ yields following decomposition:

$$[X']_{p \times n} = [U]_{p \times m} [\Lambda]_{m \times m} [V]_{m \times n}^T, \quad (3.6)$$

in which, the index $m \leq \min(p, n)$, $[U]$ contains eigenvectors of $[X'] [X']^T$ and $[V]$ contains eigenvectors of $[X']^T [X']$, therefore the k^{th} EOF is the k^{th} columns of $[U]$ and the k^{th} PC is the k^{th} column of $[V]$. The singular values on the diagonal of $[\Lambda]$ are the square roots of nonzero eigenvalues of both $[X'] [X']^T$ and $[X']^T [X']$.

It should be noted that in the nomenclature of the transpose matrix ($[V]_{m \times n}^T$) used here, the rows/columns rearrangement shown represents already the resulting matrix dimensions after being transposed.

This brief resume of the EOF method is based on the references, Hannachi et al., (2007), Wilks (2011). For this thesis, the code developed to compute the EOF/PC is inspired in the reference Navarra and Simoncini (2010).

Since the reanalysis and models data set are on a regular latitude-longitude grid, therefore on an unequal area grid, prior performing the EOF calculations, the data were weighted by the square root of the cosine of latitude. The results of the EOF maps are shown as the original detrended data anomalies regressed onto the normalized Principal Component (PC) time series, i.e. by the standard deviation.

3.4.3 Maximum Covariance Analysis

To identify leading modes of covariability between two different geophysical fields the Maximum Covariance Analysis (MCA; BRETHERTON et al., 1992) is used. The MCA is the method used to obtain the AMM, i.e. the leading mode of covariability between the SST and the surface wind components in the tropical Atlantic. The MCA is based on the decomposition of the covariance matrix of two geophysical fields through the SVD and aims to find pairs of linear combinations between the fields that maximize the spatial patterns of anomalous covariability between them (one pattern for each field). The covariance matrix of two detrended data series anomalies ($[X']_{p \times n}$ and $[Y']_{q \times n}$) is given as,

$$[C]_{p \times q} = \frac{1}{n-1} [X'] [Y']^T. \quad (3.7)$$

By applying the SVD to the covariance matrix,

$$[C]_{p \times q} = [U]_{p \times m} [\Lambda]_{m \times m} [V]_{m \times q}^T, \quad (3.8)$$

in which, the index $m \leq \min(p, n)$, $[U]$ contains eigenvectors of $[X']$ and $[V]$ contains eigenvectors of $[Y']$, therefore the k^{th} EOF of $[X']$ is the k^{th} columns of $[U]$ and the associated k^{th} EOF of $[Y']$ is the k^{th} column of $[V]$. Here, EOFs mean maximum spatial patterns of covariability between the two fields. The singular values on the diagonal of $[\Lambda]$ are the square roots of nonzero eigenvalues of $[X'] [Y']^T$. The time

series or expansion coefficients (EC) of each spatial pattern can be obtained by projecting the spatial pattern onto the respective original detrended data series anomalies,

$$[EC_x]_{m \times n} = [EOF_x]^T_{m \times p} [X']_{p \times n}, \quad (3.9)$$

$$[EC_y]_{m \times n} = [EOF_y]^T_{m \times q} [Y']_{q \times n}. \quad (3.10)$$

The rows of $[EC_x]$ and $[EC_y]$ contain the expansion coefficients of fields $[X']$ and $[Y']$, respectively. The percentage of the squared covariance fraction for each k^{th} spatio-temporal pattern for each, which is maximized by MCA application, can be computed as:

$$\frac{\lambda_k^2}{\sum_{i=1}^m \lambda_i^2} \times 100\%, \quad (3.11)$$

in which λ_k is the k^{th} eigenvalue of $[\Lambda]$.

The results of the MCA maps can be shown as the original detrended data anomalies regressed onto the normalized EC time series, i.e. by the standard deviation. In the case of the AMM, the EC for the SST is used to plot both fields. Therefore the AMM maps show the homogeneous SST structure and the heterogeneous surface wind structure.

This brief resume of the MCA method is based on the references Wilks (2011) and Venegas (2001).

3.4.4 Other statistical analyses

In this study, it is used the Pearson correlation coefficient, both synchronous (zero-lag) and lead-lag, to infer potential statistical link between different phenomena. The correlation coefficient between two detrended data series anomalies ($[X']_{1 \times n}$ and $[Y']_{1 \times n}$) is given by,

$$r_{xy} = \frac{\sum_{i=1}^n X'_i Y'_i}{[\sum_{i=1}^n (X'_i)^2]^{1/2} [\sum_{i=1}^n (Y'_i)^2]^{1/2}}. \quad (3.12)$$

The lead-lag correlation coefficient is obtained through,

$$r_{xy}(k) = \frac{\sum_{i=1}^{n-k} X'_i Y'_{i+k}}{[\sum_{i=1}^{n-k} (X'_i)^2]^{1/2} [\sum_{i=k+1}^n (Y'_i)^2]^{1/2}}, \quad (3.13)$$

in which the k is the time lag between the variables. The detrending and removed averaged should be done in the new constructed time lag data series.

Spatial patterns based on lead-lag regression maps are analyzed in the section 6. These patterns are plotted by computing the regression coefficient between each grid point time series of a field and the time series in which the field is being projected. The linear regression coefficient between two detrended data series anomalies (time series $[X']_{1 \times n}$ and the field $[Y']_{p \times n}$) is given by,

$$b = \frac{\sum_{i=1}^n X'_i Y'_{m,i}}{\sum_{i=1}^n (X'_i)^2} = \frac{Cov(X'Y'_m)}{Var(X')}, \quad (3.14)$$

in which m is an arbitrary grid point.

In order to assess the statistical significance of the correlation and the linear regression coefficient between two autocorrelated time series, as are the case of low-pass filtered datasets, it is used a two-tailed Student's t-test with an effective number of degrees of freedom N^{eff} given by the approximation,

$$\frac{1}{N^{eff}(j)} \approx \frac{1}{N} + \frac{2}{N} \sum_{j=1}^N \frac{N-j}{N} \varrho_{xx}(j) \varrho_{yy}(j), \quad (3.15)$$

in which N is the sample size and $\varrho_{xx}(j)$ and $\varrho_{yy}(j)$ are the autocorrelations of two sampled time series X and Y at time lag j (PYPER; PETERMAN, 1998; LI; SUN; JIN, 2013; SUN et al., 2017). Correlation coefficients are considered significant at 95% confidence level.

In this work, in order to evaluate the periodicity of the phenomena it is applied the power spectrum technique based on Fourier Analysis on the normalized time series, in which the normalization is done by their long-term monthly standard deviation.

The information of this subsection was obtained in the reference Wilks (2011).

4 CLIMATE VARIABILITY SIMULATED BY BESM-OA2.5

In this section, the performance of the BESM-OA2.5 in simulating the most prominent global climate variability patterns over the historical period is evaluated. Following climate model validation procedure, in which the atmospheric and oceanic main variabilities are validated against reanalysis datasets, the evaluation particularly focuses the most important large-scale climate variability patterns simulated in the historical run, which is forced by observed CO₂ equivalent atmospheric concentration. This allows us to infer the ability of the model in simulating atmospheric and oceanic variabilities in the climate system correctly. The model's ability in simulating large-scale variabilities indicates its usefulness for the study aimed at this thesis. Note that the Atlantic Meridional Mode is evaluated in chapter 5. The complete evaluation of BESM-OA2.5 Historical simulation has been submitted to Geoscientific Model Development under the title: The Brazilian Earth System Model version 2.5: Evaluation of its CMIP5 historical simulation (VEIGA et al., 2018).

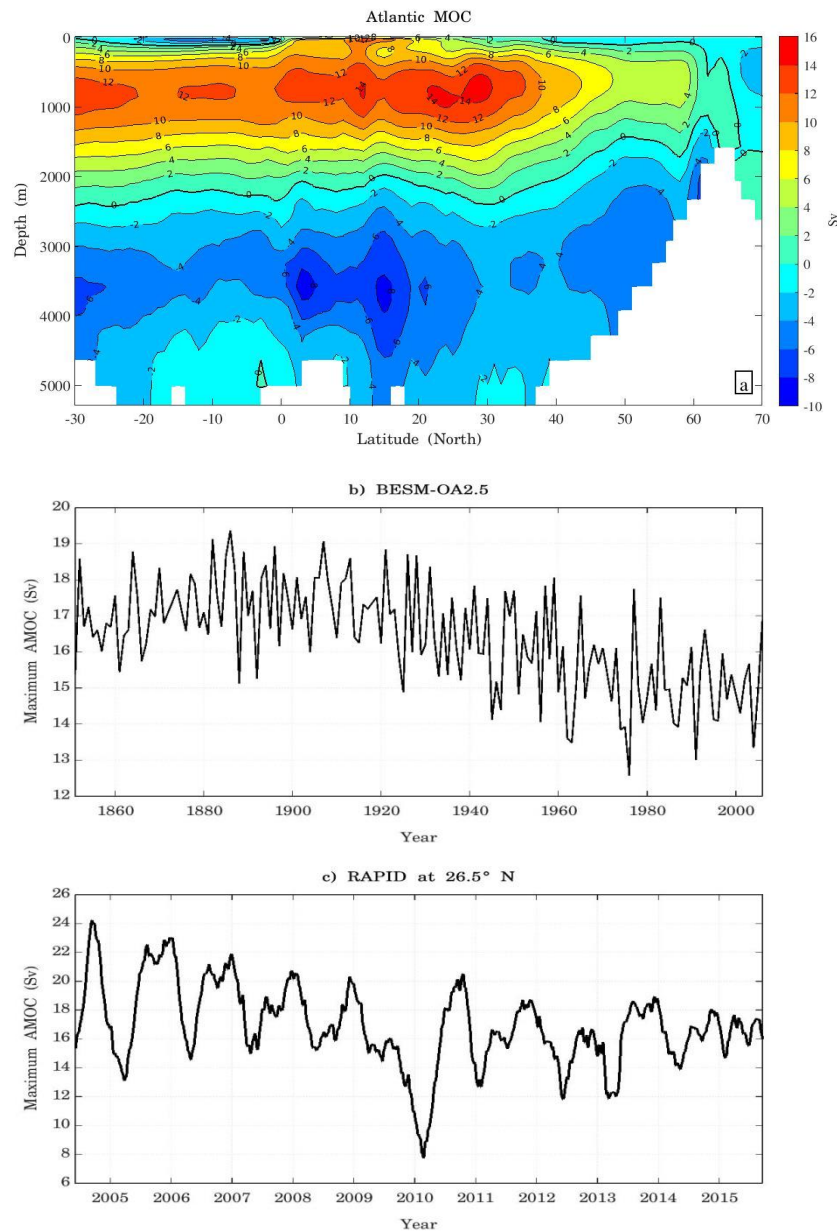
4.1 Atlantic Meridional Overturning Circulation

The AMOC in the BESM-OA2.5 historical run simulates the two overturning cells, with northward water flux in the upper limb (from the surface up to ~1000 m) of the upper overturning cell and the southward water flux in the deeper layers of the upper overturning cell (~1000 m up to ~4000 m); and the northward AABW in the ocean floor in the lower overturning cell, although is not so prominent (Figure 4.1a). Very similar AMOC structure is described in Lumpkin and Speer (2007) based on observations measurements. The annual mean maximum AMOC strength simulated by BESM-OA2.5 is about 15 Sv ($1 \text{ Sv} \equiv 10^6 \text{ m}^3 \text{ s}^{-1}$) between 25° N and 30° N at about 850 m depth (Figure 4.1a). This maximum value is within the 17.2 ± 4.6 Sv mean strength (with a 10 day filtered root mean square variability of 4.6 Sv) observed by the project RAPID at 26.5° N (MCCARTHY et al., 2015). It is also in the range of maximum volume transport strength simulated by the state-of-the-art models of the CMIP5 (WEAVER et al., 2012; CHENG; CHIANG; ZHANG, 2013). Figure 4.1b shows the maximum annual mean AMOC strength time series for the historical period at the 30° N. Figure 4.1c plots the AMOC maximum volume transport strength

measured by the Rapid project over the period April/2004 to October/2015 at the latitude of 26.5° N (http://www.rapid.ac.uk/rapidmoc/rapid_data/datadl.php).

Averaging the maximum AMOC strength over the first and the last 30 years of the time series, i.e. over the periods 1850–1879 and 1976–2005 respectively, the result shows a decrease of 11.2%, from 16.9 Sv to 15.1 Sv in each period, respectively. However, a more profound study is necessary to infer whether such a decline is a consequence of coupled model drifting due to the spinup or other processes. It is noteworthy to refer that the observed negative trend from RAPID is higher than the one that climate models project for the next hundred years (FARNETI, 2017). Modeling results indicate that the AMOC has a multidecadal cycle, however, the power spectrum of its strength time series do not show a multidecadal oscillation. The standard deviation of the detrended maximum AMOC strength time series is 1.4 Sv.

Figure 4.1 - The Atlantic Meridional Overturning Circulation simulated by BESM-OA2.5.



(a) Atlantic Meridional Overturning Circulation averaged for the period 1971–2000. (b) Annual mean maximum AMOC strength time series at the latitude 30° N simulated by BESM-OA2.5 for historical simulation over the period 1850–2005. c) The maximum AMOC strength time series measured by the project RAPID at 26.5° N over the period April/2004 to October/2015. The RAPID time series is smoothed by a 3-month running average. Units are in Sverdrup.

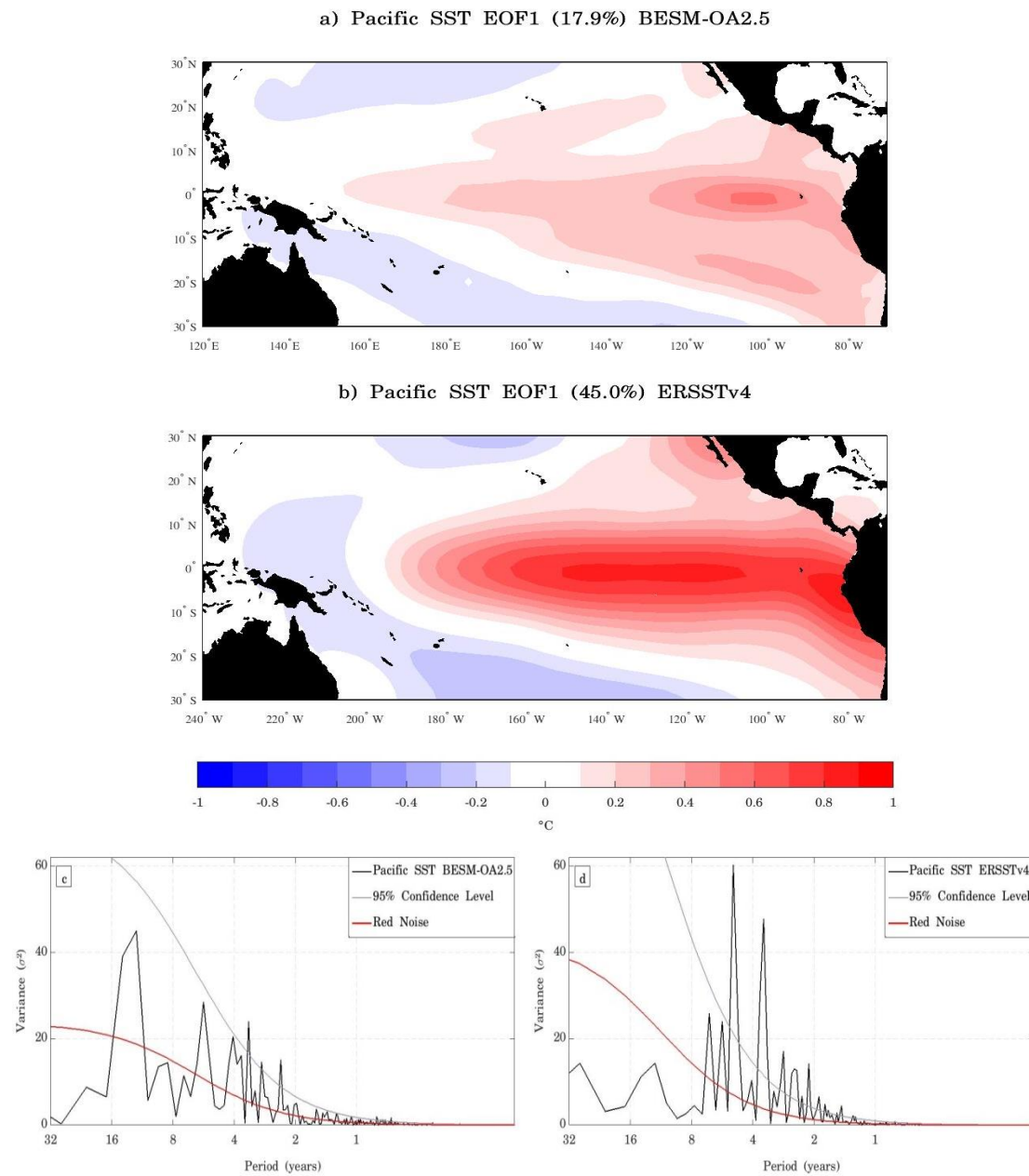
Source: by the author.

4.2 El Niño-Southern Oscillation

There are many methods to evaluate the ENSO variability. In the present study, it is applied the EOF to detrended monthly SST anomalies over the tropical Pacific ocean

(30° S–30° N; 240°–70° W) for the period 1950–2005 for both BESM-OA2.5 simulations and ERSSTv4 data. Figures 4.2a and 4.2b show the leading EOF patterns associated with the El Niño/La Niña variability. The model simulates the El Niño/La Niña variability deficiently, with lower amplitude of SST variability and the center of maxima variability confined to the eastward part of the basin. The model's leading EOF explains 17.9% of the total variance, substantially less than the 45% explained by observations. The lower amplitude of the simulated El Niño/La Niña can be verified in the power spectrum of the leading Principal Component (PC) shown in Figure 4.2. Even though the simulation shows two significant peaks between 2–4 years cycle (Figure 4.2c), which is within the range of the period cycle given by the leading PC of observations (3–7 years cycle; Figure 4.2d), the amplitude of the simulated variance is lower than that of observations. Different climate models have shown deficient ENSO simulation due to a weak ocean dynamic response to the wind interannual anomalies, impacting the influence that the thermocline has on the ENSO variability (KIM; JIN, 2011; BELLENGER et al., 2014)

Figure 4.2 - The leading EOF modes of the detrended monthly SST anomalies over the Tropical Pacific region (30° S–30° N; 240°–70° W).

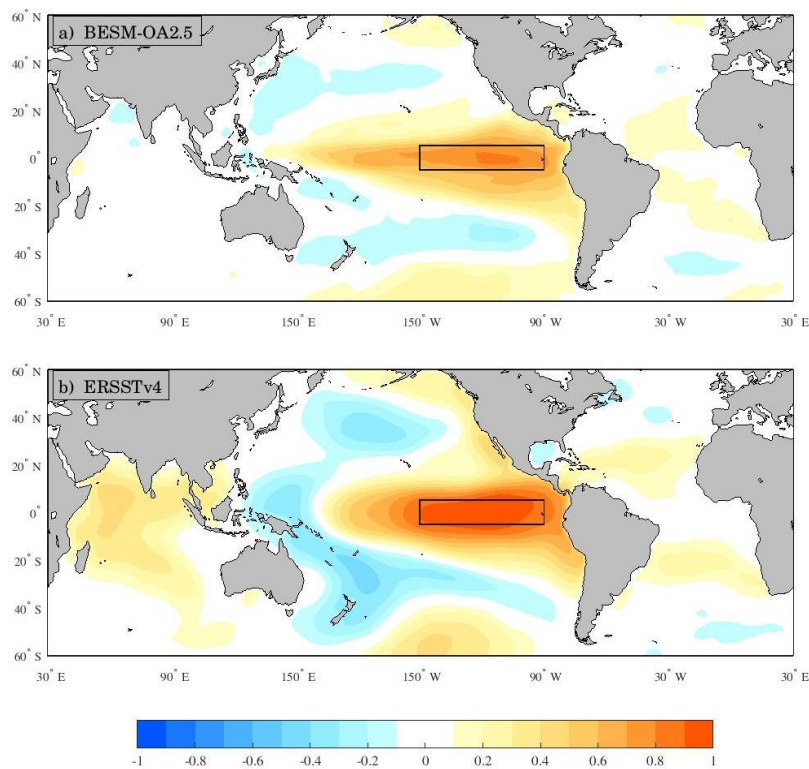


(a) BESM-OA2.5 and (b) ERSSTv4. The results are shown as the SST anomalies regressed onto the corresponding normalized PC time series (°C per standard deviation) over the period 1950–2005. The percentage of the variance explained by each EOF is indicated in the title of the figure. The contour interval is 0.1 °C. Figures (c) and (d) are the power spectrum of the leading joint PC time series of the pattern for BESM-OA2.5 and ERSSTv4, respectively. The solid red line represents the theoretical red noise spectrum and the gray line represents the 95% confidence level.

Source: by the author.

Figure 4.3 shows the spatial correlation between detrended monthly anomalies of Niño-3 index (defined inside the black rectangle area, bounded by 5° S–5° N, 90°–150° W) and detrended monthly anomalies of global SST computed for BESM-OA2.5 and ERSSTv4 over the period 1900–2005. The model has not a strong correlation at grid points inside the Niño-3 area, which is a signal that the El Niño/La Niña spatial pattern is weakly simulated. The horseshoe pattern of negative correlation observed in the Pacific Ocean is also weakly simulated by the model, particularly in the westward equatorial part. The positive correlation of observed SST over the Indian Ocean and Niño-3 index is absent in the model’s simulation. It is worth mentioning that the model simulates the observed correlation pattern of SST anomalies over the Atlantic Ocean with Niño-3 index.

Figure 4.3 - Spatial maps with the monthly correlation between Niño-3 index and global SST anomalies.



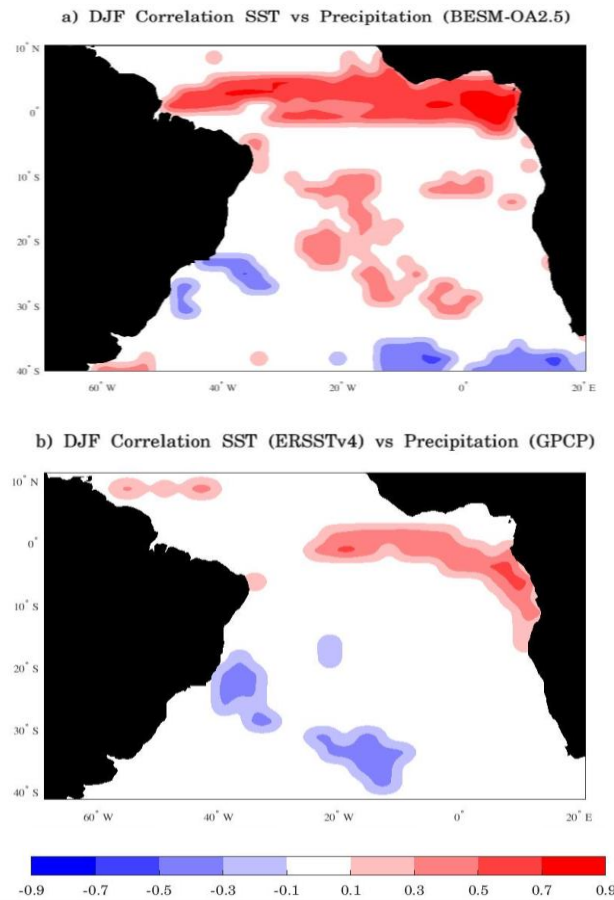
(a) BESM-OA2.5 and (b) ERSSTv4 over the period 1900–2005. The anomalies are obtained by subtracting the monthly means for the whole detrended time series at each grid point. Black rectangles show the Niño-3 index region. Shaded areas are statistically significant at the 95% confidence level (through two tailed t-student test).

Source: by the author.

4.3 South Atlantic Convergence Zone

Following Nobre et al., (2012), a correlation between seasonal precipitation and SST anomalies for the austral summer (DJF) over the tropical South Atlantic (40° S– 10° N; 70° W– 20° E) over the period 1979–2010 for observations and for the period 1971–2002 for the model, so 32 years are used. Figure 4.4 shows the rainfall-SST anomaly correlation maps for both BESM-OA2.5 and observations. BESM-OA2.5 is able to simulate an inverse correlation between precipitation and SST in the southeast of Brazil (near 20° S), suggesting the capacity of simulating precipitation over cooler SST, a feature related to the formation of SACZ (that tends to cooler the SST). It is noteworthy in Figure 4.4 that BESM-OA2.5 is capable to generate both positive and negative SSTA-rainfall correlations over the equatorial Atlantic (positive, thermally direct driven circulation over the equatorial region and negative, thermally indirect driven atmospheric circulation over the SW tropical Atlantic, Figure 4.4a, a feature also present in the observation correlation map of Figure 4.4b).

Figure 4.4 - Spatial maps with the correlation between SST and precipitation (seasonal average DJF) over the South Ocean (40° S–10° N; 70° W–20° E).



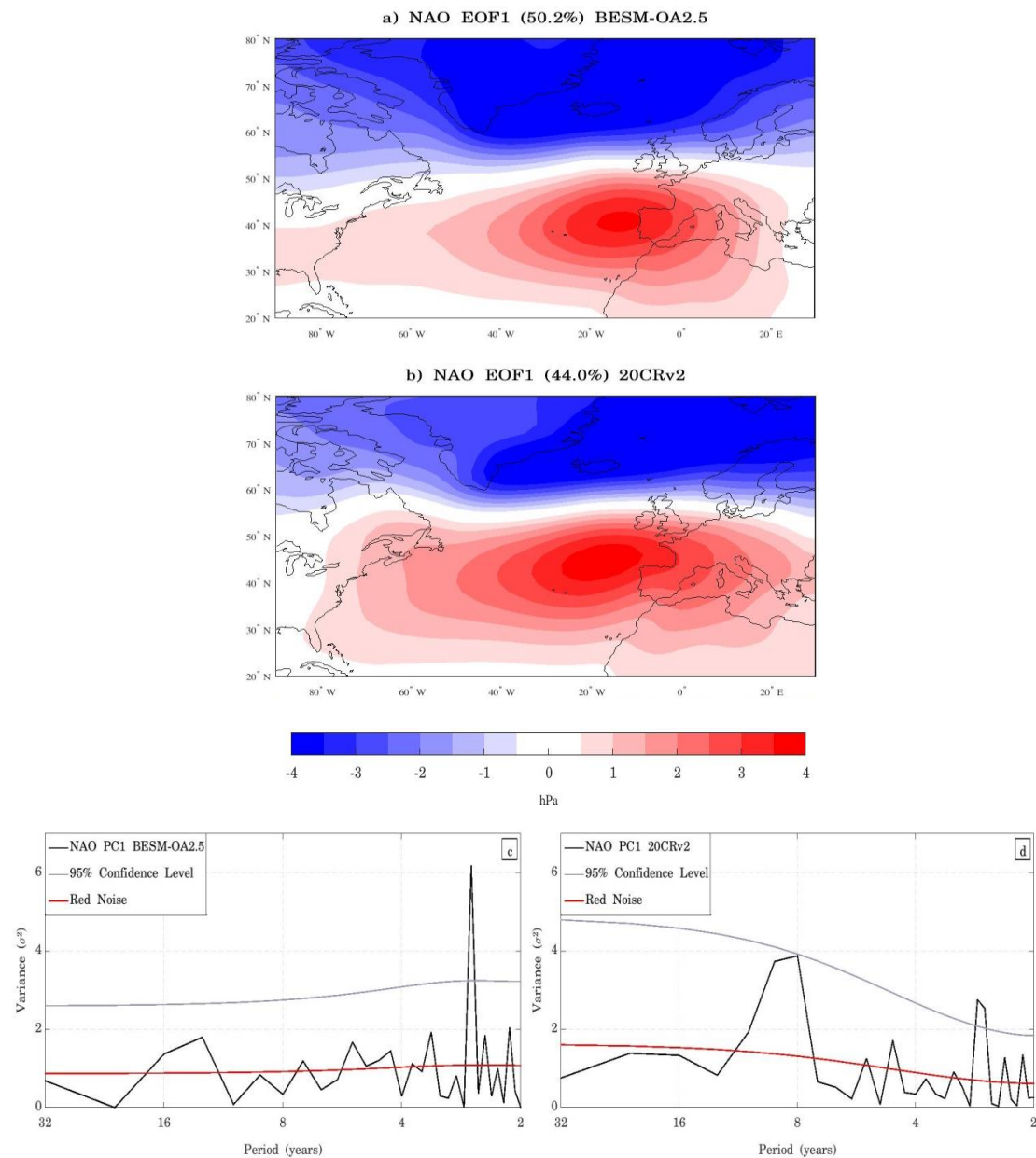
(a) BESM-OA2.5 over the period 1971–2002 and (b) observations over the period 1979–2010. Shaded areas are statistically significant at the 95% confidence level (through two tailed t-student test). Source: by the author.

4.4 North Atlantic Oscillation

The leading EOF of the SLP averaged for the boreal winter season (DJF) in the Euro-Atlantic region shows that the NAO is well simulated by BESM-OA2.5 (Figure 4.5a), simulating the NAO dipole centers and their amplitudes very similar to the observed pattern (Figure 4.5b). The variances explained by the leading EOF are also similar, 50.2% and 44% for BESM-OA2.5 and reanalysis, respectively. Since NAO is more active during the boreal winter, the analyses use data from this season. The period used to perform the analyses is 1950–2005. The spectral analysis of the leading PCs shows that BESM-OA2.5 captures the ~2.5 years cycle on the time variability but fails to capture the ~8 years cycle (Figure 4.5c and d). It is interesting to note that

BESM-OA2.5 simulates a NAO spatial pattern, without capturing its low-frequency variability. By analyzing the NAO variability, we consider that it is not necessary to analyze the Northern Annular Mode (NAM) since both are the manifestation of the same mode of variability (HURRELL; DESER, 2010).

Figure 4.5 - The leading EOF modes of the boreal winter (DJF) seasonal averaged SLP anomalies for the Euro-Atlantic region (20°–80° N; 100° W–30° E).



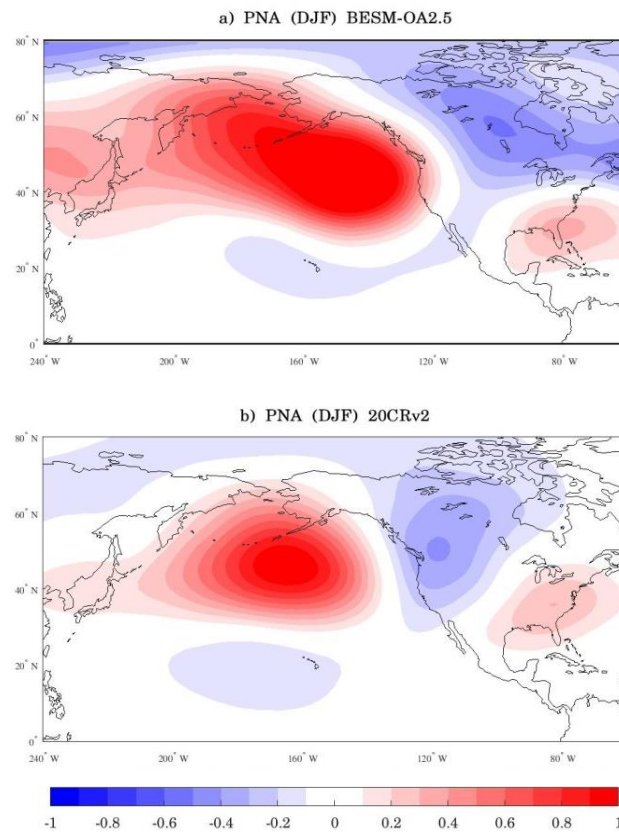
(a) BESM-OA2.5 and (b) 20CRv2. The results are shown as the SLP anomalies regressed onto the corresponding normalized PC time series (hPa per standard deviation) for the period 1950–2005. The percentage of the variance explained by each EOF is indicated at the title of the figure. The contour interval is 0.5 hPa. Figures (c) and (d) are the power spectrum of the leading PC time series of the NAO pattern for BESM-OA2.5 and 20CRv2, respectively. The solid red line represents the theoretical red noise spectrum and the gray line represents the 95% confidence level.

Source: by the author.

4.5 Pacific-North America Pattern

Similar to NAO, the PNA has its largest variation of amplitude during the boreal winter; therefore, the present analysis is performed for this season. Following Wallace and Gutzler, (1981), we construct one-point correlation maps for BESM-OA2.5 and 20CRv2 Reanalysis in order to evaluate the capacity of the model to reproduce the PNA pattern. The one-point correlation maps correlate 500 hPa geopotential height at the reference point (45° N, 165° W) with all the other grid points of the map domain (0° – 80° N; 240° – 70° W). The time series used to perform the correlations are averaged boreal winter seasonal (DJF) dataset over the period 1950–2005. The time series are departed from their long-term mean and normalized at each grid point prior the correlation computation. Figure 4.6 shows the one-point correlation maps for BESM-OA2.5 (Figure 4.6a) and 20CRv2 (Figure 4.6b). In this figure, it is possible to check the four centers of action simulated by the model, which shows a stronger correlation between the four high pressure centers when compared with reanalysis correlation maps in Figure 4.6b.

Figure 4.6 - One-point correlation map for North Pacific.



(a) BESM-OA2.5 and (b) 20CRv2 reanalysis showing the correlation coefficient of 500 hPa geopotential level based at 45° N, 165° W and the other grid points. The time series used are boreal winter seasonal (DJF) averaged dataset for the period 1950–2005.

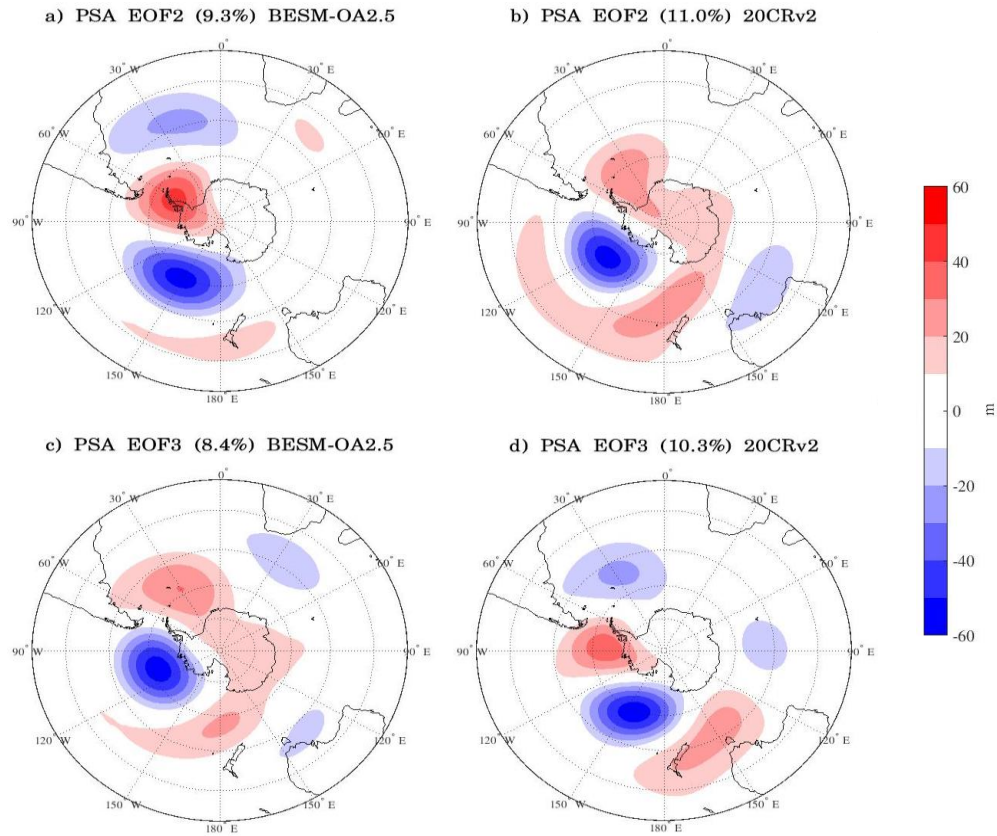
Source: by the author.

4.6 Pacific-South America Modes

Figures 4.7a and 4.7b show the PSA modes both simulated by BESM-OA2.5 and from reanalysis. As the explained variance of EOF2 and EOF3 are close, the EOFs seem to degenerate for both reanalysis and model simulation. In order to relax the orthogonality constraint, it is performed a rotated EOF (REOF) retaining the first 10 modes. The REOF2 and REOF3 resemble the EOF2 and EOF3 respectively, implying that they are independent modes. The PSA modes are well simulated by BESM-OA2.5, although the model changes the order of the EOF patterns. BESM-OA2.5 shows an anomaly south of South Africa (Figure 4.7c) that does not appear in the reanalysis (Figure 4.7b). PSA modes have significant interannual and decadal variabilities (ZHANG; MA; WU, 2016). PSA modes simulated by BESM-OA2.5

have only significant variability in the interannual scale, with absent decadal variability.

Figure 4.7 - The second and third EOF modes of the monthly mean 500 hPa geopotential height field for the Southern Hemisphere (20°–90° S).



(a) and (c) The second and third EOF modes of the monthly mean 500 hPa geopotential height field for the Southern Hemisphere (20°–90° S) for BESM-OA2.5. (b) and (d) The second and third EOF modes of the monthly mean 500 hPa geopotential height field for the Southern Hemisphere (20°–90° S) for 20CRv2 reanalysis. The results are shown as the 500 hPa geopotential height regressed onto the corresponding normalized PC time series (meters per standard deviation) over the period 1950–2005. The percentage of the variance explained by each EOF is indicated at the title of the figure. The contour interval is 10 m.

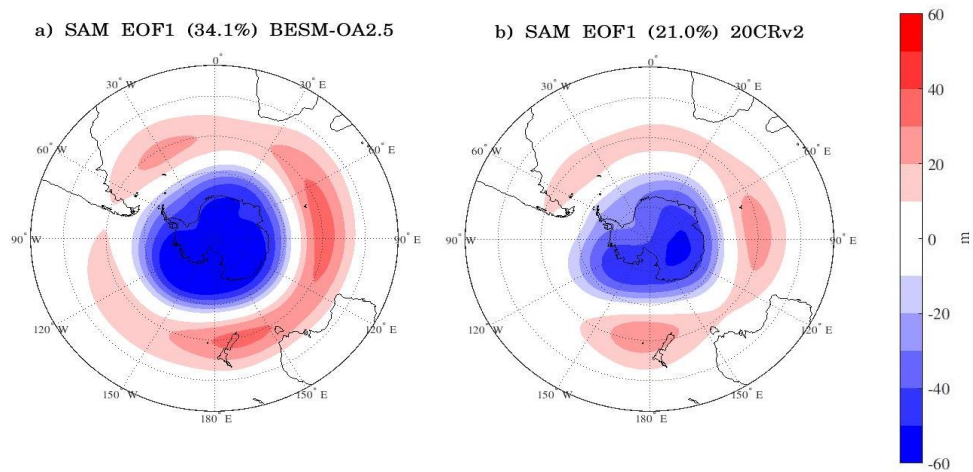
Source: by the author.

4.7 Southern Annular Mode

To evaluate the capacity of BESM-OA2.5 to simulate this atmospheric mode of variability, EOF analysis is applied to the monthly mean 500 hPa geopotential height field from 20° S to 90° S, over the period 1950–2005, for both model and Reanalysis. The SAM pattern simulated by BESM-OA2.5 resembles very well the observed pattern, with the mid-latitude 500 hPa geopotential height variation centers depicted

in the same longitudes as observations, but with differences in the amplitude values (Figure 4.8). However, the explained variance is higher compared with observation. The explained variances of BESM-OA2.5 and 20CRv2 are 34.1% and 21.0%, respectively. The reason for a higher variance explained by the model is not clear, although the CMIP5 models tend to explain higher variance compared with reanalysis (ZHENG et al., 2013). The SAM is a quasi-decadal mode of variability (see YUAN; YONEKURA, 2011), however, the BESM-OA2.5 power spectrum reveals a SAM with a markedly interannual variability, without the peak between 8 and 16 years as obtained in the reanalysis.

Figure 4.8 - The leading EOF modes of the monthly mean 500 hPa geopotential height fields for the Southern Hemisphere (20°–90° S).



(a) BESM-OA2.5 and (b) for 20CRv2 Reanalysis. The results are shown as the 500 hPa geopotential height regressed onto the corresponding normalized PC time series (meters per standard deviation) over the period 1950–2005. The percentage of the variance explained by each EOF is indicated at the title of the figure. The contour interval is 10 m.

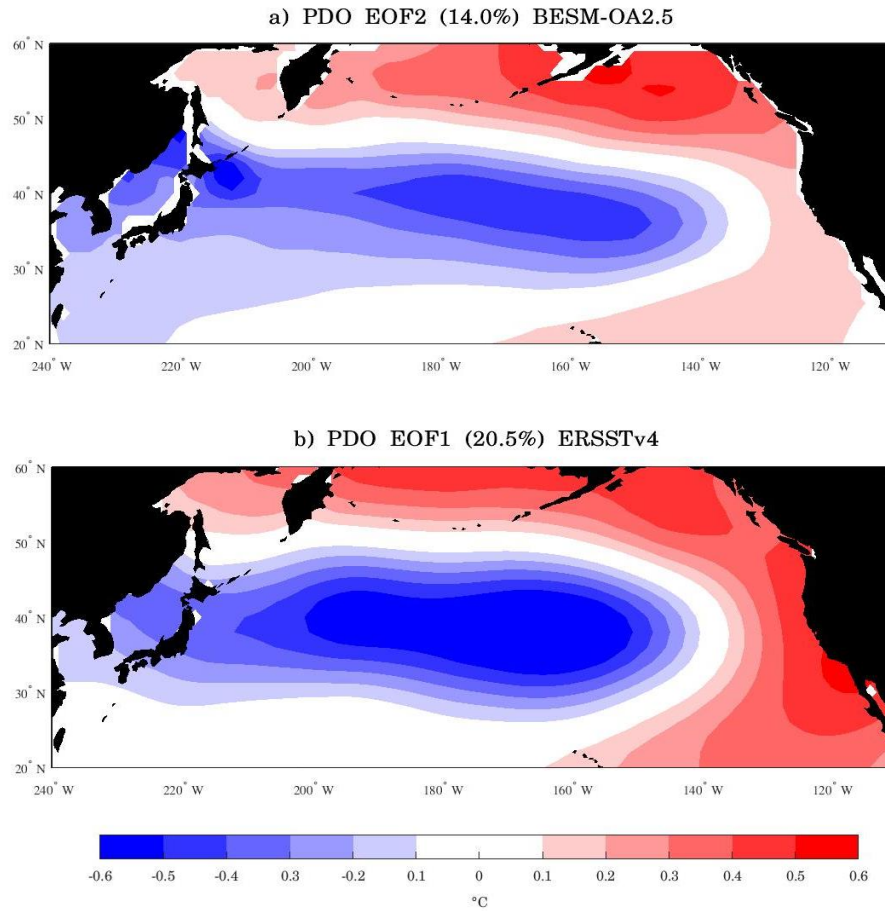
Source: by the author.

4.8 Pacific Decadal Oscillation

Following the definition (MANTUA et al., 1997), the spatial pattern of PDO is obtained by regressing the SST anomalies onto the leading normalized PC time series, shown in Figure 4.9 which in this case is showing the positive phase of the PDO. The EOF is applied to monthly SST anomalies over North Pacific (20°–60° N; 240°–110° W) over the period 1900–2005. BESM-OA2.5 is not capable of reproducing this pattern by the leading EOF. The PDO pattern only appears on the second EOF (Figure 4.9a), with the explained variance of 14.0% against 20.5% of observations (Figure

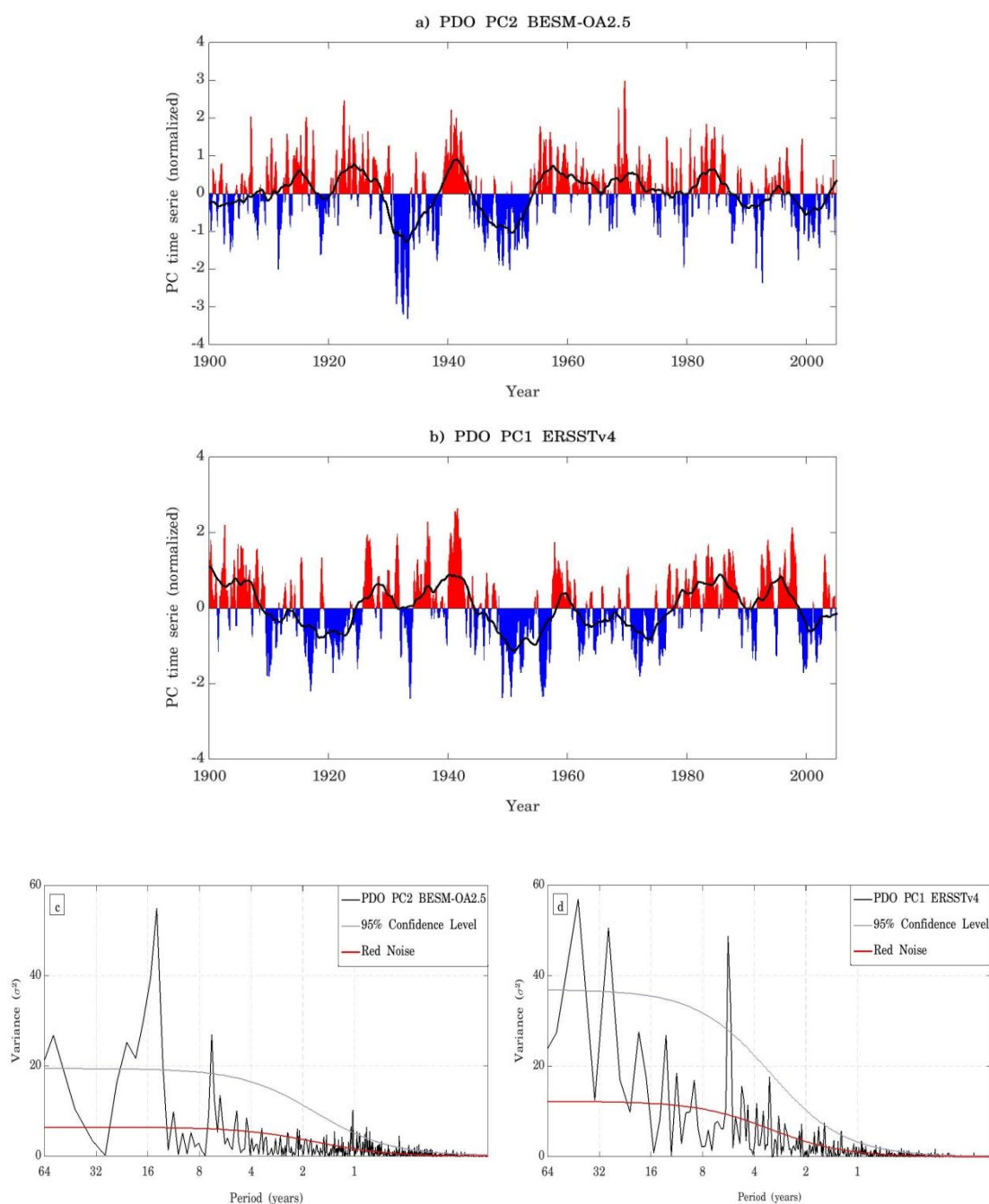
4.9b). Although the EOF2 resembles the PDO mode, the tropical part has a weaker variation than the observation. The reason of incapacity of the model in reproducing the PDO as the leading mode of variability is probably due to the model's simulation of weaker ENSO variability, both in spatial and temporal scales. These deficiencies may impact the mechanisms that reproduce the PDO, mainly via the “atmospheric bridge” as referred earlier. Figures 4.10a and 4.10b show the normalized PC2 and PC1 time series of BESM-OA2.5 and ERSSTv4, respectively. It is possible to note that both time series present a multidecadal periodicity, but in different time scales as it is confirmed by the power spectrum (Figure 4.10c and 4.10d). The power spectrum shows that both time series present interannual periodicity (~5-6 years), with BESM-OA2.5 multidecadal variability strongest spectrum around 15 years, a higher frequency compared with observation (~22 and ~40-45 years).

Figure 4.9 - The EOF modes of the detrended monthly SST anomalies for the North Pacific (20°–60° N).



(a) The second EOF mode of monthly SST anomalies of BESM-OA2.5 and (b) the leading EOF mode of monthly SST anomalies of ERSSTv4, both over North Pacific Ocean (20°–60° N; 240°–110° W). The results are shown as the monthly SST anomalies regressed onto the corresponding normalized PC time series (°C per standard deviation) over the period 1900–2005. The percentage of the variance explained by each EOF is indicated at the title of the figure. The contour interval is 0.1 °C. Source: by the author.

Figure 4.10 - The Principal Component time series of the PDO modes.



Normalized second PC time series for (a) BESM-OA2.5 and normalized leading PC time series for (b) ERSSTv4 over the period 1900–2005. The solid black lines are the 5-year running average. Figures (c) and (d) are the power spectrum of the second PC time series for BESM-OA2.5 and for the leading PC time series for 20CRv2, respectively. The solid red line represents the theoretical red noise spectrum and the gray line represents the 95% confidence level.

Source: by the author.

4.9 BESM Simulation Summary

Large-scale phenomena simulated by the new version of the coupled ocean-atmosphere component of the Brazilian Earth System Model version 2.5 (BESM-OA2.5) is evaluated for the historical period (1850-2005). The ENSO is simulated with lower amplitude of variability than the observations and such weak ENSO seems to impact other Pacific variability patterns such as the PDO. In the case of Atlantic climate variabilities, BESM-OA2.5 simulations capture very well the main phenomena. The AMM that is very well simulated by the model in term of the spatial pattern and temporal variability. It is also relevant to highlight BESM-OA2.5 ability to represent the enhanced rainfall over cooler waters over the SW Tropical Atlantic, associated with the South Atlantic Convergence Zone (SACZ). Another key phenomenon of the climate system is the Atlantic Meridional Overturning Circulation (AMOC), which is well reproduced by BESM-OA2.5, with the meridional overturning structure comparable with the observed data and the best simulations performed by CMIP5 models. BESM's maximum AMOC strength average value slighter lower than the average value that has been observed by the project RAPID. The Euro-Atlantic atmospheric variability that characterizes the NAO is very well simulated by BESM-OA2.5 even when compared with the CMIP5 models (NING; BRADLEY, 2016). In the higher latitudes, BESM-OA2.5 is capable to reproduce fairly well majors atmospheric variabilities in both Hemispheres, as the Pacific-North American (PNA), the Pacific-South American (PSA) and the Southern Annular Mode (SAM) teleconnections patterns. However, the model lacks to simulate lower frequencies (decadal time-scale) that NAO, PSA, and SAM shown in the observations. This can be related to the fact that the model configuration (low top) does not represent stratospheric mechanisms that influence and are coupled with tropospheric variabilities (SCAIFE et al., 2005; KIDSTON et al., 2015).

5 AMM IN FOUR STATE-OF-THE-ART MODELS

The evaluation of the AMM simulated by four state-of-the-art Climate/Earth System Models is presented here. The models used are BESM-OA2.5, CanESM2 (CHYLEK et al., 2011), HadGEM2-ES (COLLINS et al., 2011) and MPI-ESM-MR (GIORGETTA et al., 2013). Note that an evaluation of BESM-OA2.5 is shown in section 4. Table 5.1 shows the description of the models, presenting the center and the country each one belongs, the CMIP5 model abbreviations, the ensemble, the atmosphere and ocean resolutions. The models are chosen in order to diversify the sort of their respective components. BESM-OA2.5 uses the Modular Ocean Model (MOM) as its oceanic model component. The remaining models chosen do not have MOM as their oceanic model component. In order to be comparable with the observations, Historical simulations are used. All models AMM are computed over the period 1900-2005 (106 years). As mentioned earlier, the quality of the Intergovernmental Panel on 5 Climate Change (IPCC) fifth assessment report (AR5) models in simulating the AMM are considered low (FLATO et al., 2013, table 9.4). Nevertheless, the mode has not been extensively evaluated using the methodology presented in chapter 3. To my knowledge, Amaya et al., (2017) is the first to report such an evaluation. In their study, in which the AMM features are analyzed based on multi-model mean, it is reported that the AMM is not always the leading mode of coupled variability in the Tropical Atlantic. Here, by analyzing four models it is possible to track the main differences between them and relative to the observations.

Table 5.1 - The description of the models used to compute the AMM.

Institute	Model	Simulation	horizontal resolution (lat×lon)	
			Atmosphere	Ocean
Brazilian National Institute for Space Research (Brazil)	BESM-OA2.5	Historical GHG r1i1p1	1.875° × 1.875°	0.25°, 1°×1°
Canadian Centre for Climate Modelling and Analysis (Canada)	CanESM2	Historical r1i1p1	2.791°×2.813°	0.93°,1.141° ×1.406°
Met Office Hadley Centre (UK)	HadGEM2-ES	Historical r1i1p1	1.25°×1.875°	0.340°, 1°×1°
Max Planck Institute for Meteorology (Germany)	MPI-ESM-MR	Historical r1i1p1	1.875°× 1.875°	802×404 (tripolar)

Models with higher resolution in the tropical region and a decreasing resolution towards the poles have two values for latitude in their respective oceanic resolution column. Models with an oceanic tripolar grid, the number of grid points in each coordinate are presented.

Source: by the author.

5.1 Models Results

Figure 5.1 shows different features of the AMM simulated by BESM-OA2.5. The spatial pattern is well simulated by the model, with the interhemispheric SSTA gradient well depicted in its meridional structure. The northern SSTA tend to be weaker than the observations and the southern SSTA pattern is constrained to southwestern African coast compared with the widely spread SSTA observed in the TSA (Figs. 3.1a, 5.1a). Figure 5.1a also shows that the surface wind anomalies tend to be weaker compared with the observations, in particular in the TNA. This indicates that the model underestimates the AMM coupled variability strength, that is also reflected in 47% of the explained covariance between SSTA and surface wind anomalies, slightly lower than the observed one (56.0%). The SST and 10-m wind expansion coefficients have a zero-lag correlation of 0.65, lower than obtained in the observations (0.76) (Figure 3.1b, 5.1b). The important feature of the AMM variability is its dominant decadal periodicity. BESM-OA2.5 captures this temporal variability although it is significant at 90%, whereas the observed spectral is significant at 95% (Figure 3.1c, 5.1c). The model also captures the AMM interannual variability. BESM-

OA2.5 month-to-month variance of the surface wind components is reasonably well simulated both for the monthly variance values and the seasonal variability. The model peaks at Dec-Jan-Feb whereas the peak in the observations occurs in Jan-Feb-Mar. However, the SST month-to-month maximum variance simulated by the model occurs in Oct-Nov-Dec, distinct from the observed season Mar-Apr-May (Figure 3.1d, 5.1d). Finally, through the lead-lag correlation between the SST and wind expansion coefficients, it is possible to see that the model correctly indicates that the surface winds lead the SSTA in the AMM simulation, with maximum correlation of ~ 0.77 when AMM-Wind leads by a month the AMM-SST, very similar to the observations, in which the AMM-Wind leads by a month the AMM-SST with a maximum correlation of 0.79 (Figure 3.1e, 5.1e).

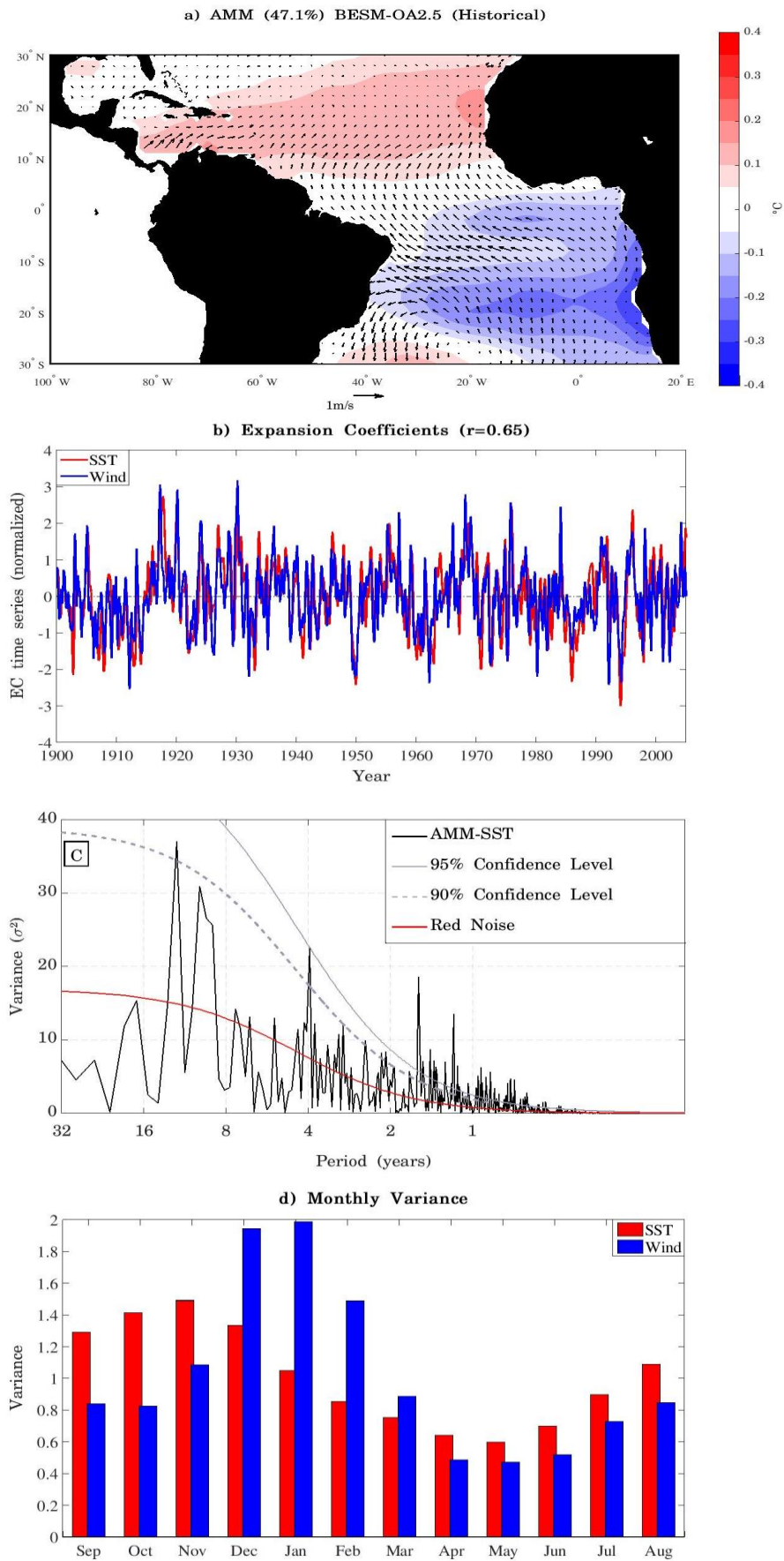
CanESM is not able to accurately simulate the AMM spatial pattern, generating a strong lobe of SSTA variability in the TSA and none significant SSTA variability in the TNA (Figure 5.2a). Nevertheless, such a strong lobe seems to generate a sufficient gradient that imposes a meridional wind speed direction despite the cross-equatorial surface wind anomalies are weak and the surface wind field anomalies in the TNA are very weak, compared with the observations. The second and the third MCA modes do not also resemble the AMM pattern, so the analysis is done using the leading pattern. The zero-lag correlation between the AMM-SST and AMM-Wind time series is 0.66, which is slightly lower than the observed and very similar to BESM-OA2.5 (Figure 5.2b); but the AMM-SST time series variability does not present a decadal periodicity (Figure 5.2c). The month-to-month variance peaks Jan-Feb-Mar for both AMM-SST and AMM-Wind, the correct season for AMM-Wind but it anticipates the AMM-SST peak by 2 months (Figure 5.2d). Figure 3.4e shows that the wind anomalies leads the SSTA by a month (Figure 5.2e), similarly to the observations. However, overall, these results show that CanESM is not able to simulate the AMM as the leading coupled mode over the tropical Atlantic.

HadGEM2-ES is able to accurately simulate the interhemispheric gradient pattern, although the southern lobe is stronger than the northern lobe, a feature that the observations do not show (Figure 5.3a). The surface wind in the equator tends to have a stronger zonal component compared with the observation and unrealistically weak surface wind speed fields over TNA and TSA are simulated by the model. The AMM-

SST and AMM-Wind time series are higher correlated at zero-lag than the observed one, with a correlation of 0.88 (Figure5.3b). The AMM temporal variability simulated by HadGEM2-ES is dominant on interannual time scales (Figure5.3c). The decadal component of the AMM variability is simulated by the mode, however, it is not significant at 90% confidence level. The model fails to reproduce the month-to-month variance of AMM-SST and AMM-Wind. The AMM-SST month-to-month variance peaks in Apr-May-Jun-Jul, whereas the AMM-Wind month-to-month variance peaks in Jun-Jul-Aug (Figure5.3d). Similarly to the observations, the lead-lag correlation shows that wind anomalies lead the SSTA by a month, with a maximum correlation of 0.90 (Figure 5.3e).

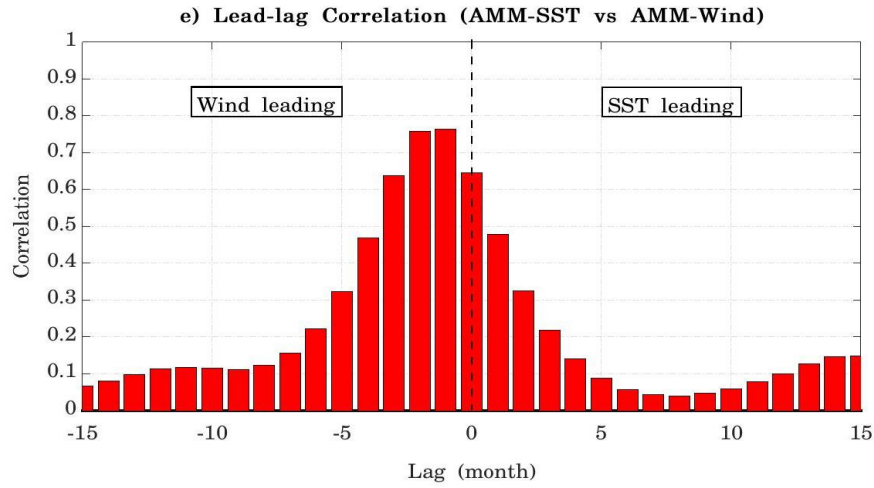
The last model evaluated is the MPI-ESM-MR. The model is capable of simulating the interhemispheric gradient pattern, with a squared covariance fraction of 40.8% which is slightly lower than the observations (Figure5.4a). The SSTA and wind anomalies associated with the coupled mode is lower than obtained through the observations. The zero-lag correlation between the AMM-SST and AMM-Wind time series is 0.74 which is very similar to the observed one (0.76) (Figure5.4b). Concerning to the temporal variability, the model shows a significant peak (at 95% confidence level) on ~8 yr periodicity, which is lower than the significant decadal peak (~11-13 yr) that occurs in the observed AMM variability (Figure5.4c). MPI-ESM-MR simulates the AMM-Wind time series month-to-month variance correctly, both the peak season and the corresponding monthly variance in each month (Figure5.4d). However, the AMM-SST month-to-month is not correctly simulated. The lead-lag correlation shows that the AMM-Wind leads the AMM-SST by a month, as in the case of the observations (Figure5.4e).

Figure 5.1 - The Atlantic Meridional Mode simulated by BESM-OA2.5.



continue

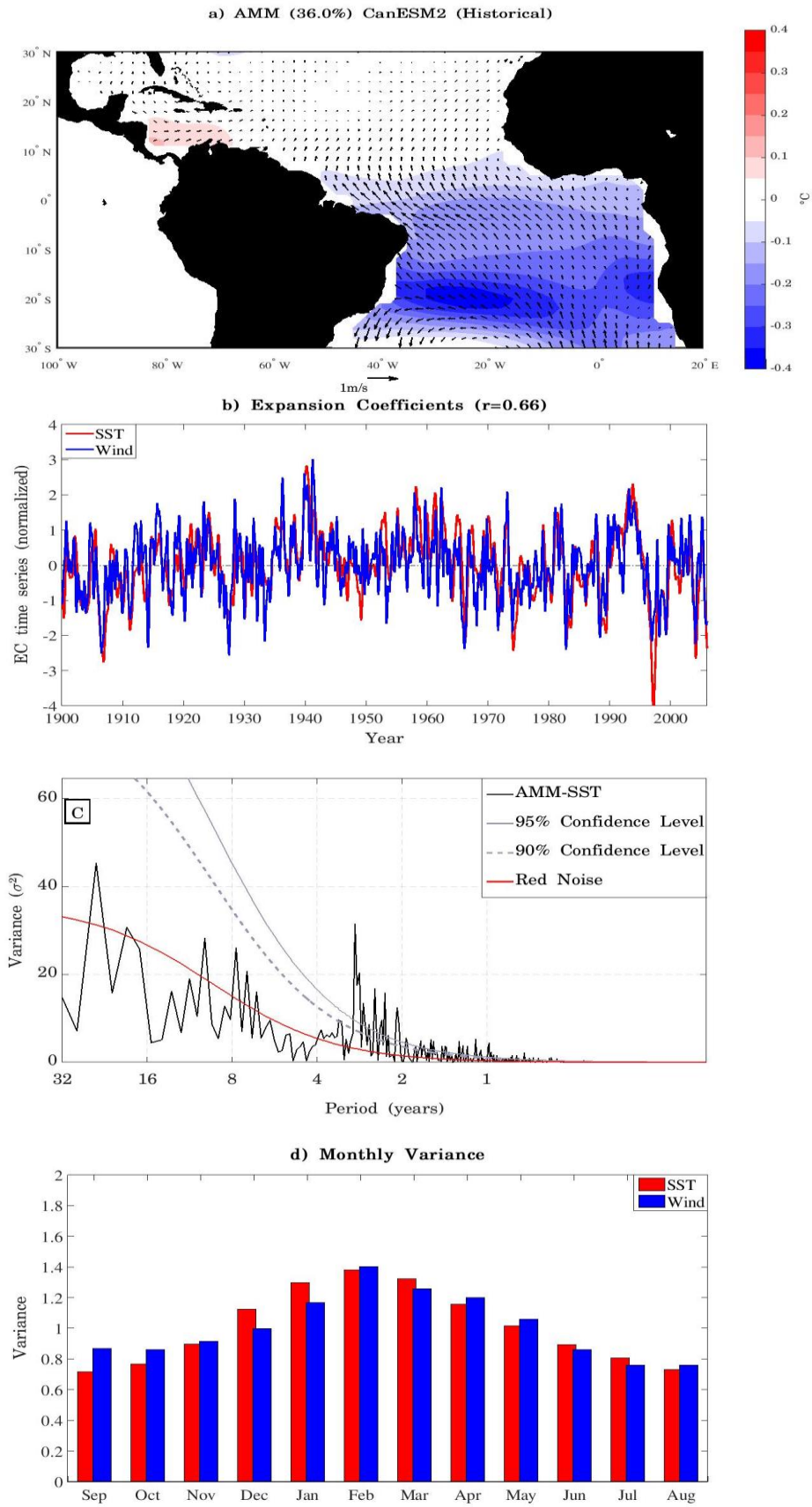
Figure 5.1 – Conclusion.



(a) The leading maximum covariance analysis (MCA) mode between SSTA (shading, °C) and 10-m wind anomalies (arrows, m s^{-1}) over tropical Atlantic (30°S – 30°N) for BESM-OA2.5 Historical simulation over the period 1900–2005. The mode is shown as the SSTA and 10-m wind anomalies regressed onto the SST normalized expansion coefficient (AMM-SST) time series ($^\circ\text{C}$ per standard deviation) for the period 1900–2005. The contour interval is 0.05°C . The squared covariance fraction of the mode is 47.1%. b) The normalized AMM-SST (red) and AMM-Wind (blue) time series. Their correlation is 0.65. c) The power spectrum of the AMM-SST time series. The solid red line represents the theoretical red noise spectrum, the dashed and solid gray lines represent the 90% and 95% confidence level, respectively. d) Month-to-month variance of the AMM-SST (red) and AMM-Wind (blue). e) The lead-lag correlation between the AMM-SST and AMM-Wind time series.

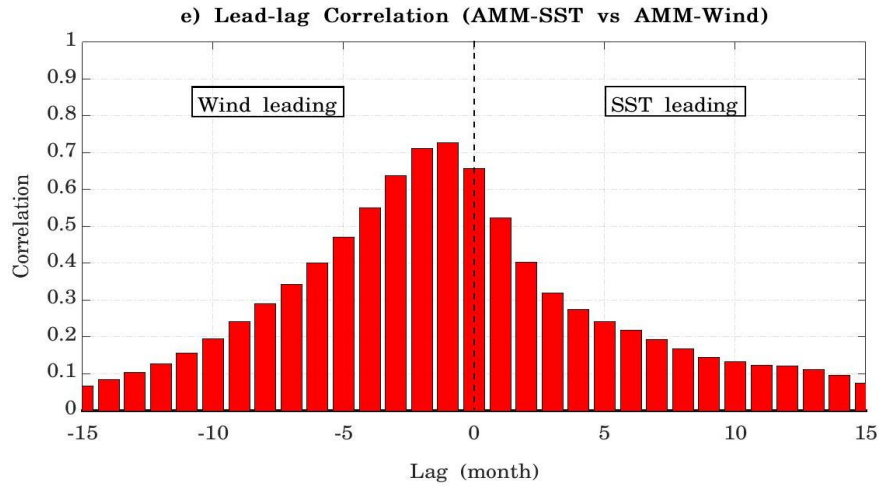
Source: by the author.

Figure 5.2 - The Atlantic Meridional Mode simulated by CanESM2.



continue

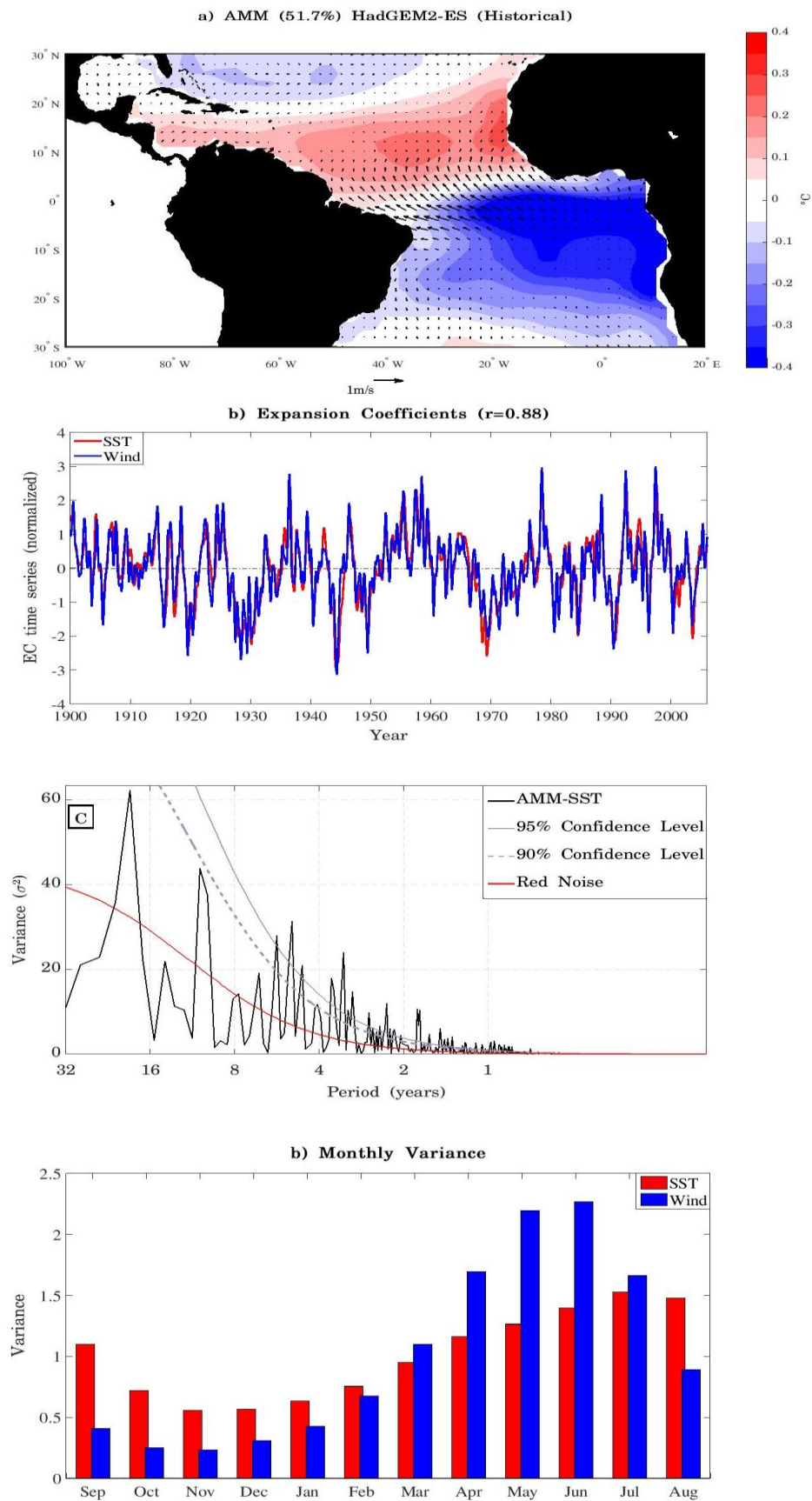
Figure 5.2 – Conclusion.



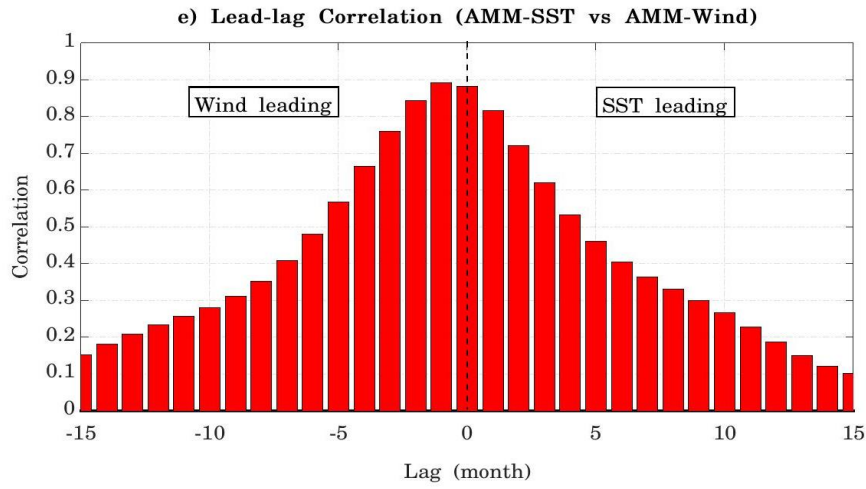
a) The leading maximum covariance analysis (MCA) mode between SSTA (shading, °C) and 10-m wind anomalies (arrows, m s^{-1}) over tropical Atlantic (30°S – 30°N) for CanESM2 Historical simulation over the period 1900–2005. The mode is shown as the SSTA and 10-m wind anomalies regressed onto the SST normalized expansion coefficient (AMM-SST) time series (°C per standard deviation) for the period 1900–2005. The contour interval is 0.05°C . The squared covariance fraction of the mode is 36.0%. b) The normalized AMM-SST (red) and AMM-Wind (blue) time series. Their correlation is 0.66. c) The power spectrum of the AMM-SST time series. The solid red line represents the theoretical red noise spectrum, the dashed and solid gray lines represent the 90% and 95% confidence level, respectively. d) Month-to-month variance of the AMM-SST (red) and AMM-Wind (blue). e) The lead-lag correlation between the AMM-SST and AMM-Wind time series.

Source: by the author.

Figure 5.3 - The Atlantic Meridional Mode simulated by HadGEM2-ES.



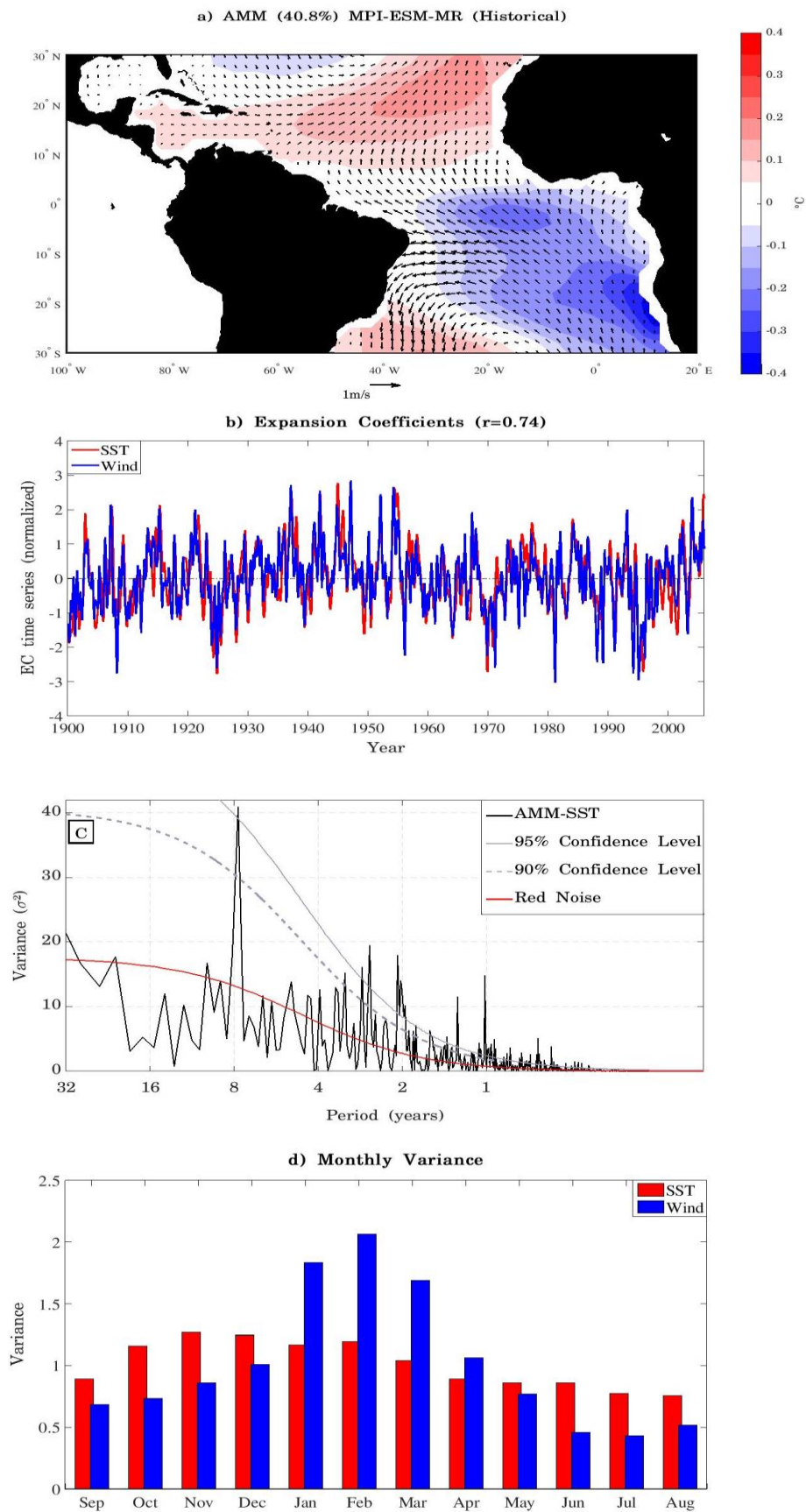
Continued Figure



(a) The leading maximum covariance analysis (MCA) mode between SSTA (shading, °C) and 10-m wind anomalies (arrows, m s^{-1}) over tropical Atlantic (30°S – 30°N) for HadGEM2-ES Historical simulation over the period 1900–2005. The mode is shown as the SSTA and 10-m wind anomalies regressed onto the SST normalized expansion coefficient (AMM-SST) time series ($^\circ\text{C}$ per standard deviation) for the period 1900–2005. The contour interval is 0.05°C . The squared covariance fraction of the mode is 51.7%. b) The normalized AMM-SST (red) and AMM-Wind (blue) time series. Their correlation is 0.88. c) The power spectrum of the AMM-SST time series. The solid red line represents the theoretical red noise spectrum, the dashed and solid gray lines represent the 90% and 95% confidence level, respectively. d) Month-to-month variance of the AMM-SST (red) and AMM-Wind (blue). e) The lead-lag correlation between the AMM-SST and AMM-Wind time series.

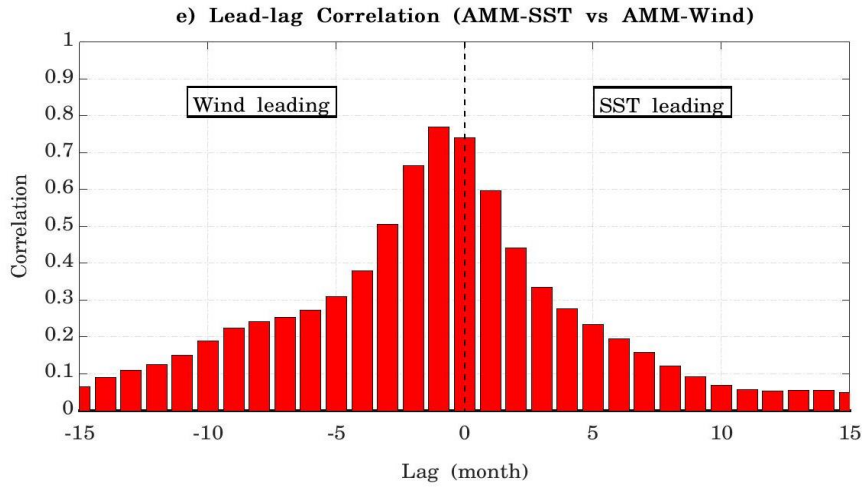
Source: by the author.

Figure 5.4 - The Atlantic Meridional Mode simulated by MPI-ESM-MR.



continue

Figure 5.4 – Conclusion.



a) The leading maximum covariance analysis (MCA) mode between SSTA (shading, °C) and 10-m wind anomalies (arrows, m s^{-1}) over tropical Atlantic (30°S – 30°N) for MPI-ESM-MR Historical simulation over the period 1900–2005. The mode is shown as the SSTA and 10-m wind anomalies regressed onto the SST normalized expansion coefficient (AMM-SST) time series ($^\circ\text{C}$ per standard deviation) for the period 1900–2005. The contour interval is 0.05°C . The squared covariance fraction of the mode is 40.8%. b) The normalized AMM-SST (red) and AMM-Wind (blue) time series. Their correlation is 0.74. c) The power spectrum of the AMM-SST time series. The solid red line represents the theoretical red noise spectrum, the dashed and solid gray lines represent the 90% and 95% confidence level, respectively. d) Month-to-month variance of the AMM-SST (red) and AMM-Wind (blue). e) The lead-lag correlation between the AMM-SST and AMM-Wind time series.

Source: by the author.

5.2 AMM Simulation Summary

Some interesting points should be highlighted. The three models that accurately simulate the interhemispheric gradient pattern (BESM-OA2.5, HadGEM2-ES and MPI-ESM-MR) tend to simulate a coupled mode that is slightly weaker than the observed mode. An important characteristic of the AMM is its dominant decadal variability. Only BESM-OA2.5 is able to reproduce the dominant decadal periodicity, although significant at 90% confidence level (observation spectral is significant at 95% confidence level). All models analyzed fail to reproduce the peak season of AMM-SST month-to-month variance. Finally, all models accurately simulate the wind anomalies leading the SSTA by a month.

Table 5.2 - Models results.

Models	AMM spatial pattern	AMM temporal pattern
BESM-OA2.5	Captures the interhemispheric pattern	<ul style="list-style-type: none"> • Captures the dominant decadal periodicity (significant at 90%) • Fails to capture the pattern seasonal phase lock • Captures the wind leading the SST
CanESM2	Fails to capture the interhemispheric pattern	Fails to capture the temporal pattern
HadGEM2-ES	Captures the interhemispheric pattern	<ul style="list-style-type: none"> • Fails to captures the dominant decadal periodicity (not significant) • Fails to capture the pattern seasonal phase lock • Captures the wind leading the SST
MPI-ESM-MR	Captures the interhemispheric pattern	<ul style="list-style-type: none"> • Fails to captures the dominant decadal periodicity (8 yr periodicity) • Fails to capture the pattern seasonal phase lock • Captures the wind leading the SST

Source: by the author.

6 INFLUENCE OF LARGE-SCALE VARIABILITY ON THE AMM DECADAL TIME SCALE

6.1 Introduction

As presented in chapter 3 (AMM review), a rich body of scientific studies contribute to the understanding of the influences of different large-scale variabilities on the Atlantic Meridional Mode (AMM). In this chapter, the hypothesis formulated based on results which shows that the Atlantic Multidecadal Oscillation (AMO) excites the AMM (chapter 1 - Motivation) is explored. Firstly, the ocean component is analyzed through the relationship of the sea surface temperature anomalies (SSTA) and the AMM on decadal time scales, and through the relationship of the variability of the ocean heat content in the upper 300 m (OHC300) in the Atlantic basin and the AMM on decadal time scales. Although several studies have explored the atmospheric variabilities which potentially influence the AMM, these relations are revisited focusing mainly on the decadal time scales. The NAO influence on AMM is particularly analyzed since there are studies which point out lack of causality (DOI; TOZUKA; YAMAGATA, 2010). Finally, a discussion based on the results from the ocean and atmospheric analysis and their interaction is presented. The analyses are based on the statistical lead-lag relationship between the variabilities through lead-lag correlation and lead-lag regression patterns.

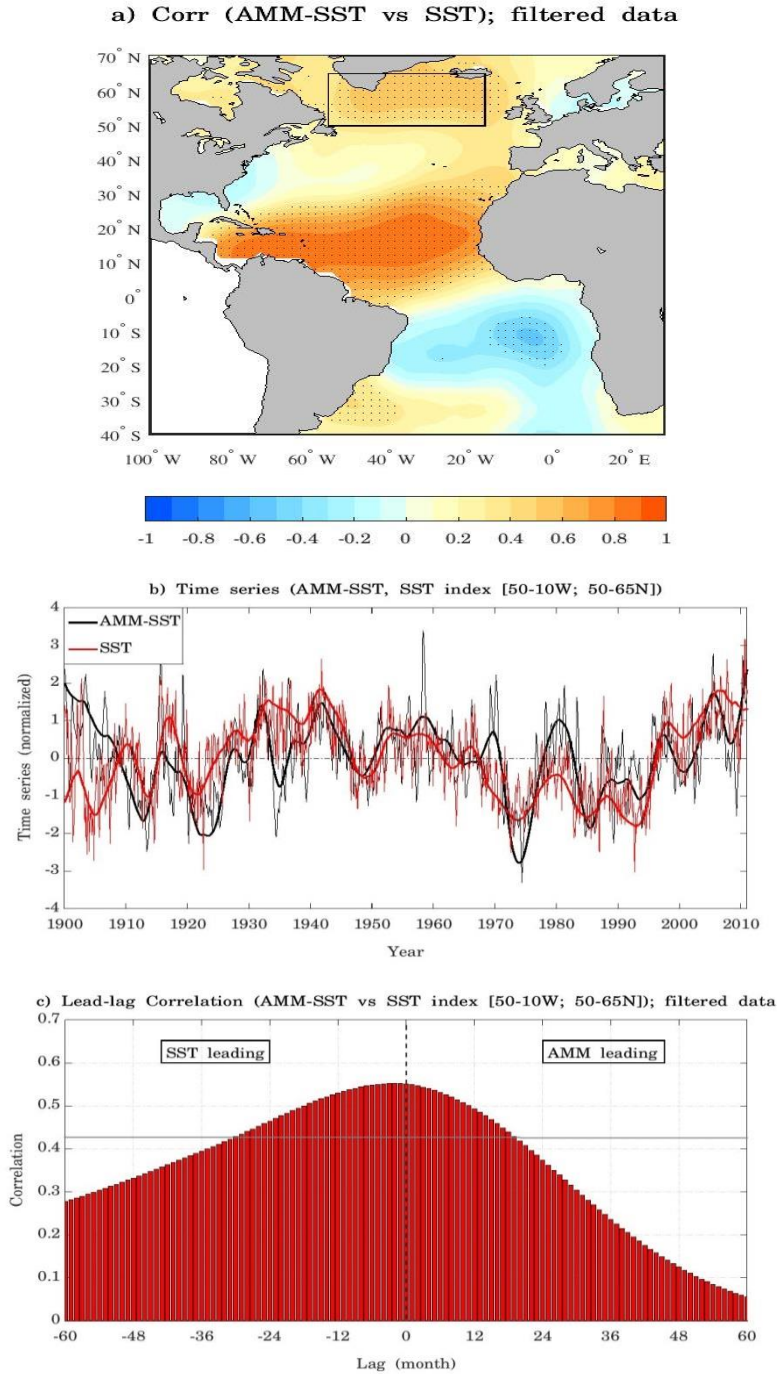
Since the interest is in understanding the relationship between the AMM and other phenomena at decadal time scale, most analyses are performed using low-pass filtered datasets. Following Zhang et al. (1997) and Vimont (2005) to leave only the low-frequency it is successively applied a 25- and 37-month running mean to the time series or at each grid point time series in the case of a field. Unless otherwise noted, the AMM-SST expansion coefficient is always used to study the AMM.

6.2 Relationship between the AMM and SST

Vimont and Kossin (2007) has found a strong correlation between AMM and the AMO, with maxima at ~ 0.84 when AMO leads AMM by a year. In their work, the AMO was computed over the region 60° – 20° W and 45° – 65° N, the region where it has greater variability (GOLDENBERG et al., 2001). AMO is characterized by a

multidecadal variability of the SSTA over the North Atlantic with periodicity at ~60–70 years cycle (SCHLESINGER; RAMANKUTTY, 1994; DELWORTH; MANN, 2000a). By performing a correlation between AMM-SST and the SSTA variability at each grid point over the Atlantic basin, it is possible to observe a significant positive spatial correlation pattern in the south of Greenland where the AMO peaks (black box, Figure 6.1a). Moreover, taking the entire Atlantic basin the pattern resembles the pan-Atlantic pattern (XIE; TANIMOTO, 1998), with significant correlation in the TNA and center of the TSA and in the western part of subtropical South Atlantic. It should be noted that the significant correlation in the TNA and TSA are expected since the AMM-SST index is taken from this region. To test the relationship between the AMM and the SSTA over the south of Greenland, an index is defined based on the spatially averaged SSTA for the region in the south of Greenland (10°–50° W; 50°–65° N; black box). Since the SSTA over the south of Greenland resembles an AMO-like variability, for simplicity we will call it AMO. The unfiltered and low-pass filtered time series of the AMM-SST and AMO are shown in Figure 6.1b. The relationship reported by Vimont and Kossin (2007) is corroborated by the lead-lag correlation between AMM-SST and AMO on decadal time scale, in which the AMO leads by 2–3 months, but with a clear persistence (Figure 6.1c). Vimont and Kossin (2007) found a maximum correlation of 0.8 for the period 1950–2005 between AMO and AMM. Here, it is only observed a maximum correlation of 0.55 for the period 1900–2010. However, it should be noted that this correlation is not stationary. The North Atlantic pattern resembles the horseshoe pattern related to the AMO.

Figure 6.1 - Relationship between AMM-SST and SST.



a) Spatial correlation pattern between the AMM-SST time series and the SSTA at each grid point. The AMM-SST and SSTA at each grid point are filtered by a low-pass filter to retain the decadal variability. Dotted areas are statistically significant at the 95% confidence level. b) AMM-SST filtered (thick black line) and unfiltered (thin black line) time series, and AMO filtered (thick red line) and unfiltered (thin red line) time series. The AMO index is computed by spatially averaged the SSTA in the south of Greenland region (black box Figure 2; 10°–50° W; 50°–65° N). All series are normalized by their respective long-term standard deviation. c) Lead-lag correlation of AMM-SST and AMO filtered time series. The gray line represents the statistically significant at the 95% confidence level value for the zero lag correlation. It should be noted that the 95% confidence level values change for each lag correlation performed. However, as the values changes are insignificant, we chose to display only the 95% confidence level value for the zero lag correlation. Datasets are provided by the 20CRv2 and ERSSTv4 reanalysis.

Source: by the author.

6.3 Relationship between the AMM and OHC300

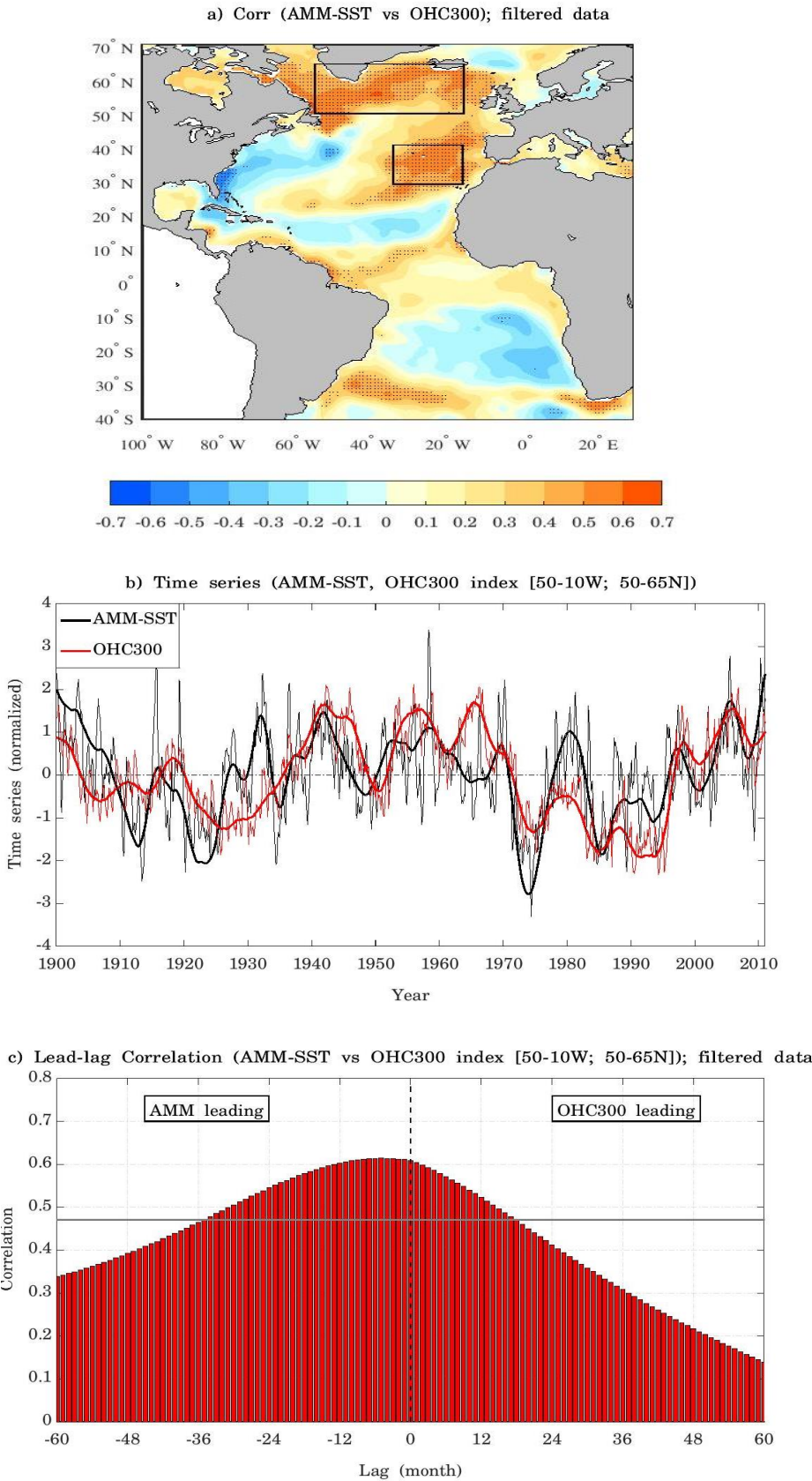
As shown in the previous section, the SSTA variability in the subpolar North Atlantic leads the AMM on decadal time scale with a strong correlation. This lead-lag relationship can be one of two scenarios: the manifestation of a mechanism triggered by the AMO that impacts the AMM variability on decadal time scale or both AMO and AMM are excited at low-frequencies by a third variability. A rich body of studies has linked the AMO to the strength of the AMOC, in which the northward transport of warm waters at the upper layers driven by the AMOC impacts the SST in the North Atlantic (DELWORTH; MANN, 2000a; KNIGHT et al., 2005). A stronger AMOC leads to warmer SST (AMO positive phase) and a weaker AMOC leads to cooler SST (AMO negative phase) in the subpolar North Atlantic. The SSTs are influenced by the ocean-atmosphere interaction at shorter time scales and by ocean large-scale circulation at longer time scales. Here, it is assumed as the hypothesis that the AMO and AMM are influenced by the same external forcing, which in this case is the AMOC. However, the analysis is interested in the decadal variability of the northward heat transport at the upper layers of the ocean driven by the AMOC over the entire Atlantic basin and not in the strength of the AMOC defined in the latitude/depth plane. The decadal ocean heat content at the upper 300 m is assumed as an indicator of the decadal variability of the northward heat transport at the upper layers. Seidov et al., (2017) shows that the decadal OHC is highly correlated decadal AMO of the entire North Atlantic. Nevertheless, the AMOC variability may impact the OHC300 differently in different North Atlantic regions (ZHANG, 2008; SEIDOV et al., 2017). Zhang (2008) shows that the AMO is positively correlated with higher ocean subsurface temperatures in subpolar regions and negatively correlated with ocean subsurface temperatures in the Gulf Stream pathway. The OHC is the integrated ocean temperature at depth and its anomalies can persist for long periods (from months to years) and potentially imprint an influence on the overlying ocean surface in the lower frequencies (FRAJKA-WILLIAMS; BEAULIEU; DUCHEZ, 2017). In this case, the OHC is computed from the ocean surface to the 300 m, using the equation:

$$OHC300(x, y) = C_p \rho \int_{-300}^0 T(x, y, z) dz \quad (J/m^2), \quad (6.1)$$

in which C_p is the sea water specific heat capacity, ρ is the sea water density and $T(x, y, z)$ is the ocean temperature profile.

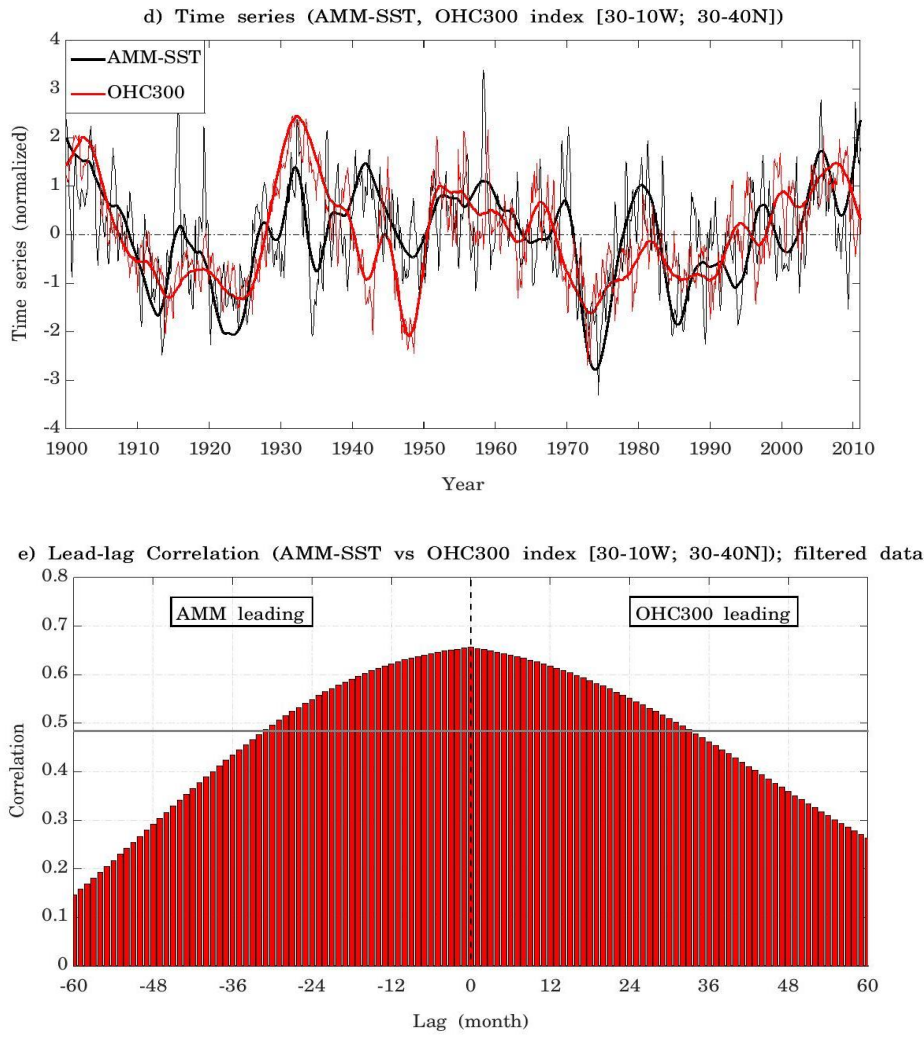
To investigate the link between the AMM and Atlantic OHC300 variability on decadal time scale, it is performed a zero lag correlation between low-pass filtered AMM-SST and OHC300 at each grid point over the Atlantic basin. The spatial correlation pattern is illustrated in Figure 6.2a. The more extensive areas which show a significant correlation between AMM-SST and the OHC300 are in the south of Greenland (50° – 60° N), extending zonally, and in the subtropical to mid-latitudes eastern Atlantic region (5° – 35° W; 30° – 45° N). In both cases, there are significant positive correlations, which indicate that the AMM positive phase is correlated with the increase of the OHC300 in these regions on decadal time scale. To further understand the nature of these correlations, two indices are defined based on the spatially averaged OHC300 for each region, in the south of Greenland (10° – 50° W; 50° – 65° N; black box) and eastern North Atlantic (10° – 30° W; 30° – 40° N; black box), which will be called as OHC300-SG and OHC300-ENA indices, respectively. The unfiltered and low-pass filtered time series of the AMM-SST with OHC300-SG and OHC300-ENA are shown in Figure 6.2b and 6.2d, respectively. The lead-lag correlation between the AMM-SST and OHC300-SG shows a slightly antisymmetric structure in which the AMM-SST leads by 5–6 months (Figure 6.2c). This result suggests that the OHC300 variability in the south of Greenland region is not exerting any influence on the AMM variability on decadal time scale. Concerning to the OHC300-ENA, the lead-lag correlation with AMM-SST shows a symmetric structure around zero lag, suggesting that the OHC300 variability in eastern North Atlantic is also not a potential AMM forcing (Figure 6.2e). The same analysis using unfiltered data show the similar results. Nonetheless, although the symmetric structure, Figure 6.2e shows that there is a higher persistence associated with the OHC300 leading. Whether there is any sort of preconditioning by the OHC300 in this region to the AMM variability, it is speculated that is communicated to the atmosphere by OHC300 influencing SSTA. (HASANEAN, 2004) shows that SSTA over tropical North Atlantic influences the sea level pressure of the subtropical high which leads to wind trade variations and can then feedback in SSTA over the same region.

Figure 6.2 - Relationship between AMM-SST and OHC300.



continue

Figure 6.2 – Conclusion.

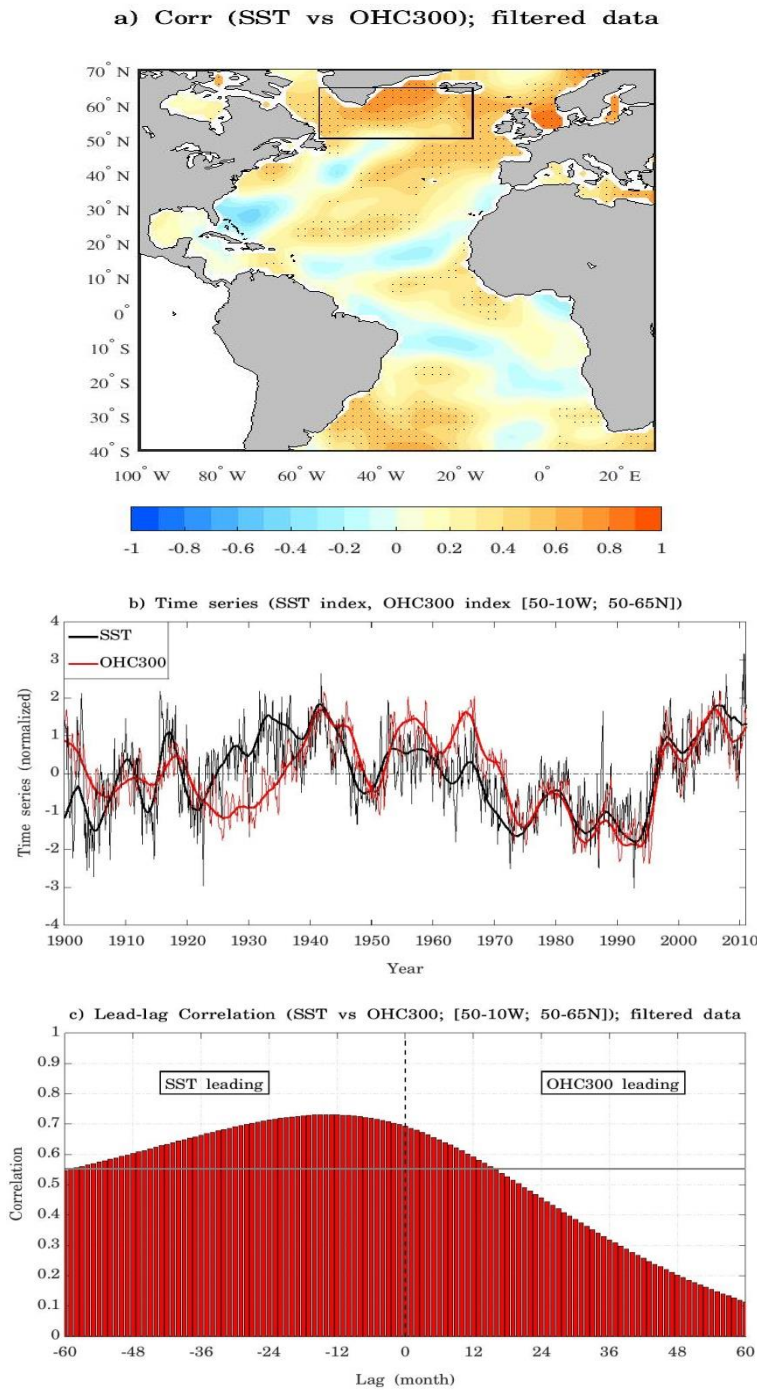


(a) Spatial correlation pattern between the AMM-SST time series and the OHC300 at each grid point. The AMM-SST and OHC300 at each grid point are filtered by a low-pass filter to retain the decadal variability. Dotted areas are statistically significant at the 95% confidence level. The black boxes represent regions where the indices OHC300-SG (south of Greenland) and OHC300-ENA (eastern North Atlantic) are computed. b) AMM-SST filtered (thick black line) and unfiltered (thin black line) time series, and OHC300-SG filtered (thick red line) and unfiltered (thin red line) time series. The OHC300-SG indices are computed by spatially averaged the OHC300 in the south of Greenland region (black box; 10°–50° W; 50°–65° N). All series are normalized by their respective long-term standard deviation. c) Lead-lag correlation of AMM-SST and OHC300-SG filtered time series. The gray line represents the statistically significant at the 95% confidence level value for the zero lag correlation. It should be noted that the 95% confidence level values change for each lag correlation performed. However, as the values change are insignificant, we chose to display only the 95% confidence level value for the zero lag correlation. d) AMM-SST filtered (thick black line) and unfiltered (thin black line) time series, and OHC300-ENA filtered (thick red line) and unfiltered (thin red line) time series. The OHC300-ENA indices are computed by spatially averaged the OHC300 in the eastern North Atlantic region (black box; 10°–30° W; 30°–40° N). All series are normalized by their respective long-term standard deviation. e) Lead-lag correlation of AMM-SST and OHC300-ENA filtered time series. The gray line represents the statistically significant at the 95% confidence level value for the zero lag correlation. It should be noted that the 95% confidence level values change for each lag correlation performed. However, as the values change are insignificant, we chose to display only the 95% confidence level value for the zero lag correlation. Datasets are provided by the 20CRv2, ERSSTv4 and CHOR_RL reanalysis.

Source: by the author.

To test this assumption, it is performed a zero lag correlation between the OHC300 and the SSTA at each grid point over the Atlantic basin (Figure6.3a). For this analysis, the OHC300 dataset is interpolated into the SST grid point resolution. The OHC300 over the region defined in the eastern North Atlantic region is weakly and not significantly correlated to SSTA. This result suggests that the AMM decadal variability is not influenced by the decadal variability of the OHC300 in the Atlantic basin, by potentially imprint a long-term persistent SST anomalies that can then affect atmospheric circulation in that region. The OHC300 is strongly correlated to the SSTA in the North Atlantic and subpolar eastern North Atlantic. There is also a large area of significant correlations in the western mid-latitudes of the South Atlantic. By using the same south of Greenland index region it is computed a time series for the SSTA (AMO). The unfiltered and low-pass filtered time series of the AMO and OHC300-SG are shown in Figure6.3b. It is performed the lead-lag correlation between the AMO and OHC300-SG on decadal time scale (Figure6.3c). The SSTA leads the OHC300 roughly by 12–15 months. A similar result is reported by Hazeleger et al., (2013, Figure9a). This result indicates that subsurface ocean processes influencing the surface are unlikely. Therefore, in this case, the influence seems to be generated from atmospheric processes. Since the NAO can potentially impact the SST over North Atlantic, recent works have shown the influence of the stratospheric quasi-biennial oscillation (QBO) on the NAO through the stratospheric polar vortex strength (DUNSTONE et al., 2016; GRAY et al., 2018).

Figure 6.3 - Relationship between SST and OHC300.



a) Spatial correlation pattern between the SSTA and the OHC300 in each grid point. The OHC300 datasets is interpolated into the SST resolution grid point. The data at each grid point are filtered by a low-pass filter to retain the decadal variability. Dotted areas are statistically significant at the 95% confidence level. b) SSTA-SG filtered (thick black line) and unfiltered (thin black line) time series, and OHC300-SG filtered (thick red line) and unfiltered (thin red line) time series. Both indices are computed by being spatially averaged in the south of Greenland region (black box of Figure 2; 10°–50° W; 50°–65° N). All series are normalized by their respective long-term standard deviation. c) Lead-lag correlation of SSTA-SG and OHC300-SG filtered time series. The gray line represents the statistically significant at the 95% confidence level value for the zero lag correlation. It should be noted that the 95% confidence level values change for each lag correlation performed. However, as the values change are insignificant, we chose to display only the 95% confidence level value for the zero lag correlation. Datasets are provided by the ERSSTv4 and CHOR_RL reanalysis.

Source: by the author.

To investigate the hypothesis whether there is a link between the ocean subsurface variability manifested in the variability of the OHC300 and the dominant decadal variability of the AMM was one of the purposes of the present thesis. Through the results obtained from lead-lag analysis, it is possible to conclude that there is no relationship between the OHC300 and AMM variabilities, at least in terms of causation. Therefore, the OHC300 variability over the North Atlantic does not trigger any kind of mechanism that may impact the AMM on decadal time scale.

6.4 Revisiting the NAO and ENSO influence on the AMM

Numerous studies have shown the impact of ENSO and NAO on the subtropical Atlantic SST, in particular in the TNA SSTA that can potentially lead the AMM formation (ENFIELD; MAYER, 1997; CZAJA; VAN DER VAART; MARSHALL, 2002; AMAYA; FOLTZ, 2014). Nevertheless, as mentioned in chapter 2, the forcing exerted by the NAO still raises debate (RUIZ-BARRADAS; CARTON; NIGAM, 2000; WAINER; SERVAIN; CLAUZET, 2008; DOI; TOZUKA; YAMAGATA, 2010).

The NAO variability is considered slightly red with no significant power spectra at any particular frequency (HURRELL; LOON, 1997; MARSHALL; JOHNSON; GOODMAN, 2001; WANG et al., 2017), despite an interannual periodicity at ~ 2 and ~ 8 years cycle (MARSHALL; JOHNSON; GOODMAN, 2001; WANNER et al., 2001; HURRELL; DESER, 2010) and multidecadal variability with spectra energy at ~ 50 – 70 years (COOK; DARRIGO; BRIFFA, 1998; OLSEN; ANDERSON; KNUDSEN, 2012; SUN; LI; JIN, 2015). Although the complexity of the NAO time scale variability, some studies have suggested the NAO as an important external forcing on the AMM, in particular on decadal time scale (WU; LIU, 2002; CHIANG; VIMONT, 2004; WU; ZHANG; LIU, 2004; HUANG; SHUKLA, 2005). Chang et al., (2006c) suggest that NAO imposes an influence in the AMM based on red noise process and AMM decadal time scale occurs by chance; such hypothesis can be regarded as a null hypothesis for AMM decadal variability. However, its influence on AMM is not clear yet, with studies using different approaches finding no clear print of the NAO forcing AMM (RUIZ-BARRADAS; CARTON; NIGAM, 2000; DOI; TOZUKA; YAMAGATA, 2010), or finding the reverse, AMM forces the NAO on

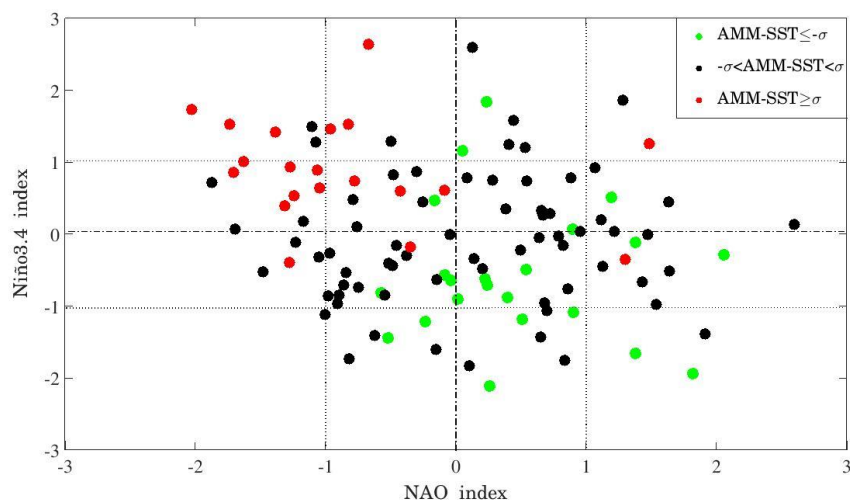
decadal time scale (WAINER; SERVAIN; CLAUZET, 2008). ENSO is characterized by a well defined interannual periodicity (~2–7 years cycle) and, opposing to NAO, is well accepted as external forcing that mainly modulates the AMM on interannual time scales (RUIZ-BARRADAS; CARTON; NIGAM, 2000; CZAJA; VAN DER VAART; MARSHALL, 2002; LIU; ZHANG; WU, 2004; WU; ZHANG; LIU, 2004).

The NAO and ENSO-like indices are computed in order to further understand the relationship between them and AMM. The NAO index is obtained from the first principal component (PC) which results of applying the empirical orthogonal function (EOF) to the monthly mean sea level pressure (MSLP) monthly anomalies over the North Atlantic region, similar to Figure 4.5 but here is used monthly data. Such a methodology allows having a representation of the NAO that is not fixed spatially, different from the widely used station-based Hurrell's NAO index. Nonetheless, for the monthly data, the two time series have a high correlation of 0.82. The ENSO variability is assessed through the Niño3.4 index which captures the SST variability in the East Central Tropical Pacific by spatially averaged the SSTA over the region 5° N–5° S and 170°–120° W.

Figure 6.4 shows a scatter plot constructed using unfiltered normalized Niño3.4, NAO and AMM indices, in which is highlighted the strong negative AMM events (i.e. $AMM \leq -\sigma$) and strong positive AMM events (i.e. $AMM \geq \sigma$). The NAO and Niño3.4 normalized indices are the coordinates. Over the period 1900–2010, we have 20 strong AMM positive events and 22 strong AMM negative events. It is used NAO and Niño3.4 indices averaged for the trimesters DJF and FMA, respectively; preceding the AMM boreal spring peak phase. The results show that negative NAO index ($< 0\sigma$) corresponds to 18 of 20 strong positive AMM events ($\geq \sigma$), whereas positive NAO index ($> 0\sigma$) corresponds to 16 of 22 strong negative AMM events ($\leq -\sigma$). Therefore, negative NAO index precedes strong positive AMM events in 90% of the cases and positive NAO index precedes strong negative AMM events in 73% of the cases. Concerning the Niño3.4 index, negative Niño3.4 index ($< 0\sigma$) corresponds to 17 of 22 strong negative AMM events, whereas positive Niño3.4 index ($> 0\sigma$) corresponds to 17 of 20 strong positive AMM events (17/20). Therefore, negative Niño3.4 index precedes strong negative AMM events in 77% of the cases and positive Niño3.4 index precedes strong positive AMM events in 81% of the cases. Considering the

combination of the NAO and Niño3.4 indices, negative NAO index ($< 0\sigma$) and positive Niño3.4 index ($> 0\sigma$) corresponds to 16 of 20 strong positive AMM events, representing 16 of 18 events that occurred for particular case of negative NAO, i.e. 89% of strong positive AMM events preceded by negative NAO phase. Positive NAO index ($> 0\sigma$) and negative Niño3.4 index ($< 0\sigma$) corresponds to 12 of 22 strong negative AMM events, representing 12 of 16 events that occurred in the particular case of positive NAO index, i.e. 75% of strong negative AMM events preceded by positive NAO phase. These results suggest that negative NAO conditions and/or El Niño events (events that warm the TNA region) are more efficient in leading to a positive AMM phase formation than positive NAO conditions and/or La Niña events leading to a negative AMM phase formation. El Niño (La Niña) conditions tend to generate anomalous southwesterlies (northeasterlies) in the TNA, that associated with negative (positive) NAO that reduce (enhance) the climatological trade winds, reinforce anomalous ocean surface latent heat flux over the subtropical North Atlantic, causing the warm (cool) of the ocean mixed layer; conditions that can trigger a positive (negative) AMM phase formation. It should be noted that the NAO conditions can be a response to the Pacific conditions, although they have a weak relationship (GERSHUNOV; BARNETT, 1998). A summary of these relations is presented in Table 6.1.

Figure 6.4 - Scatter plot using as coordinates normalized NAO and Niño3.4 indices averaged for the trimesters FMA and DJF, respectively.



The AMM phases are normalized averages from boreal spring season (MAM), in which blue, red and black dots represent $AMM \leq -\sigma$, $AMM \geq \sigma$ and $-\sigma > AMM > -\sigma$, respectively. To compute the indices respective unfiltered datasets are used. NAO and Niño3.4 indices are computed using datasets from 20CRv2 and ERSSTv4 reanalysis, respectively
Source: by the author.

Table 6.1 - Summarized relation between NAO index, Niño3.4 index and the phases of the AMM-SST based on the scatter plot of Figure 6.4, for the period 1900-2010.

	AMM $\leq -\sigma$	AMM $\geq \sigma$
NAO $< 0\sigma$	6/22 (27%)	18/20 (90%)
NAO $> 0\sigma$	16/22 (73%)	2/20 (10%)
Niño3.4 $< 0\sigma$	17/22 (77%)	3/20 (15%)
Niño3.4 $> 0\sigma$	5/22 (23%)	17/20 (85%)
NAO $< 0\sigma$ and Niño3.4 $> 0\sigma$	1/22 (1/6)	16/20 (16/18; 89%)
NAO $> 0\sigma$ and Niño3.4 $< 0\sigma$	12/22 (12/16; 75%)	1/20 (1/2)

The information in the lines 2, 3, 4 and 5, consists of the number of strong negative AMM events (column 2) and strong positive AMM events (column 3) events that occurred under different phases of NAO and El Niño, over the total number of AMM negative events (column 2) and AMM positive events (column 3). In parentheses are the proportions. For the lines 6 and 7, the information consists of the number of strong negative AMM events (column 2) and strong positive AMM events (column 3) that occurred following NAO negative phase and El Niño conditions (line 6) and following NAO positive phase and La Niña conditions (line 7), over the total number of AMM negative events (column 2) and AMM positive events (column 3). In parentheses is the same but over the number of strong AMM events that occurred following that phase of NAO.

Source: by the author.

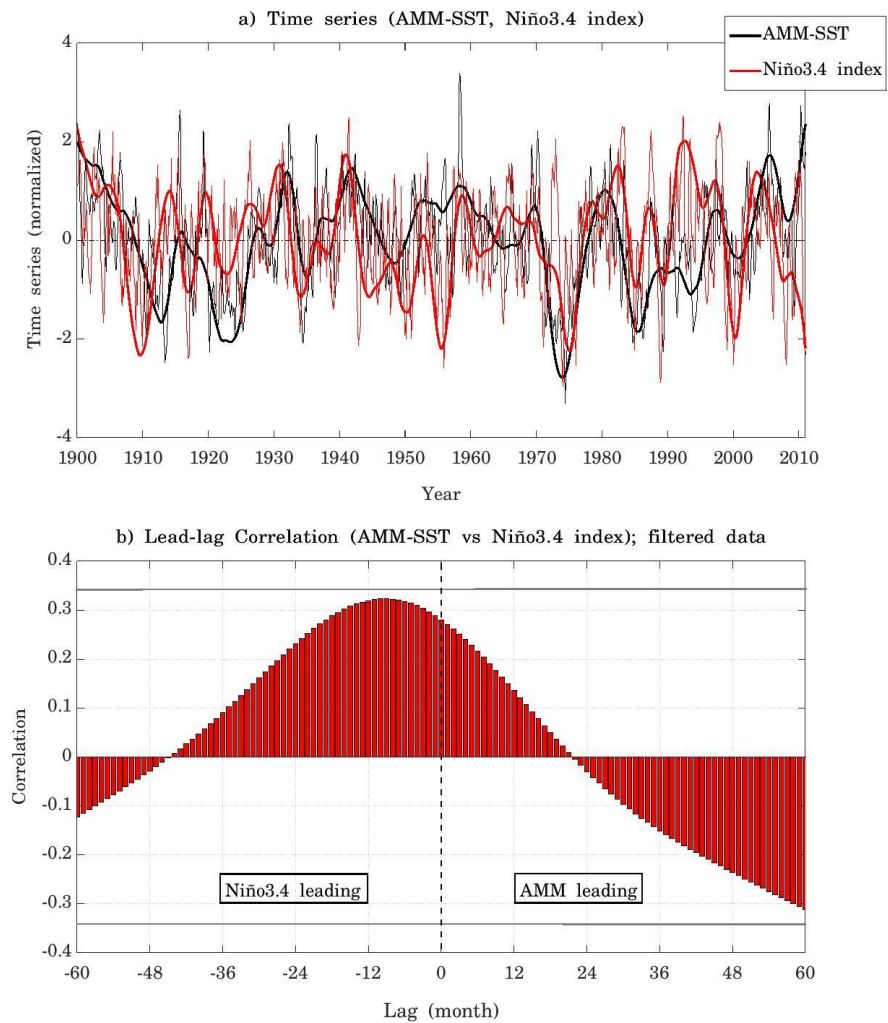
This statistical relationship corroborates the conclusions that the AMM is influenced by the ENSO and NAO variability that a great number of studies have already suggested on the interannual time scale (NOBRE; SHUKLA, 1996; CHIANG; VIMONT, 2004; XIE; CARTON, 2004). To test its relationship with the AMM variability on the decadal time scale, lead-lag correlation are performed between the low-pass filtered of Niño3.4 and AMM indices, and between the low-pass filtered of NAO and AMM indices. Figure 6.5a shows the respective unfiltered and filtered Niño3.4 and AMM time series, and Figure 6.5b the lead-lag correlation between the filtered time series. The relationship between the two modes is not significant on decadal time scales. Nonetheless, changes in the strength of decadal ENSO and its global teleconnections have statistical relation with Interdecadal Pacific Oscillation (IPO) (WANG et al., 2014), a Pacific-wide decadal to multidecadal SSTA variability (POWER et al., 1999; FOLLAND, 2002). Such a decadal to multidecadal variability may influence the AMM on the decadal time scale. To characterize the IPO variability

the Tripole Index (TPI) is used (HENLEY et al., 2015). The TPI is computed using the following formula:

$$TPI = SSTA_2 - \frac{SSTA_1 + SSTA_3}{2}. \quad (6.2)$$

Here, the $SSTA_1$, $SSTA_2$ and $SSTA_3$ represent spatially averaged SST anomalies over the North Pacific region (25° N – 45° N , 140° E – 145° W), the central Pacific region (10° S – 10° N , 170° E – 90° W) and southwestern Pacific region (50° S – 15° S , 150° E – 160° W), respectively. The unfiltered and low-pass filtered time series of the IPO and AMM are shown in Figure 6.6a. The lead-lag correlation between the low-pass filtered time series indicates the lack of a significant link between the IPO and AMM at lower periodicities (Figure 6.6b). The lack of a statistical relationship between either ENSO or IPO and the AMM on decadal time scale leads to the conclusion that the lower periodicity of AMM may be generated within the Atlantic.

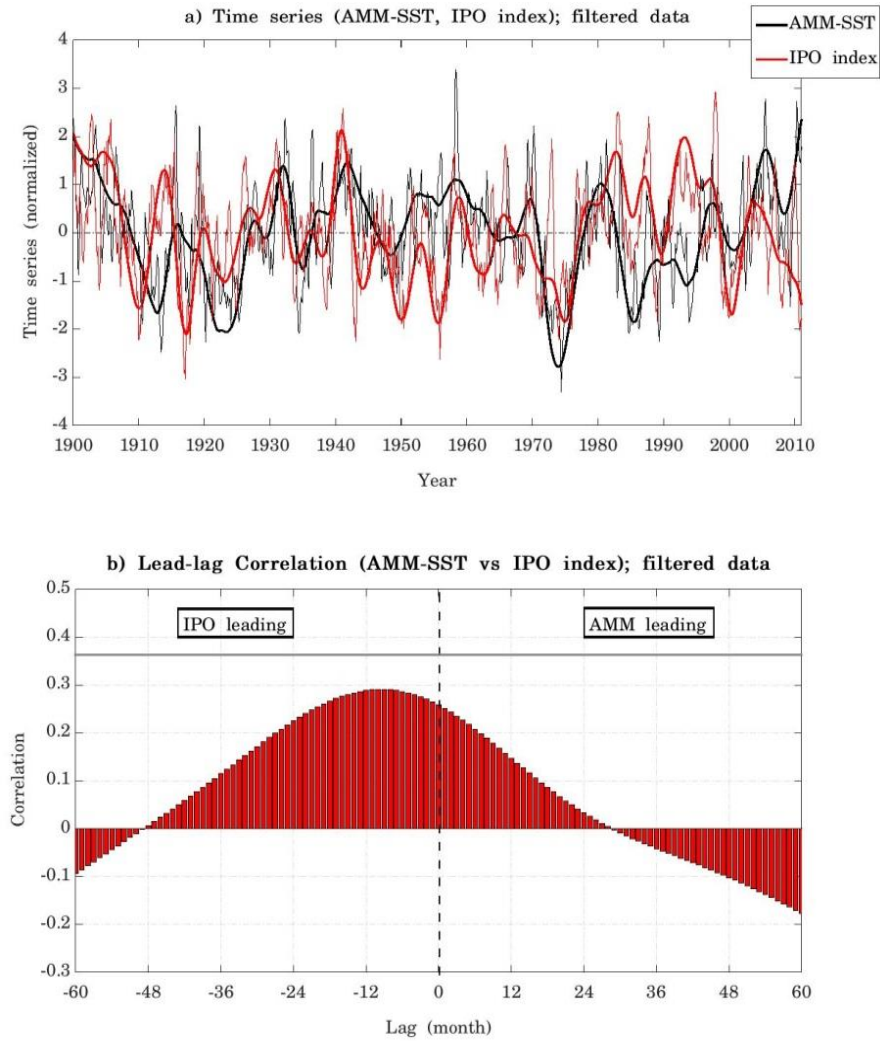
Figure 6.5 - Relationship between AMM-SST and Niño3.4.



a) AMM-SST filtered (thick black line) and unfiltered (thin black line) time series, and Niño3.4 index filtered (thick red line) and unfiltered (thin red line) time series. All series are normalized by their respective long-term standard deviation. b) Lead-lag correlation of AMM-SST and Niño3.4 index filtered time series. The gray line represents the statistically significant at the 95% confidence level value for the zero lag correlation. It should be noted that the 95% confidence level values change for each lag correlation performed. However, as the values change are insignificant, we chose to display only the 95% confidence level value for the zero lag correlation. Datasets are provided by the 20CRv2 and ERSSTv4 reanalysis.

Source: by the author.

Figure 6.6 - Relationship between AMM-SST and IPO.



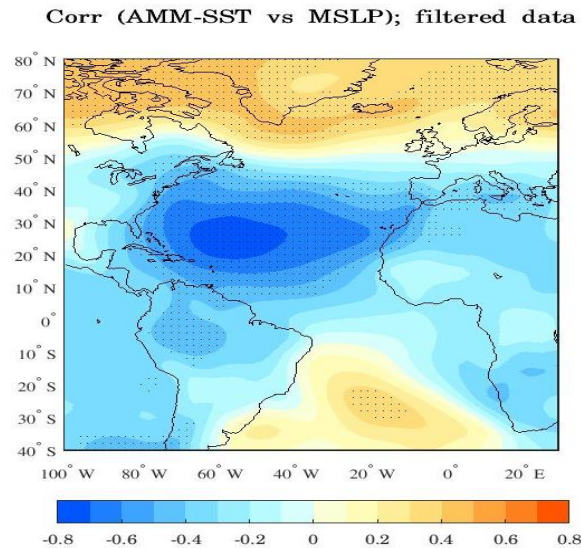
a) AMM-SST filtered (thick black line) and unfiltered (thin black line) time series, and IPO index filtered (thick red line) and unfiltered (thin red line) time series. All series are normalized by their respective long-term standard deviation. b) Lead-lag correlation of AMM-SST and IPO index filtered time series. The gray line represents the statistically significant at the 95% confidence level value for the zero lag correlation. It should be noted that the 95% confidence level values change for each lag correlation performed. However, as the values change are insignificant, we chose to display only the 95% confidence level value for the zero lag correlation. Datasets are provided by the 20CRv2 and ERSSTv4 reanalysis.

Source: by the author.

Following the same kind of analysis carried out for SSTA and OHC300, it is here performed a zero lag correlation between low-pass filtered AMM-SST and MSLP at each grid point over the Atlantic basin (Figure 6.7). At decadal time scales, the relationship is evident since a significant spatial correlation pattern clearly resembles the NAO-like pattern over the North Atlantic. Positive (negative) AMM is strongly correlated with negative (positive) anomalies in the southern (northern) lobe of the

NAO at decadal time scales, meaning that negative (positive) NAO is related to positive (negative) AMM phase. The spatial pattern shows a relation with the subtropical South Atlantic pressure system (South Atlantic Anticyclone), although weaker compared with NAO variability (MÉLICE; SERVAIN, 2003). A stronger South Atlantic Anticyclone is positively correlated with a positive AMM phase, by the same sort of mechanism exerted by NAO in the boreal hemisphere (BARREIRO et al., 2004). The southward displacement of the southern lobe MSLP anomalies is likely to be related to the zero lag relation also manifesting the influence of the AMM SST pattern on the MSLP.

Figure 6.7 - Relationship between AMM-SST and MSLP.



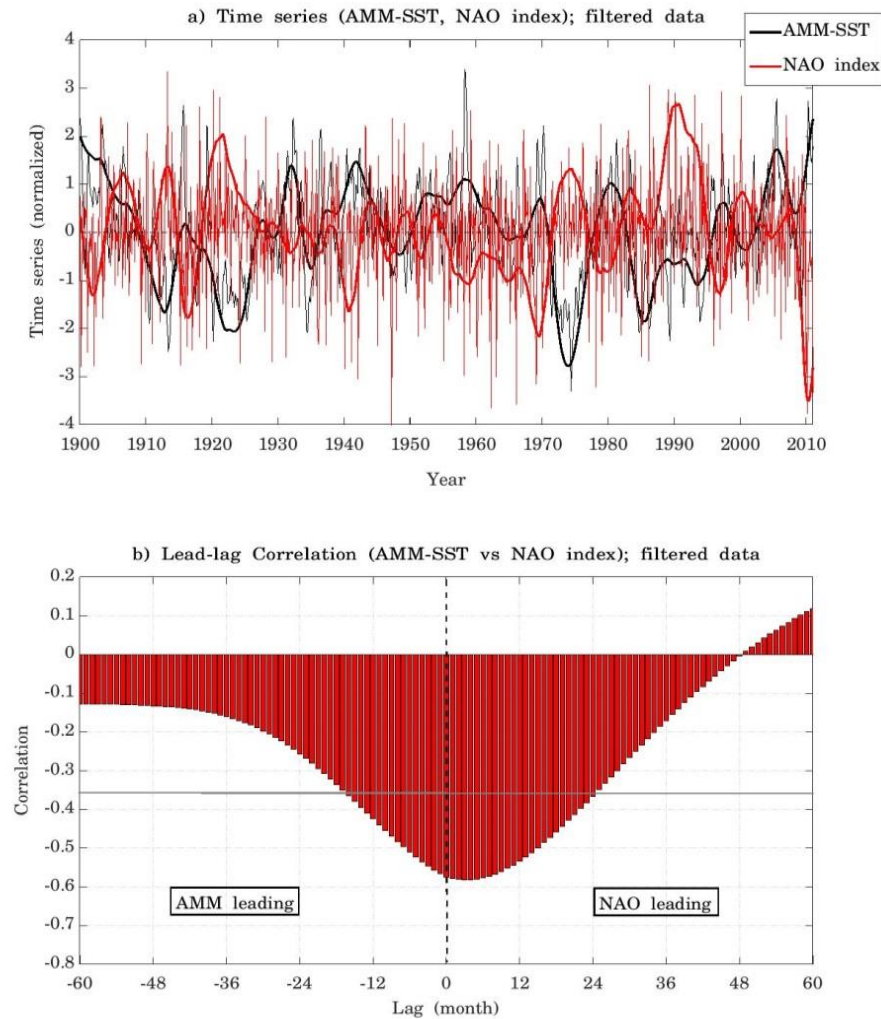
Spatial correlation pattern between the AMM-SST time series and the MSLP anomalies at each grid point. The AMM-SST and MSLP anomalies at each grid point are filtered by a low-pass filter to retain the decadal variability. Dotted areas are statistically significant at the 95% confidence level. Datasets are provided by the 20CRv2 and ERSSTv4 reanalysis.

Source: by the author.

The unfiltered and low-pass filtered time series of the NAO index and AMM-SST are shown in Figure 6.8a. The low-pass filtered time series lead-lag correlation shows an antisymmetric structure with higher persistence for NAO leading, with the maximum link occurring at lag 2–4 months with significant correlation of -0.58 (Figure 6.8b). These results indicate that the NAO phases are significantly correlated to the AMM formation and its phases on decadal time scale, in which the higher correlation occurs when NAO precedes. Therefore, the mechanism based on the impact of negative

(positive) NAO that reduce (enhance) the climatological trade winds, driving anomalous ocean surface latent heat flux over the subtropical North Atlantic, which warms (cools) of the ocean mixed layer, is likely to be an efficient way of inducing a positive (negative) AMM on decadal time scale.

Figure 6.8 - Relationship between AMM-SST and NAO.



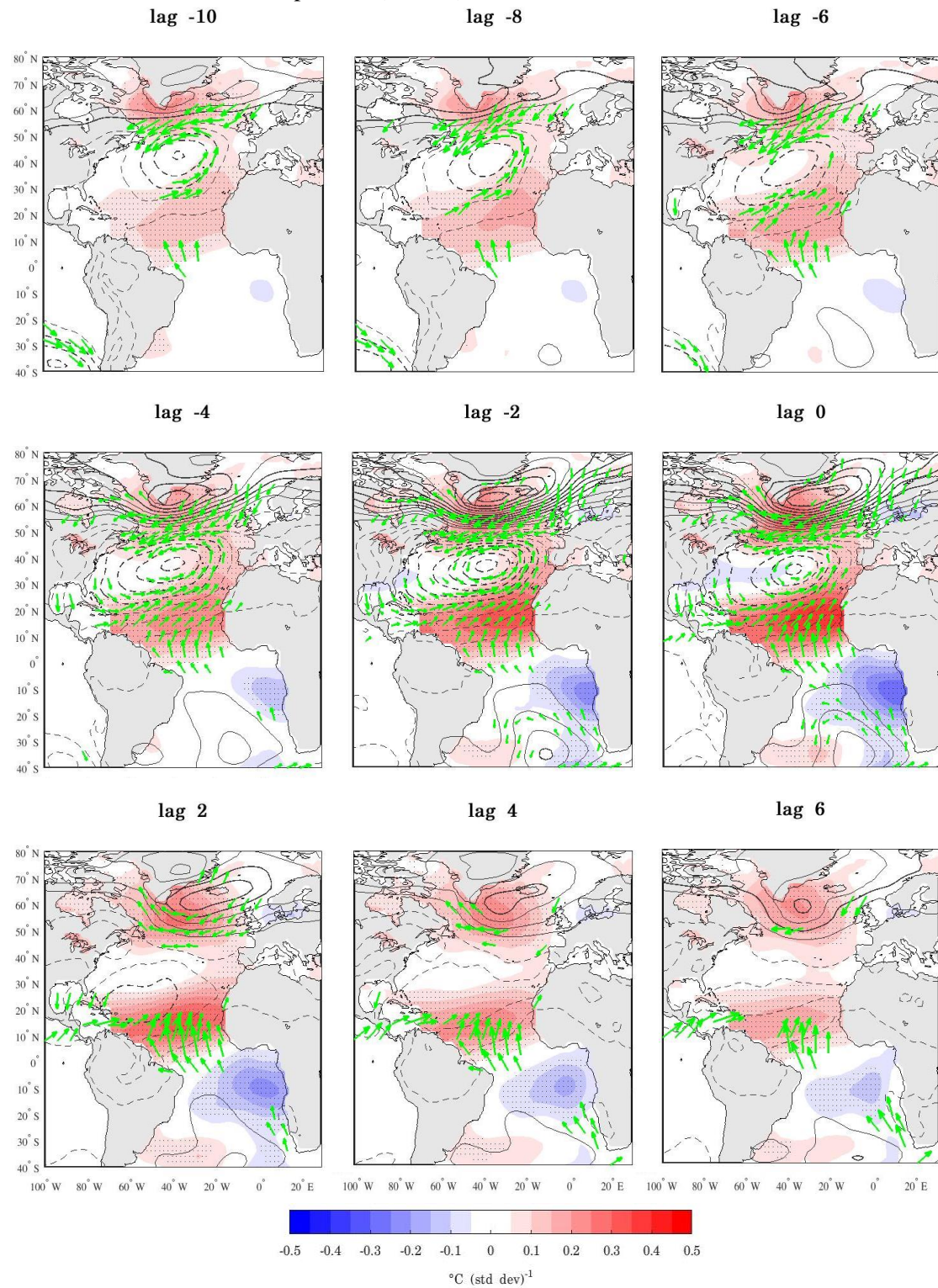
a) AMM-SST filtered (thick black line) and unfiltered (thin black line) time series, and NAO index filtered (thick red line) and unfiltered (thin red line) time series. All series are normalized by their respective long-term standard deviation. b) Lead-lag correlation of AMM-SST and NAO index filtered time series. The gray line represents the statistically significant at the 95% confidence level value for the zero lag correlation. It should be noted that the 95% confidence level values change for each lag correlation performed. However, as the values change are insignificant, we chose to display only the 95% confidence level value for the zero lag correlation. Datasets are provided by the 20CRv2 and ERSSTv4 reanalysis.

Source: by the author.

6.5 On the interpretation of NAO and AMO influences

Through the results obtained in the previous subsections, it is possible to conclude that the AMM on decadal time scale has a strong relationship with the AMO and the NAO variabilities. To further reinforce these conclusions and understand the nature of these links, spatial patterns of lead-lag regression are carried out by regressing the anomalies of SST, MSLP and 10-m wind components onto the normalized unfiltered AMM-SST index (Figure 6.9). Here, positive lags mean that AMM is leading the respective climatological variable patterns. At lag -10 months is noticed that positive anomalies of SST in TNA and in the south of Greenland are present since negative anomalies of the Azores High (weaker high pressure center) is also formed but the Iceland Low has not a significant structure. A full NAO pattern (in this case, in its negative phase) is established at lag -4 and reinforced at lag -2. At the AMM peak (lag 0), we have a similar NAO pattern of lag -2, and the SST anomalies are at their peak, with full coupled SST/10-m wind components. In the positive lags, i.e. AMM leading, the NAO pattern starts to weaken and quickly vanishes from lag 2 to lag 6, particularly the Azores High. It is not possible to infer causality through this lead-lag relationship, but it reinforces the likelihood of the NAO as an important variability in exciting the AMM, corroborating previous studies that reached this conclusion (XIE; TANIMOTO, 1998; CHIANG; VIMONT, 2004; HUANG; SHUKLA, 2005). Generally, previous works used observed data for the second half of the 20th century (XIE; TANIMOTO, 1998; CHIANG; VIMONT, 2004), whereas here it is used observed data for the whole 20th century and the datasets are provided by different reanalysis.

Figure 6.9 - Lead-lag regression maps of SST (shaded 0.05 °C), MSLP (contour 0.2 hPa) and 10-m wind components (vectors) onto unfiltered AMM-SST index.



For the SST, dotted areas are statistically significant at the 95% confidence level. For MSLP, solid contours denote positive values, dashed contours denote negative values, and the zero contours have been omitted. For 10-m wind components, only values greater than 0.15 m s^{-1} are plotted. Since the regression slope coefficients are obtained with the normalized AMM index, the values of each field represent variations per standard deviation of the AMM index. Positive lags indicate that AMM index is leading. Datasets are provided by the 20CRv2 and ERSSTv4 reanalysis.

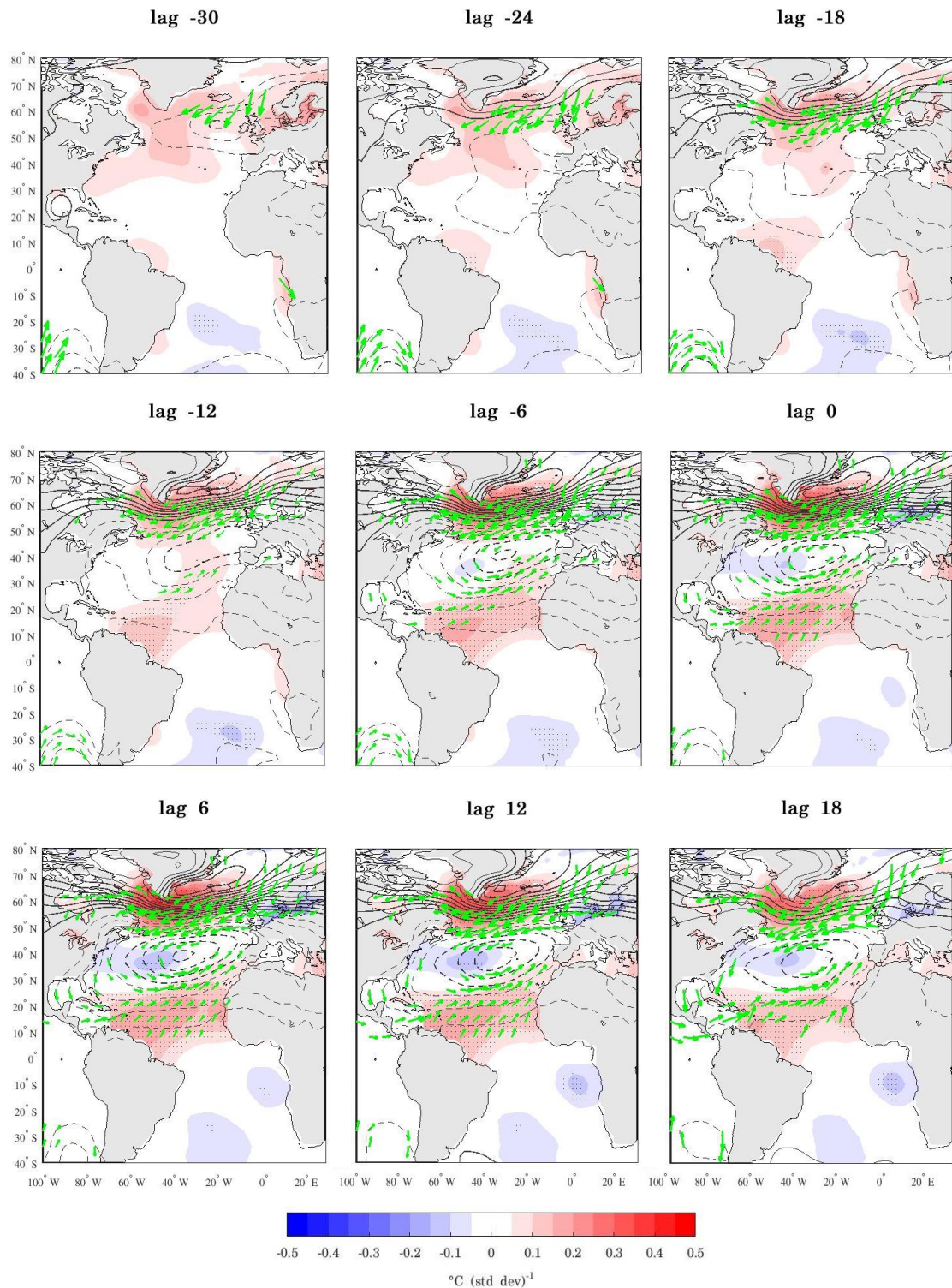
Source: by the author.

The lead-lag regression map of the MSLP reveals the NAO pattern, in which the lowering (enhancing) of the Azores high (the NAO southern lobe) and the lowering (enhancing) of the Iceland low (the NAO northern lobe), which means a decrease (increase) in the NAO index implies the formation of the AMM pattern in its positive (negative) phase with a lag of ~ 2 months. The regression of the 10-m wind components reveals an anomalous southwesterly (northeasterly) in the subtropical North Atlantic, coherent with the NAO pattern wind response. Variation of the trade wind in the equatorward side of the Azores high influence the sea surface latent heat flux which leads to SST anomalies that subsequently can trigger the WES feedback process and lead to AMM is likely to be the most important mechanism in triggering the AMM (CZAJA; VAN DER VAART; MARSHALL, 2002; HANDOH et al., 2006; PENLAND; HARTTEN, 2014). The relationship between AMM and NAO is also highlighted by Chiang and Vimont (2004, Figure 10), suggesting that trade winds anomalies in the subtropical North Atlantic that is related to the AMM variability originate from NAO variability. Their analysis use composites method to infer the AMM seasonal evolution. Here, by using the lead-lag regression method it is possible to clearly infer that NAO precedes the AMM formation, reinforcing their conclusion.

Figure 6.10 shows the spatial pattern sequence of lead-lag regression maps by regressing the anomalies of SST, MSLP and 10-m wind components onto the normalized low-pass filtered NAO index. In this case, to be coherent with the climatological variables patterns related to the AMM in its positive phase, the NAO index is presented in its negative phase. Through lag -30 up to lag -12, we can observe that the SST anomalies are already present in the south of Greenland, although significant values appear only from lag -12 on. At lag -18 up to lag -12, anomalous easterlies form in this region, where there the greater MSLP gradient. MSLP anomalies first organize in the Iceland Low at lag -12, and continuing to grow in the following lags until the full establishment of the NAO pattern (lag 0). In contrast to the SSTA in the south of Greenland, the SSTA over the northeast coast of South America is not accompanied by MSLP or wind anomalies. Statistical significant SSTA over this region starts to expand throughout the TNA, from the coast of South America until reaching the West African coast, from lag -18 up to lag -6. This SSTA spatial propagation that covers all the TNA seems to precede the NAO pattern since the NAO only organizes at the lag -6, and the anomalous Azores High associated

conditions appear at lag -6 up to lag 0. Therefore, is unlikely that the SSTA propagation is forced by any atmospheric conditions related to the NAO pattern formation, in particular with the Azores High. Anomalous westerly winds blowing in the subtropical North Atlantic region first appear at lag -6, after the SSTA propagation from the west to east of the TNA basin, and extending into deep TNA at lag 0 and maintaining up to lag 12.

Figure 6.10 - Lead-lag regression maps of SST (shaded 0.05 °C), MSLP (contour 0.2 hPa) and 10-m wind components (vectors) onto low-pass filtered NAO index.



For the SST, dotted areas are statistically significant at the 95% confidence level. For MSLP, solid contours denote positive values, dashed contours denote negative values, and the zero contour has been omitted. For 10-m wind components, only values greater than 0.15 m s^{-1} are plotted. Since the regression slope coefficients are obtained with the normalized NAO index, the values of each field represent variations per standard deviation of the NAO index. Positive lags indicate that NAO index is leading. Datasets are provided by the 20CRv2 and ERSSTv4 reanalysis.

Source: by the author.

The tropical SST/10-m winds meridional gradient that characterizes the AMM pattern does not project in the filtered NAO index regression in any specific lag, although there is a weak interhemispheric SSTA dipole from lag 6 to lag 18. But the winds only project over the TNA. Nevertheless, the significant SSTA over the TNA and the westerly surface wind anomalies opposing the dominant easterlies trade winds in the TNA, can be the conditions to force the WES mechanism that leads to the AMM. The missing AMM pattern projection on the NAO index regression is the argument advanced by Ruiz-Barradas et al., (2000) to conclude the lack of relationship between the two modes. In spite of having the same results, it is shown that the NAO pattern projects in the AMM index (either filtered and unfiltered), leading the AMM pattern by few months, and the NAO is associated with SSTA and surface anomalies over the TNA which characterizes specific conditions to trigger AMM events. Interestingly, the SSTA propagation over the TNA seems to precede the NAO and can influence the sensitivity of the TNA to a NAO external forcing which through the WES feedback mechanism can expand the signal into deep tropics and potentially interhemispheric. Thus, the conclusion that it is advanced is that the AMO does not excite the AMM through a physical mechanism, instead, it generates the SST conditions over the TNA to a NAO variation.

Hence, the NAO is very likely an external forcing of the AMM decadal time scale variability. However, its influence probably cooperates with the influence exerted by the AMO, since Figure 6.10 shows the presence of SST anomalies over the North Atlantic at negative lags. Such cooperation would lie upon the nature of the interaction between the NAO and AMO, which has revealed a complex one and is still under debate. The physical mechanism that can drive the low-frequency NAO fluctuations remains to be clarified, with some studies indicating to be predominantly caused by internal dynamical atmospheric processes (FELDSTEIN, 2000; HURRELL; DESER, 2010), and others pointing out potential influences from stratospheric-tropospheric coupling (SCAIFE et al., 2005; KIDSTON et al., 2015) and North Atlantic SST variability caused by the AMOC (TIMMERMANN; LATIF, 1998). Regarding AMO, the mechanism that drives its variability still raises uncertainties. Disputing conclusions have been proposed. For instance, Clement et al., (2015) shows that the AMO main features are reproduced in slab ocean models, in which the ocean heat transport is prescribed. They conclude that the AMO represents the low-

frequency response to the NAO high-frequency atmospheric noise and the thermal coupling (i.e. WES positive feedback) extending the signal into the tropics. Changes in the SST over the North Atlantic due to turbulent surface heat flux anomalies driven by variations of the NAO on seasonal and interannual time scales have been reported (CAYAN, 1992; GULEV et al., 2013; GASTINEAU; FRANKIGNOUL, 2015), causing the formation of an anomalous SST tripole pattern over North Atlantic (Figure 6.10, lag0 to lag12). The anomalous SST tripole pattern consists of positive (negative) NAO forcing positive (negative) SST anomalies in the western part of subtropical North Atlantic and negative (positive) SST anomalies in the subpolar gyre and in the TNA. Guan and Nigam, (2009) observed that NAO leads the tripole SST anomalies by two seasons. However, at lower frequencies which characterize the AMO, several studies highlighted other features than the NAO influence. The indirect effect of the aerosols has been proposed as a driver of the AMO (BOOTH et al., 2012) but most of the studies suggest that the AMO is the ocean surface manifestation of the AMOC variability (DELWORTH; MANN, 2000a; KNIGHT et al., 2005; LATIF MOJIB; KEENLYSIDE, 2011; ZHANG; WANG, 2013; MARINI; FRANKIGNOUL, 2014). Many works using climate model simulations show that the intensification (reduction) of the AMOC leads to positive (negative) AMO phase, suggesting the connection between SST variations over North Atlantic and fluctuations in the ocean northward heat transport (DELWORTH; MANABE; STOUFFER, 1993; TIMMERMANN; LATIF, 1998; KNIGHT et al., 2005; ZHANG, 2008; BA et al., 2014; MARINI; FRANKIGNOUL, 2014). Lozier, (2012) in a recent review, however, indicates that the relationship between AMOC and SST variability in the North Atlantic using observational datasets remains to be shown.

Thus, concerning the NAO and AMO interaction, Guan and Nigam, (2009) based on observational datasets, reports that the two modes have different temporal variability and they are essentially uncorrelated. Ba et al., (2014), in a multi-model study, show that the AMOC is the main driver of the AMO but found no linear link on decadal time scales between AMOC and NAO. Nonetheless, there are modeling studies that find a link between the SST anomalies and NAO evolving feedback process between atmosphere and ocean (TIMMERMANN; LATIF, 1998; FARNETI; VALLIS, 2011; GASTINEAU; D'ANDREA; FRANKIGNOUL, 2013). This implies that the results are model dependent. For instance, Wen et al., (2016) using a climate model found

that there is a coupled variability of AMOC and NAO in decadal time scale, being this coupling more effective when compared with the simulations produced by the same with lower resolution. In summary, the mechanism of the possible interaction between the AMO and NAO remains to be explained (GASTINEAU; D'ANDREA; FRANKIGNOUL, 2013).

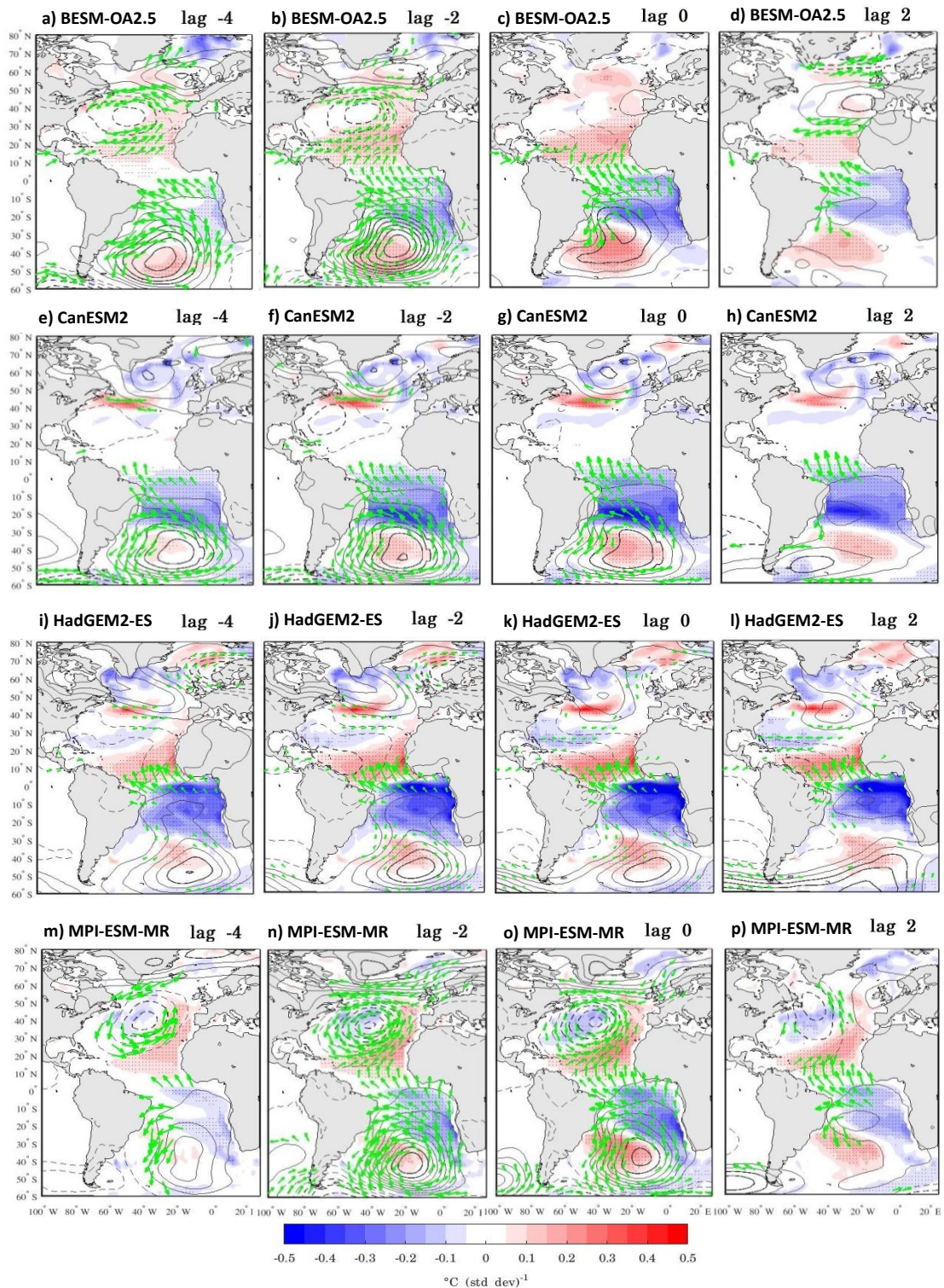
Based on the previous discussion, in the light of the current scientific knowledge, it seems reasonable to assume that the NAO and AMO are either independent modes or that AMO reinforces the NAO phase. In the former scenario, the AMO phase precondition the SST anomalies in the TNA which gives the conditions to an AMM formation when triggered by the NAO forcing that propagates into the tropics as a coupled mode by the WES positive feedback. In the latter scenario, both modes interact with each other modulation and raise the SST anomalies precondition in the TNA leading to an AMM event triggered by NAO variation. Hence, the firm conclusion on what explains the dominant decadal variability (~11-13 yr) of the AMM and improve its predictability relies upon a further understanding of the interaction between the atmospheric and ocean surface conditions generated by the NAO and AMO.

6.6 NAO influence on AMM in four state-of-the-art models

Following the analysis illustrated in Figure 6.9 which uses observational datasets, similar calculations are performed using the models presented in Chapter 5. Since BESM-OA2.5, HadGEM2-ES and MPI-ESM-MR simulate the AMM very well in the Historical simulation, it is interesting to investigate whether they show the NAO leading function in driving AMM. BESM-OA2.5 and MPI-ESM-MR (first and fourth rows of the Figure 6.11) show clearly that NAO precedes the AMM formation through the lead-lag pattern evolution of the MSLP and surface wind patterns, from lag -4 to lag 0. Both models simulate a negative NAO pattern at lag -4 to lag -2 with the associated wind pattern preceding the formation of the AMM in its positive phase, and NAO pattern rapidly disappears from lag 0. HadGEM2-ES simulates a strong interhemispheric SSTA gradient to which the surface winds in the deep tropics seem to respond. However, the AMM is not generated by NAO influence and rather seems to be an internal tropical Atlantic mode (Figure 6.11, third row). CanESM2 is not able

to simulate the AMM as a tropical Atlantic coupled variability. Instead, it simulates a monopole variability centered in the subtropical South Atlantic. Through the lead-lag regression map, it is possible to infer that such a pattern is influenced by the South Atlantic Anticyclone, that is likely to drive the dynamical conditions related to the surface wind direction and speed that forces air-sea interaction and ocean surface heat loss. Since the NAO pattern is absent, the mode does not develop to fully AMM pattern. In fact, all the four models simulate a strong South Atlantic Anticyclone associated with the driving conditions to trigger AMM from the southern hemisphere. Such a link is not revealed by the observations (Figure 6.9). Summarizing, based on the results given by BESM-OA2.5, CanESM2 and MPI-ESM-MR, the NAO is likely to be an important external forcing on the AMM formation.

Figure 6.11 - Lead-lag regression maps of SST (shaded 0.05 °C), MSLP (contour 0.2 hPa) and 10-m wind components (vectors) onto AMM index.



BESM-OA2.5 (first row), CanESM2 (second row), HadGEM2-ES (third row) and MPI-ESM-MR (fourth row). For the SST, dotted areas are statistically significant at the 95% confidence level. For MSLP, solid contours denote positive values, dashed contours denote negative values, and the zero contour has been omitted. For 10-m wind components, only values greater than 0.15 m s⁻¹ are plotted. Since the regression slope coefficients are obtained with the normalized NAO index, the values of each field represent variations per standard deviation of the AMM index. Positive lags indicate that AMM index is leading.

Source: by the author.

6.7 Influence of NAO phases on the tropical North Atlantic SST

The impact of the NAO atmospheric conditions on the tropical North Atlantic SSTs is analyzed through the composite method. The positive NAO composite is defined by averaging the SST over the years in which the NAO normalized index is greater than a standard deviation ($>\sigma$), whereas the negative NAO composite is defined by averaging the SST over the years in which the NAO normalized index is lower than $-\sigma$. Observations and the results of four numerical simulations are used to analyze the NAO impact. Regarding the numerical simulations, the results from the fully coupled BESM-OA2.5 Historical simulation (CPLD), an ocean-only model simulation forced by observed atmospheric conditions (Ocean-INTER), and two ocean-only model simulations forced by the negative NAO composite (Ocean-NEG) and by the positive NAO composite (Ocean-POS), respectively, are used in the analysis. The numerical simulations are described in the methodology section (chapter 2).

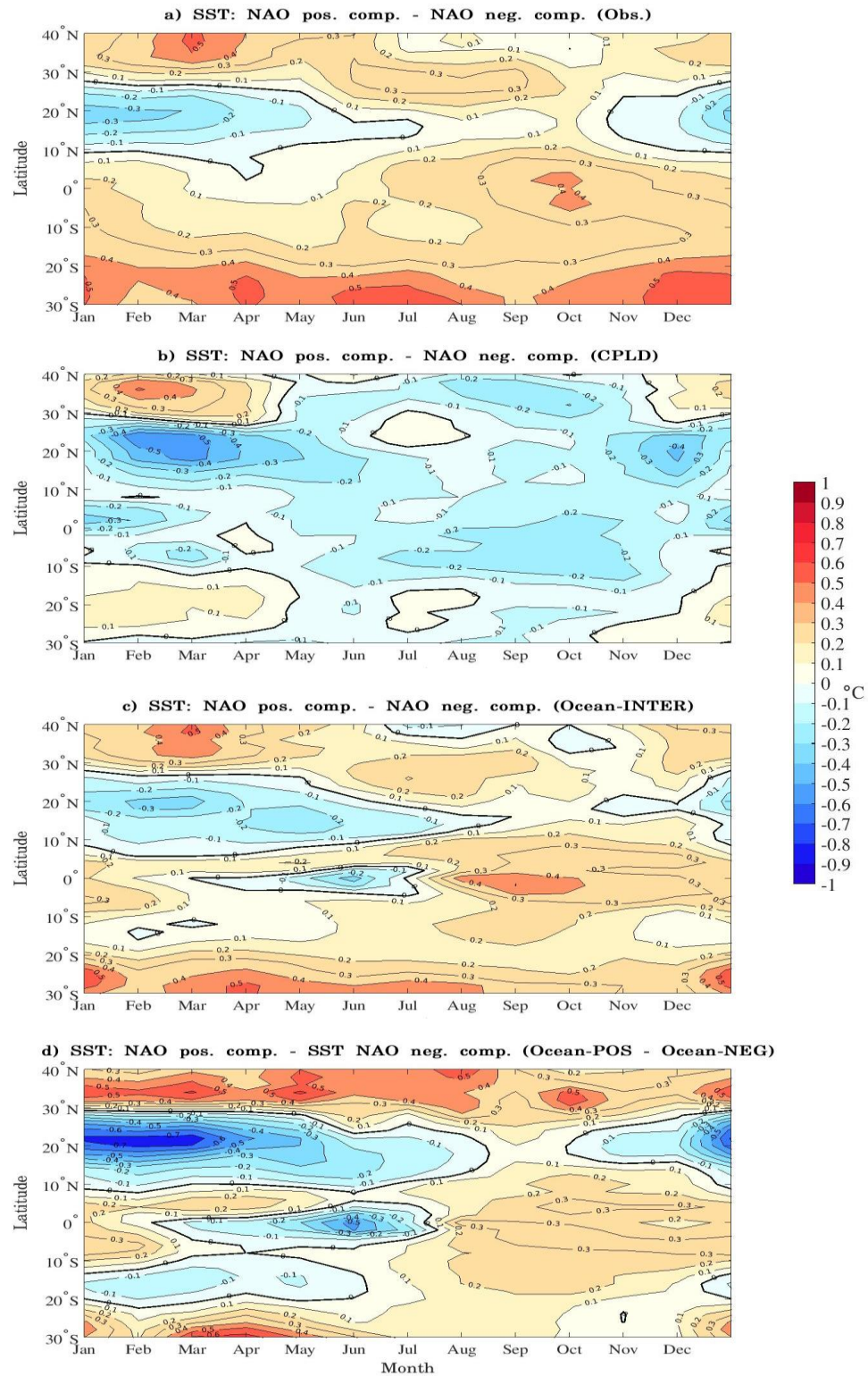
For the Historical simulation, the NAO index is computed through the EOF method applied to the MSLP for the boreal winter season (DJF). Nonetheless, by comparing this index with the index given by the method used by Hurrell, the correlation is 0.97. Based on the NAO normalized index generated by the simulation, the positive NAO composite is defined based on the years: 1952, 1955, 1962, 1963, 1965, 1966, 1979, 1989, 1995, 1998 and 2000. Conversely, the negative NAO composite is defined based on the years: 1954, 1959, 1964, 1967, 1972, 1974, 1975, 1976, 1982, 1988 and 2001.

The SST is zonally averaged over the Atlantic region $50^{\circ}\text{W} - 10^{\circ}\text{E}$ and $30^{\circ}\text{S} - 40^{\circ}\text{N}$. Therefore, hovmoller diagrams are constructed for each case showing the SST evolution in a time/latitude plane. Here, time goes from January up to December, therefore a composite of the whole year following a NAO maximum/minimum phase. The zonally SST averaged difference between the positive composite and negative composite for the observations, CPLD simulation, Ocean-INTER simulation and Ocean-POS/Ocean-NEG are shown in Figure 6.12.

The composite difference of the observational datasets shows that there is a positive (negative) SST anomalies related to the positive (negative) composite in the region limited between 10°N and 30°N , which spans roughly from the beginning of the year

up to May (Figure 6.12.a). This result indicates that in the years of negative (positive) NAO conditions, i.e. negative (positive) NAO composite, there is a response in the SST in the subtropical North Atlantic due to the reduction (increase) of the climatological trade winds, reinforce anomalous ocean surface latent heat flux over the subtropical North Atlantic, that warms (cools) the SST. Therefore, the composite difference (positive composite – negative composite) shows a clear negative SST in the subtropical North Atlantic (10° N – 30° N) in the DJFM season, when NAO is more active. The BESM-OA2.5 Historical simulation captures this feature (Figure 6.12b). The Ocean-INTER simulation shows that the ocean responds to the atmospheric forcing for the NAO composite years in a similar way of the observations (Figure 6.12c). The impact of positive and negative phases of the NAO on the SST over the tropical North Atlantic given the observations is corroborated by the coupled and ocean-only forced experiments. These results corroborate previous studies (HURRELL; DESER, 2010). The difference of SST simulated by the idealized ocean-only experiments using as atmospheric forcing by persistent NAO positive and negative phases reinforces the conclusion above (Figure 6.12d).

Figure 6.12 - Latitudinal hovmoller diagrams for zonally averaged (50 °W-10 °E) SST difference between NAO positive and negative composites.



a) observations, b) coupled simulation, c) ocean-only forced with observed atmospheric fields and d) ocean-only forced with NAO composites atmospheric fields.

Source: by the author.

6.8 Section Summary

In this section, it is explored the link between oceanic and atmospheric large-scale variabilities and AMM decadal variability. For the ocean component, SST and OHC300 variabilities in the Atlantic basin are analyzed with the aim of inferring whether there is a significant statistical link of those ocean variabilities and the predominant decadal variability of the AMM. Regarding SST anomalies variability, the study corroborates Vimont and Kossin (2007) by showing that SST anomalies variability in the region where the AMO has its highest peak (south of Greenland) is highly correlated to the AMM on decadal time scales. To further understand the ocean influence, it is analyzed the upper ocean heat content at 300 m, that is influenced by the northward heat transport driven by the upper cell of the AMOC. The results show that, although there are significant zero-lag statistical links between the AMM and OHC300 in regions as the south of Greenland and the eastern part of Atlantic mid-latitudes, there is an absence of statistical causality driven by the OHC300 variability in those regions. The atmospheric component has been more studied, in particular, the atmospheric circulation changes caused by SSTA variabilities in the equatorial Pacific (El Niño/La Niña events) and by the NAO in the subtropical North Atlantic. Although ENSO impact has not raised special debate, a lack of solid conclusion remains concerning to the NAO influence on the AMM. In this study, through lead-lag relationship was possible to show that NAO precedes the AMM by roughly 2 months. This result contributes to suggest a firm conclusion that the NAO precedes and influence the AMM on interannual and decadal time scales. Results from Earth System Models corroborate this conclusion. Moreover, analyzing jointly the ocean and atmospheric components, the AMO and NAO seems to cooperate in driving the AMM on decadal time scales, with the positive (negative) AMO warming (cooling) the Tropical North Atlantic, and positive (negative) NAO events triggering conditions for formation of positive (negative) AMM events.

7 SIMULATED AMM IN THE IDEALIZED ABRUPT 4xCO₂ EXPERIMENT

7.1 Introduction

The aim of the work presented in this chapter is to investigate how the AMM may respond to perturbed AMOC and to a warmer climate scenario. It is also analyzed what is the nature of the AMOC response to a perturbed climate. The CMIP5 4xCO₂ simulation is the climate scenario used (TAYLOR; STOUFFER; MEEHL, 2012). In this experiment, the atmospheric CO₂ concentration is abruptly quadrupled (1120 ppmv) from its preindustrial level (280 ppmv) and then kept fixed up to the end of the simulation. The simulation used here spans for 150 years, which is generally the period of 4xCO₂ experiments. In order to assess a more general estimate of the AMM response, it is analyzed results from BESM-OA2.5, BNU-ESM (JI et al., 2014), CanESM2 (CHYLEK et al., 2011) and HadGEM2-ES (COLLINS et al., 2011). Table 6.1 shows the description of the models. The piControl simulation, which is a non-perturbed experiment with the atmospheric CO₂ concentration fixed at its pre-industrial level, is the respective control simulation. The period analyzed for the piControl simulation is the correspondent time period of the 4xCO₂ simulation; for instance, if the abrupt quadruplication of CO₂ concentration begins at the 101 yr and 4xCO₂ simulation runs for 150 years, then the period of the piControl simulation to be analyzed and compared with 4xCO₂ is from 101 to 250 yr. The aim is to explore how the AMM may change under perturbed climate system, but focusing on the period which the system has already achieved its stable phase, therefore after the transient phase. To define the stable phase it is used two indicators: the surface air temperature and the AMOC. After the perturbation, it is assumed that the climate system has achieved a new equilibrium and has already entered its stable phase when both have achieved a stationary behavior. In particular, it is assumed the AMOC long-term stability as a key indicator of a stable phase of the Atlantic Ocean circulation. Moreover, AMOC is considered a tipping-point of the Earth's climate due to its ability to regulate the climate system, and for being highly sensitive to small changes in external forcing (LENTON et al., 2008; LENTON, 2011; CAI; LENTON; LONTZEK, 2016). This means that AMOC is likely to respond in a strongly

nonlinear way to external forcing and potentially change its state (LENTON et al., 2008).

Several studies have been focused on the possible response of the AMOC in a perturbed climate scenario, either under the steady increasing of CO₂ in scenarios given by Representative Concentration Pathways (RCPs) simulations or in abruptly quadrupled 4×CO₂ simulation (STOUFFER et al., 2006; WEAVER et al., 2012; CHENG; CHIANG; ZHANG, 2013; GIERZ; LOHMANN; WEI, 2015). In general, these studies show that in a global warming scenario the AMOC tends to reduce its overturning strength and the ability to transport upper warmer waters from low latitudes to higher latitudes in the North Atlantic (STOUFFER et al., 2006; MIKOLAJEWICZ et al., 2007; GIERZ; LOHMANN; WEI, 2015). The AMOC weakening is likely to be caused by melting of the sea and continental ice in high-latitudes North Atlantic, which increases the amount of fresh and lighter water in the region of deep convection in the Nordic Sea, the Labrador Sea and South of Greenland, i.e. North Atlantic Deep Water (NADW) formation region. Such conditions tend to decrease the vertical density gradient that drives the deep water formation and impacting the overturning strength of the AMOC; which turns to reduce the northward transport of salty water associated with the AMOC and eventually reinforcing the cycle in a positive feedback (LOZIER, 2012; RAHMSTORF et al., 2015).

Table 7.1 - The description of the models used.

Institute	Model	Simulation	horizontal resolution (lat×lon)	
			Atmosphere	Ocean
Brazilian National Institute for Space Research (Brazil)	BESM-OA2.5	piControl and 4×CO2 r1i1p1	1.875° × 1.875°	0.25°, 1°×1°
¹ Beijing Normal University (China)	BNU-ESM	piControl and 4×CO2 r1i1p1	2.791°× 2.813°	0.334°, 1°×1°
Canadian Centre for Climate Modelling and Analysis (Canada)	CanESM2	piControl and 4×CO2 r1i1p1	2.791°× 2.813°	0.93°, 1.141° ×1.406°
Met Office Hadley Centre (UK)	HadGEM2-ES	piControl and 4×CO2 r1i1p1	1.25°×1.875°	0.34°, 1°×1°

Models with higher resolution in the tropical region and a decreasing resolution towards the poles have two values for latitude in their respective oceanic resolution column.
Source: by the author

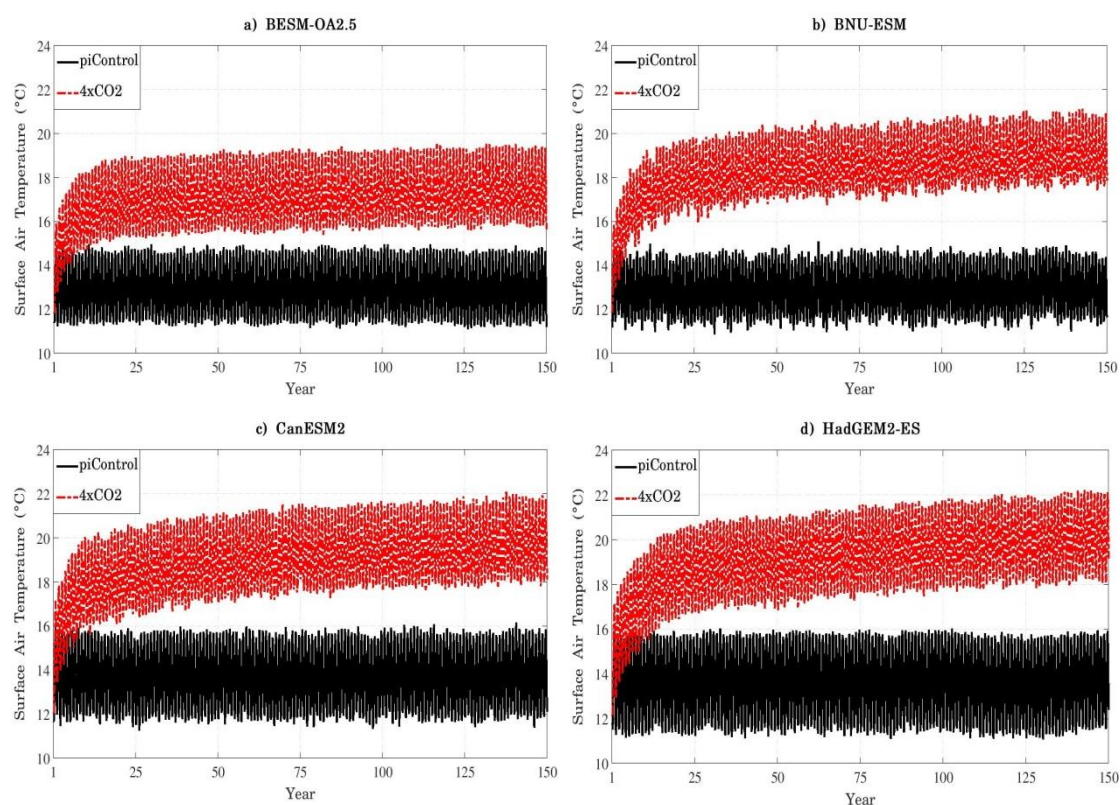
7.2 Surface Air Temperature Response

As mentioned before, the surface air temperature and/or the AMOC are the reference features to assess the stationarity of the climate system in this study. Figure 7.1 shows the globally averaged surface air temperature for the piControl (in black) simulation and the response to the abruptly quadrupled CO₂ atmospheric concentration, i.e. the 4×CO₂ simulation (in red), for the four models used. To compare the surface air temperature for each simulation and between the models, the last 60 years (period 91–150 yr) of simulations are used, a period that follows the fast transitory response to the perturbation. The highest air temperature increase is given by the HadGEM2-ES with an average increase of 6.3 °C, i.e. the difference between the 4×CO₂ and piControl for last 60 years (Figure 7.1d). HadGEM2-ES also presents the highest trend with a value of 0.1 °C decade⁻¹. BESM-OA2.5 has the lowest increase in the surface air temperature with an increase of 4.4 °C (4xCO₂ – piControl) and the lowest

¹ The calculation of the AMOC for the MPI-ESM-MR model showed unrealistic values to be used to compare with the other models. For that reason - and until such differences can be understood - we preferred to use a fourth model (BNU-ESM) for these comparisons since it presents reasonable representation of the AMOC.

trend ($0.03\text{ }^{\circ}\text{C decade}^{-1}$) (Figure 7.1a). BNU-ESM has an average increase of $6\text{ }^{\circ}\text{C}$ and a trend of $0.06\text{ }^{\circ}\text{C decade}^{-1}$ (Figure 7.1b). CanESM2 has an average increase of $5.9\text{ }^{\circ}\text{C}$ and a trend of $0.06\text{ }^{\circ}\text{C decade}^{-1}$ (Figure 7.1c). It should be noted that none of the models reaches an equilibrium state for surface air temperature. All models are consistent in the time scale response to abrupt quadrupled CO_2 atmospheric concentration, with a sharp response in the first 25 years.

Figure 7.1 - Monthly time series of global mean surface air temperature for the $4\times\text{CO}_2$ (red line) and the piControl (black line) simulations.



(a) BESM-OA2.5, (b) BNU-ESM, (c) CanESM2 and (d) HadGEM2-ES. Units are in $^{\circ}\text{C}$.

Source: by the author.

7.3 AMOC Response

An important feature in a perturbed climate system scenario are the changes which the AMOC may suffer. Figure 7.2, 7.3, 7.4 and 7.5 show the AMOC response by comparing $4\times\text{CO}_2$ and piControl simulations performed by BESM-OA2.5, BNU-ESM, CanESM2 and HadGEM2-ES, respectively. Concerning the BESM-OA2.5 simulations, the piControl simulation shows an AMOC pattern similar to the general structure inferred from observations (LUMPKIN; SPEER, 2007); with northward

water flux in the upper limb (from the surface up to ~1000 m) of the upper overturning cell and the southward water flux in the deeper layers of the upper overturning cell (~1000 m up to ~4000 m); and the northward Antarctic Bottom Water in the ocean floor in the lower cell, although is not so prominent (Figure 7.2a). This is considered the AMOC warm mode and is the present-day observed AMOC mode (RAHMSTORF, 2002, Figure 2). The maximum value of the AMOC is about 15 Sv ($1 \text{ Sv} \equiv 10^6 \text{ m}^3 \text{ s}^{-1}$) which is slightly lower than the 17.2 Sv maximum mean strength observed by the project RAPID at 26.5 °N (MCCARTHY et al., 2015). In the present work, the maximum strength of the AMOC is defined in the latitude and depth in which the AMOC has its time-averaged maximum in the piControl simulation (Figure 7.2a). In the case of BESM-OA2.5, the maximum strength of the AMOC is located at the latitude of 28° N and depth of 800 m. It is relative to these coordinates that the strength of the AMOC is compared in both simulations. RAPID measurements at 26.5° N estimate a maximum AMOC at the depth of ~1100 m (MCCARTHY et al., 2015). The 4×CO₂ simulation shows that as the response to the abruptly perturbed climate system the AMOC changes significantly (Figure 7.2b). There is a shallowing of the upper cell of the AMOC and a reduction of the overturning flux, in which the northward water flux is not able to reach higher latitudes (~40°–60° N). The lower overturning cell becomes slightly more vigorous with a stronger AABW. This response is in accordance to the AMOC cold mode, in which the AMOC is weaker and its upper overturning cell is displaced southward (RAHMSTORF, 2002, Figure 2) Figure 7.2c shows the significant reduction of the AMOC strength in the latitude and depth of the maximum AMOC simulated by the piControl simulation. The 4×CO₂ simulates a decrease of ~53% comparing to the maximum strength of the AMOC region of the piControl simulation. The immediate response to the abrupt rise of CO₂ is a fast but steady decrease of the maximum strength of the AMOC down to about 7 Sv in the first 90 years of 4×CO₂ simulation. Thereafter, the AMOC seems to reach an equilibrium phase in the last 60 years of simulation.

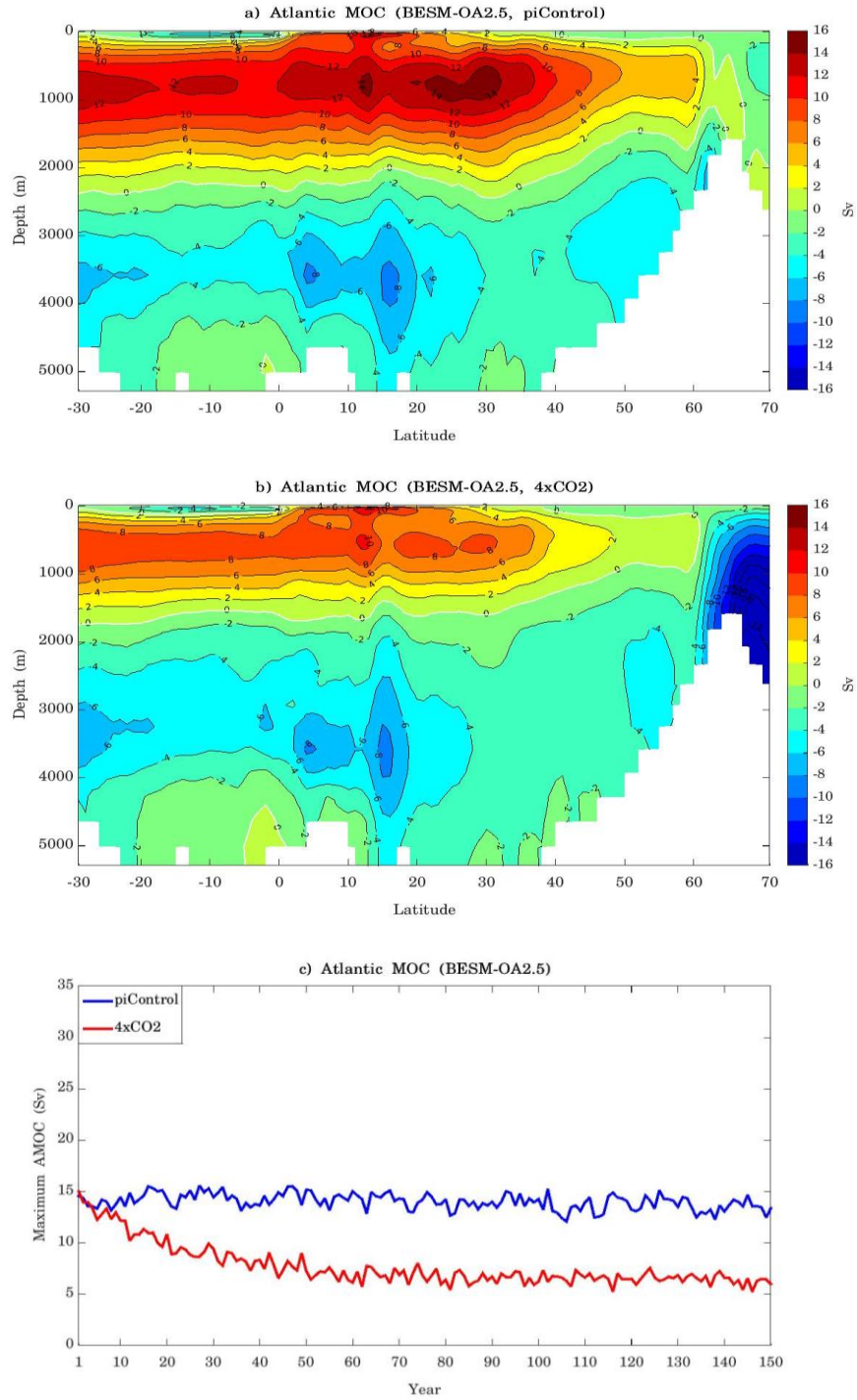
The BNU-ESM piControl simulates a strong AMOC with a maximum strength of 28 Sv, well above the maximum strength which has been observed by the RAPID project or compared the estimate of 21 Sv based on the global ocean re-analyses (MASINA et

al., 2011). The model seems to only simulate a vigorous upper overturning cell, with the upper limb associated with the northward water transport reaching a deeper depth compared with other models (~2000 m) and the NADW filling the deeper ocean without the presence of the lower cell and AABW (Figure 7.3a). The maximum strength of the AMOC is located at the latitude of 35° N and depth of 1500 m. The 4×CO₂ simulation forces the northward upper layer of the upper overturning cell to shallow from ~2000 m to ~1500 m (Figure 7.3b). There is a significant weakening of the northward upper layer and southward displacement, with the maximum strength of the AMOC in the 4×CO₂ simulation reducing considerably up to about 10 Sv, which is a reduction of 66% from the piControl maximum (Figure 7.3c). Moreover, this reduction happens in a very fast way and it takes only 40 years before the maximum strength of the AMOC stabilizes, which is the lowest relaxation time of all models. In the 4×CO₂ simulation, the lower overturning cell of the AMOC emerges and fills the ocean floor (near the equator). Although the upper overturning cell is not accurately simulated, the AMOC response is consistent with a shift from the warm mode to the cold mode.

The CanESM2 piControl simulates an AMOC pattern in which the upper overturning cell is accurately represented, similarly to the pattern obtained from observations (LUMPKIN; SPEER, 2007); however the AABW is not very prominent in the simulation (Figure 7.4a). The maximum strength of AMOC is found at the latitude of 37° N and depth of 700 m; with a value of 15 Sv. In response to the abruptly increasing concentration of atmospheric CO₂, the northward upper layer of the AMOC shallows but not so strongly as the other models and there is a weakening of this layer, in which the maximum strength of the AMOC reduces to about 8–9 Sv, i.e. a reduction of ~43% respectively to the piControl (Figure 7.4b). Similar to BNU-ESM (Figure 7.3c), this reduction occurs in a very fast way, lasting the first 40 years before the maximum strength of the AMOC stabilizes (Figure 7.4c). In the 4×CO₂ simulation, there is a weakening of the northward upper layer and its southward displacement but the deeper layers show little change compared with other models (Figure 7.4b). Nonetheless, since there is a weakening of the upper overturning cell and its capacity to transport warmer waters to higher latitudes, it seems reasonable to assume that there is a shift from a warm mode to a cold mode.

The HadGEM2-ES piControl simulates an AMOC pattern that is similar to the one obtained from observations (LUMPKIN; SPEER, 2007), and similar to BESM-OA2.5 and CanESM2 simulations. The upper limb of the upper overturning cell fills the first ~1100 m, the deeper layers are filled by the NADW and a weak AABW (Figure 7.5a). The maximum strength of AMOC is found at the latitude of 34° N and depth of 1100 m; with a value of ~15 Sv. In response to the abruptly increasing concentration of atmospheric CO₂, the northward upper layer of the AMOC weakens and shallows slightly (Figure 7.5b). The lower overturning cell strengthens, with a stronger AABW. The maximum strength of the AMOC reduces to an average value of about 6–7 Sv, i.e. a reduction of ~56% (Figure 7.5c). The reduction is stronger in the first 90 years although it does not reach an equilibrium phase. In the last 60 years, the maximum strength of the AMOC maintains a steady slight negative trend in a quasi-equilibrium phase. The AMOC patterns of the simulations are consistent with a shift from the warm mode to the cold mode.

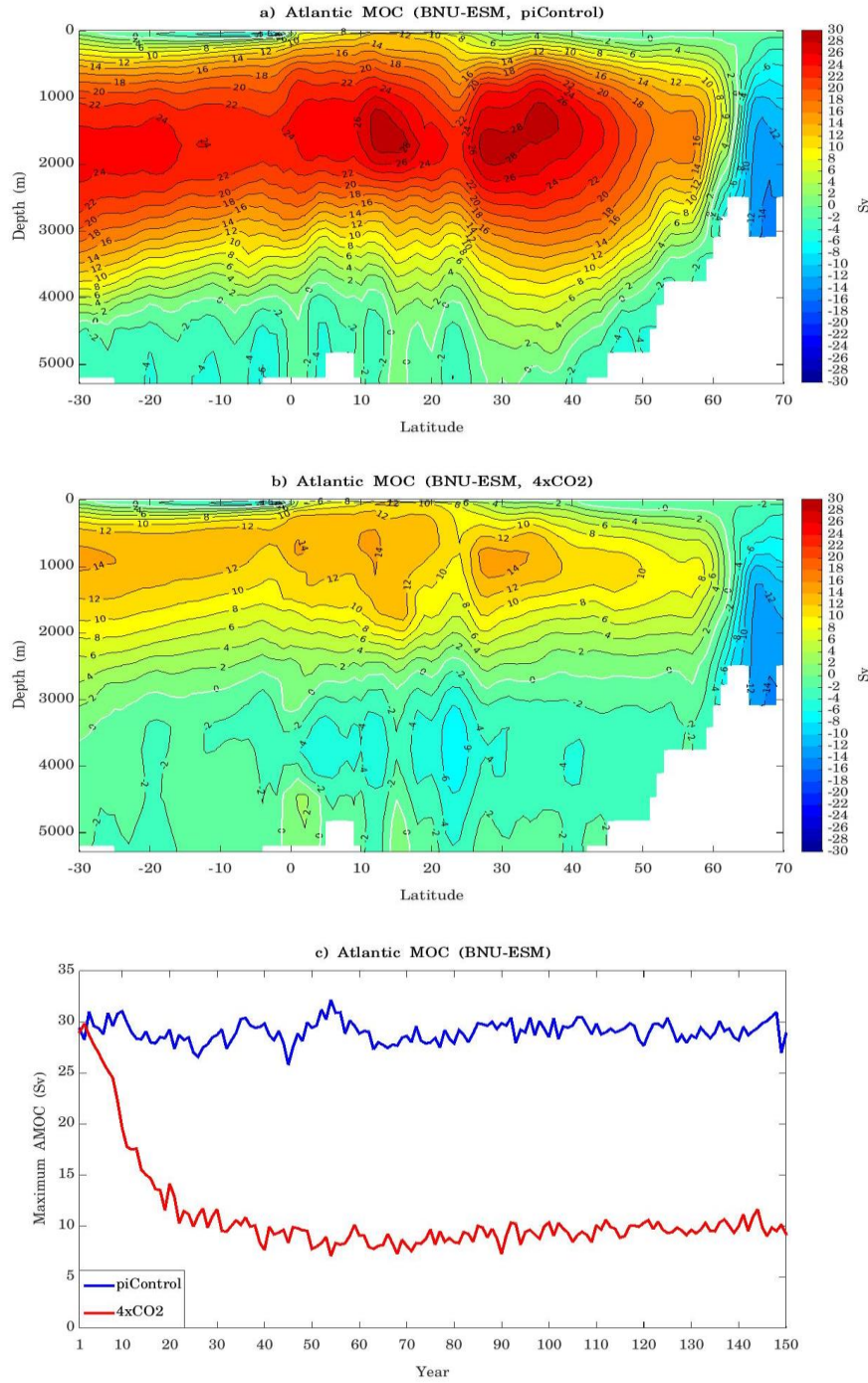
Figure 7.2 - AMOC averaged over the period 91–150 yr simulated by BESM-OA2.5.



(a) piControl and (b) 4×CO₂ experiments. The zero line is plotted in white. (c) The annual mean maximum strength of the AMOC time series for piControl (blue line) and 4×CO₂ (red line) simulations over the whole period. The maximum strength of the AMOC is defined in the latitude and depth in which the AMOC has its time-averaged maxima in the piControl simulation (a). The period selected for (a) and (b) is related to the equilibrium phase that the maximum strength of the AMOC shows in (c). Units are in Sverdrup.

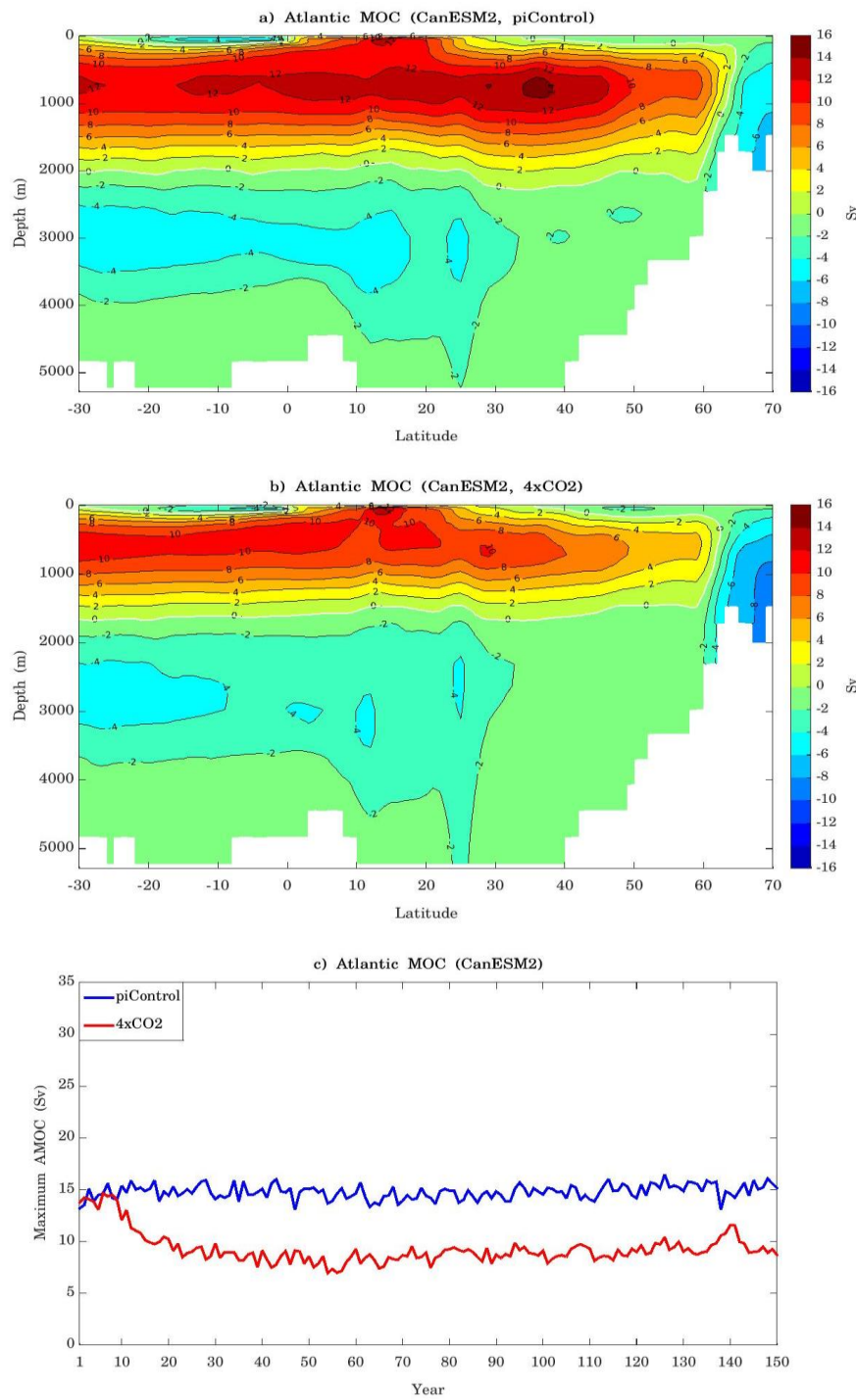
Source: by the author.

Figure 7.3 - AMOC averaged over the period 91–150 yr simulated by BNU-ESM.



(a) piControl and (b) 4×CO₂ experiments. The zero line is plotted in white. (c) The annual mean maximum strength of the AMOC time series for piControl (blue line) and 4×CO₂ (red line) simulations over the whole period. The maximum strength of the AMOC is defined in the latitude and depth in which the AMOC has its time-averaged maxima in the piControl simulation (a). The period selected for (a) and (b) is related to the equilibrium phase that the maximum strength of the AMOC shows in (c). Units are in Sverdrup.
Source: by the author.

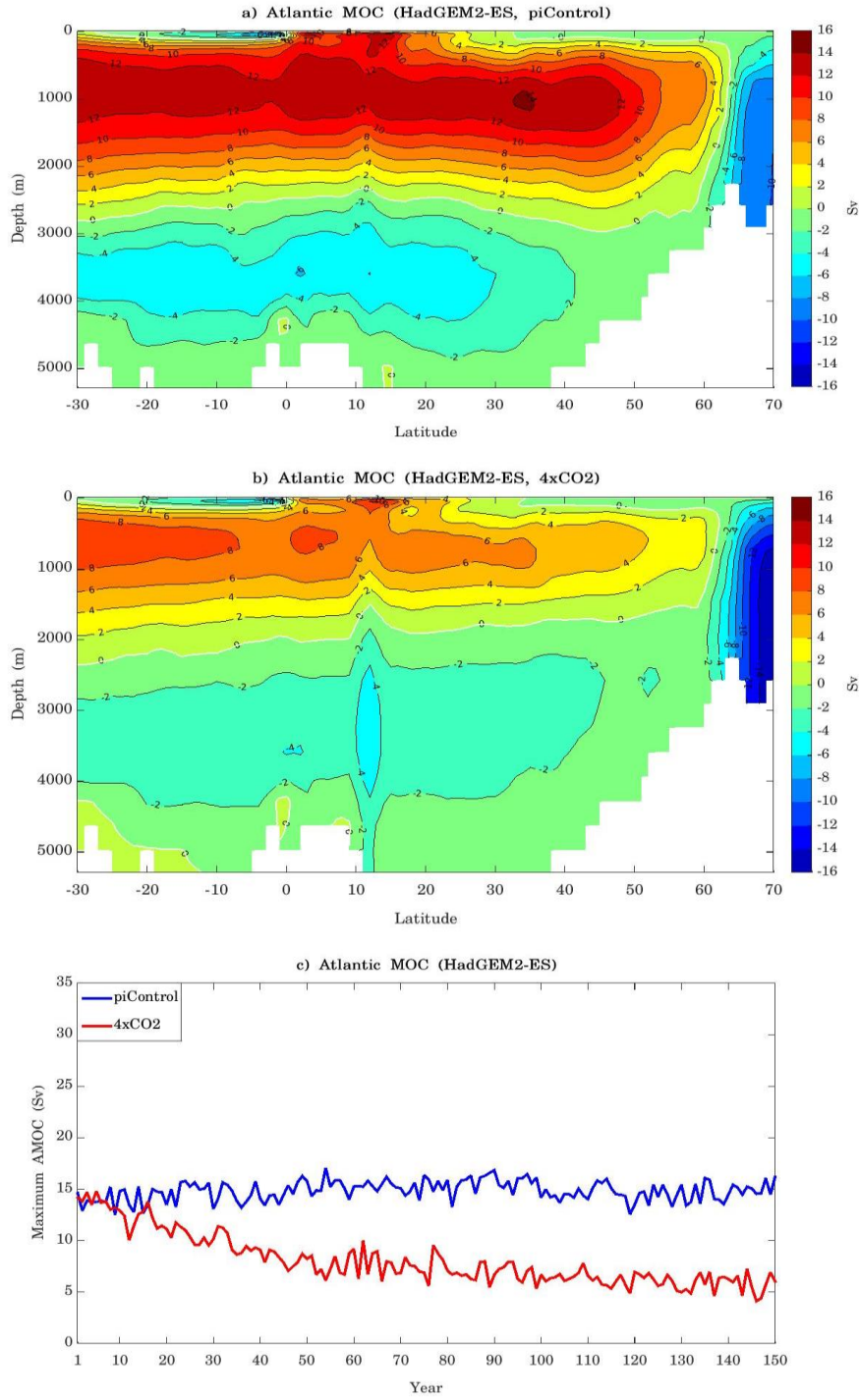
Figure 7.4 - AMOC averaged over the period 91–150 yr simulated by CanESM.



(a) piControl and (b) 4×CO₂ experiments. The zero line is plotted in white. (c) The annual mean maximum strength of the AMOC time series for piControl (blue line) and 4×CO₂ (red line) simulations over the whole period. The maximum strength of the AMOC is defined in the latitude and depth in which the AMOC has its time-averaged maxima in the piControl simulation (a). The period selected for (a) and (b) is related to the equilibrium phase that the maximum strength of the AMOC shows in (c). Units are in Sverdrup.

Source: by the author.

Figure 7.5 - AMOC averaged over the period 91–150 yr simulated by HadGEM2-ES.



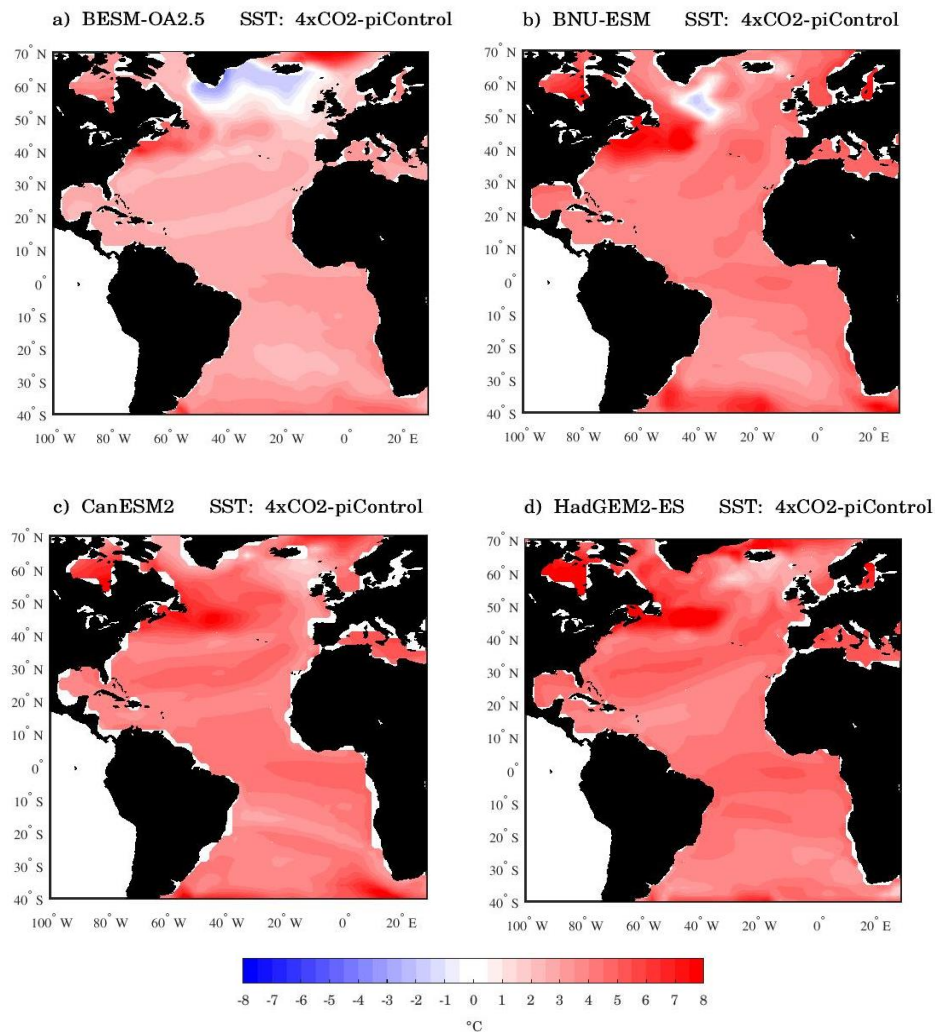
(a) piControl and (b) 4×CO₂ experiments. The zero line is plotted in white. (c) The annual mean maximum strength of the AMOC time series for piControl (blue line) and 4×CO₂ (red line) simulations over the whole period. The maximum strength of the AMOC is defined in the latitude and depth in which the AMOC has its time-averaged maxima in the piControl simulation (a). The period selected for (a) and (b) is related to the equilibrium phase that the maximum strength of the AMOC shows in (c). Units are in Sverdrup.

Source: by the author.

7.4 SST Response

The Atlantic SST response to the abrupt CO₂ increase is inferred through the difference between the 4×CO₂ and piControl simulations (Figure 7.6). The differences are performed using Atlantic SST averaged over the period 91–150 yr, which is the period that 4×CO₂ simulation shows a stable AMOC for all models used. BESM-OA2.5 shows a broad SST warming as a response to an abrupt CO₂ increase (Figure 7.6a). Nevertheless, there is a significant cooling over an extensive area in the North Atlantic subpolar region (40° W–0°; 55°–65° N). This is the region of ocean deep convection, where the NADW forms. The NADW is an important component of the AMOC and changes in NADW formation has a significant influence on the AMOC strength (RAHMSTORF, 2002; LOZIER, 2012). As a response to the abrupt CO₂ increase, the sea ice melts due to the radiative heating and anomalous cold freshwater flow into the North Atlantic deep convection region. This cold freshwater affects the vertical density gradient that drives the NADW formation and inhibits the NADW to form, which consequently weakens the AMOC (LOZIER, 2012). Therefore, the cooler SST observed in the 4×CO₂ simulation is a consequence of the melted sea ice over the North Atlantic. Nowadays, such SST cooling trend in high-latitudes of the North Atlantic has been already reported as consequence of a weakening AMOC and long-term freshening caused by the increase of anthropogenic greenhouse gas in the atmosphere (ROBSON; ORTEGA; SUTTON, 2016). For this reason, despite the global warming trend, the surface air temperature in this region has been cooling and it has been named as the warming hole (DRIJFHOUT; VAN OLDENBORGH; CIMATORIBUS, 2012; RAHMSTORF et al., 2015). BNU-ESM has also a broad SST warming in the Atlantic basin and shows the cooling SST in the North Atlantic subpolar region, however weaker than simulated by BESM-OA2.5 (Figure 7.6b). For the models CanESM2 and HadGEM2-ES, during the stable period, the North Atlantic SST response lacks the formation of cooler surface waters compared with their respective piControl simulations although in the south of Iceland both models show no SST warming (Figure 7.6c and 7.6d).

Figure 7.6 - Atlantic SST difference between the 4xCO₂ and piControl simulations.



(a) BESM-OA2.5, (b) BNU-ESM, (c) CanESM2 and (d) HasGEM2-ES. The differences are computed over the period 91–150 yr. Units are in °C.
Source: by the author.

7.5 AMM response

The response of the AMM to the abrupt quadrupled atmospheric CO₂ concentration is analyzed in each model by comparing the spatial and temporal variability in the 4xCO₂ and in the piControl simulations. The period analyzed spans over 91–150 yr, period that the models are assumed to be stable, based on the maximum AMOC time series of each model. The AMM spatial pattern is reasonably well simulated by BESM-OA2.5 in the piControl, reproducing the interhemispheric SSTA gradient and cross-equatorial surface anomalies following the gradient, from the southern lobe to northern lobe (Figure 7.7a), in a similar way to the observed pattern (Figure2.2a). Nevertheless, the pattern variability is weaker than the observed and also weaker than

simulated in the historical simulation (Figure 5.1a). In particular, the surface winds over the TNA are significantly weaker. The squared covariance fraction is 51.4% slightly lower than the observed one (56%). The AMM response to a perturbed climate is shown in Figure 7.7b. Interestingly, BESM-OA2.5 still reproduces the AMM pattern, with a more vigorous SSTA in the TNA compared with the piControl. Although there is a reduction in the squared covariance fraction from 51.4% (piControl) to 39.9%, the AMM pattern maintains its structure unperturbed. Figures 7.7c and 7.7d show the power spectrum of the AMM-SST time series simulated in piControl and 4×CO₂ experiments, respectively. In the piControl simulation, the temporal variability is dominated by interannual periodicity (~2–4 yr and 8 yr). This result contrast with the dominant decadal periodicity simulated by the Historical experiment (Figure 5.1c). In the 4×CO₂ simulation, the temporal variability maintains its dominant interannual periodicity but the 8 yr periodicity reduces its significance to less than 90%. Nevertheless, overall, the AMM spatio-temporal pattern does not suffer meaningful changes in a warmer planet by 4.4 °C relative to the piControl simulation.

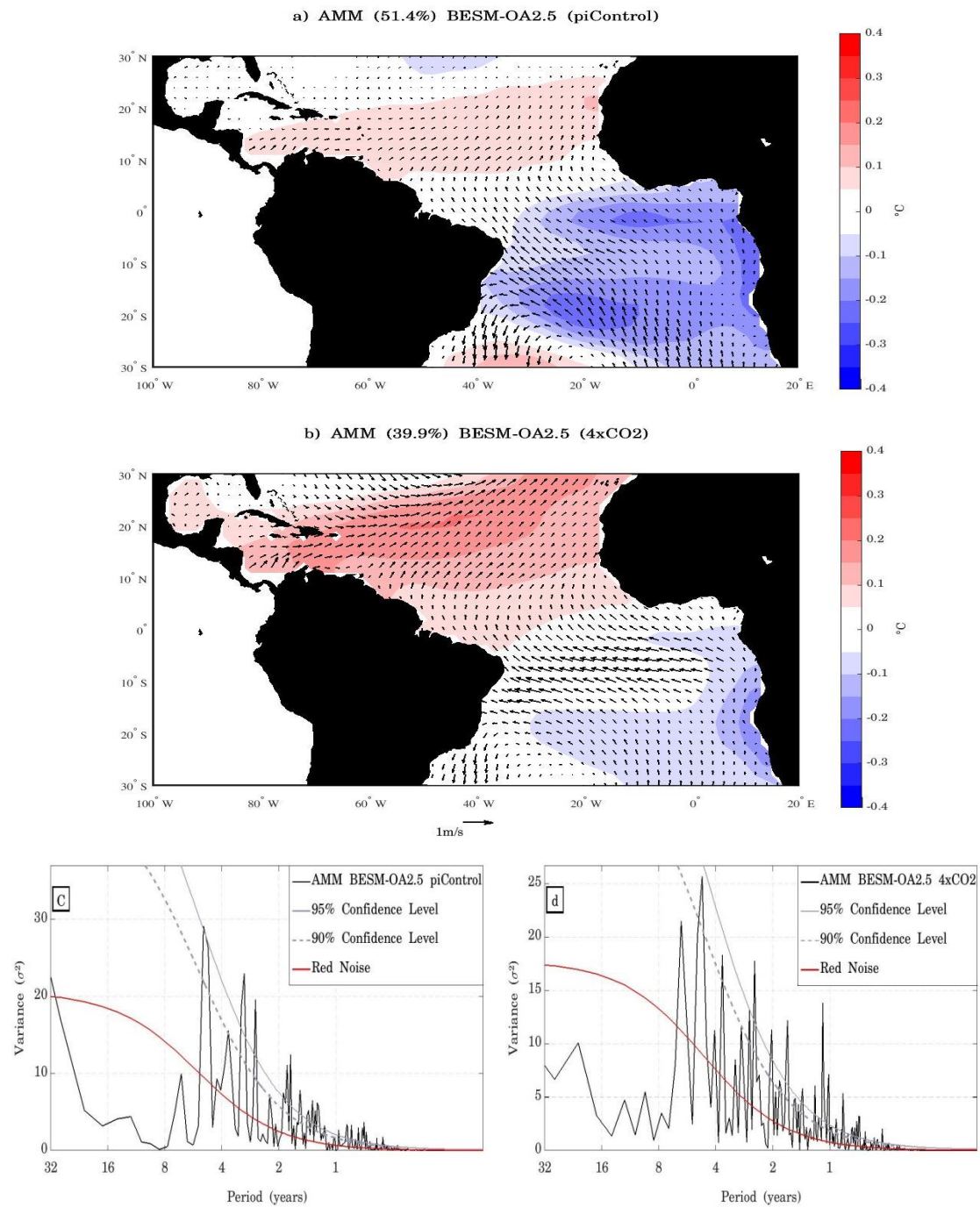
BNU-ESM is not able to accurately simulate the AMM spatial pattern, generating only a monopole of SSTA variability in the TSA and without significant SSTA variability in the TNA (Figure 7.8a). Nevertheless, anomalous cross-equatorial surface winds are coupled with this SSTA monopole, despite the surface wind field anomalies in the TNA are negligible. The second and the third BNU-ESM MCA pattern do not resemble the AMM pattern, so the analysis is done using the leading pattern. The 4×CO₂ simulation shows that the southern monopole pattern of the piControl changes to widely spread uniform variability over the Tropical Atlantic (Figure 7.8b). Although the spatial patterns are different, they represent almost the same square covariance fraction, 50.0% and 56.7% for piControl and 4×CO₂, respectively. Through the power spectrums are possible to observe that both simulations are dominated by interannual variability (~2–5 yr) (Figure 7.8c and 7.8d). So, in this case, the leading spatial pattern shows changes in a perturbed climate although the temporal variability does not change.

The next model analyzed is CanESM2. The piControl simulation reproduces the interhemispheric gradient pattern, despite it simulates weaker surface wind anomalies over TNA and TSA, and surface wind anomalies with strong a zonal component in the western part of equatorial Atlantic, compared with observed pattern (Figure 7.9a and Figure 3.1a). This result contrasts with the CanESM2 Historical simulation in which the AMM pattern mode is not simulated (Figure 5.2a). However, the model's pattern is associated with a less significant mode of variability in the tropical Atlantic coupled system, since it only represents 36.4% of the squared covariance fraction (56.6% for the observed mode). In the 4×CO₂ simulation, the AMM pattern changes to southern monopole pattern, similar to the simulated in the Historical experiment (Figure 7.9b and Figure 5.2a). Although the spatial pattern has changed, the power spectrums do not reveal any significant change (Figure 7.9c and 7.9d). Since the spatial leading coupled pattern simulated by Historical and 4×CO₂ experiments are similar, it is difficult to conclude that the changes occurred in the 4×CO₂ are caused by the abrupt warming of the planet. If such a conclusion is advanced, subsequently, one would conclude that the AMM variability is a non-perturbed mode of the CanESM2 model and in the case of perturbed simulations, as the transient Historical and abrupt 4×CO₂ simulations, the AMM is replaced by other sorts of leading variability over the Atlantic. However, we know that in the present perturbed planet, represented in the model by the forcing conditions of the Historical simulation, the AMM is the leading coupled variability observed in the Tropical Atlantic. Therefore, no conclusion is advanced based on the CanESM2 simulations results.

The HadGEM2-ES model is capable of simulating the interhemispheric gradient pattern accurately, with correct SSTA variability but the surface wind in the equator tends to have a strong zonal component compared with the observation and weak surface wind field over TNA and TSA, similar to the Historical simulation (Figure 7.10a and Figure 5.3a). The AMM spatial pattern remains practically unchanged in the 4×CO₂ simulation (Figure 7.10b). Only a weaker southern lobe of the AMM variability compared with the piControl. The squared covariance fractions are very similar, with 54.8% and 50.3% for piControl and 4×CO₂ simulations, respectively. The piControl power spectrum shows that the AMM has a decadal periodicity significant at 90% confidence level (Figure 7.10c). In the correspondent 4×CO₂ power spectrum, this dominant decadal periodicity loses its significance well below

the 90% confidence level limit (Figure7.10d). This is the only relevant change in the AMM response to the abrupt $4\times\text{CO}_2$ increase. Nevertheless, it should be noted that in the Historical simulation the spectral peak at decadal periodicity is slightly below the 90% confidence level limit (Figure5.3c). Therefore, the AMM decadal periodicity seems to become weaker as the climate forcing conditions enhance.

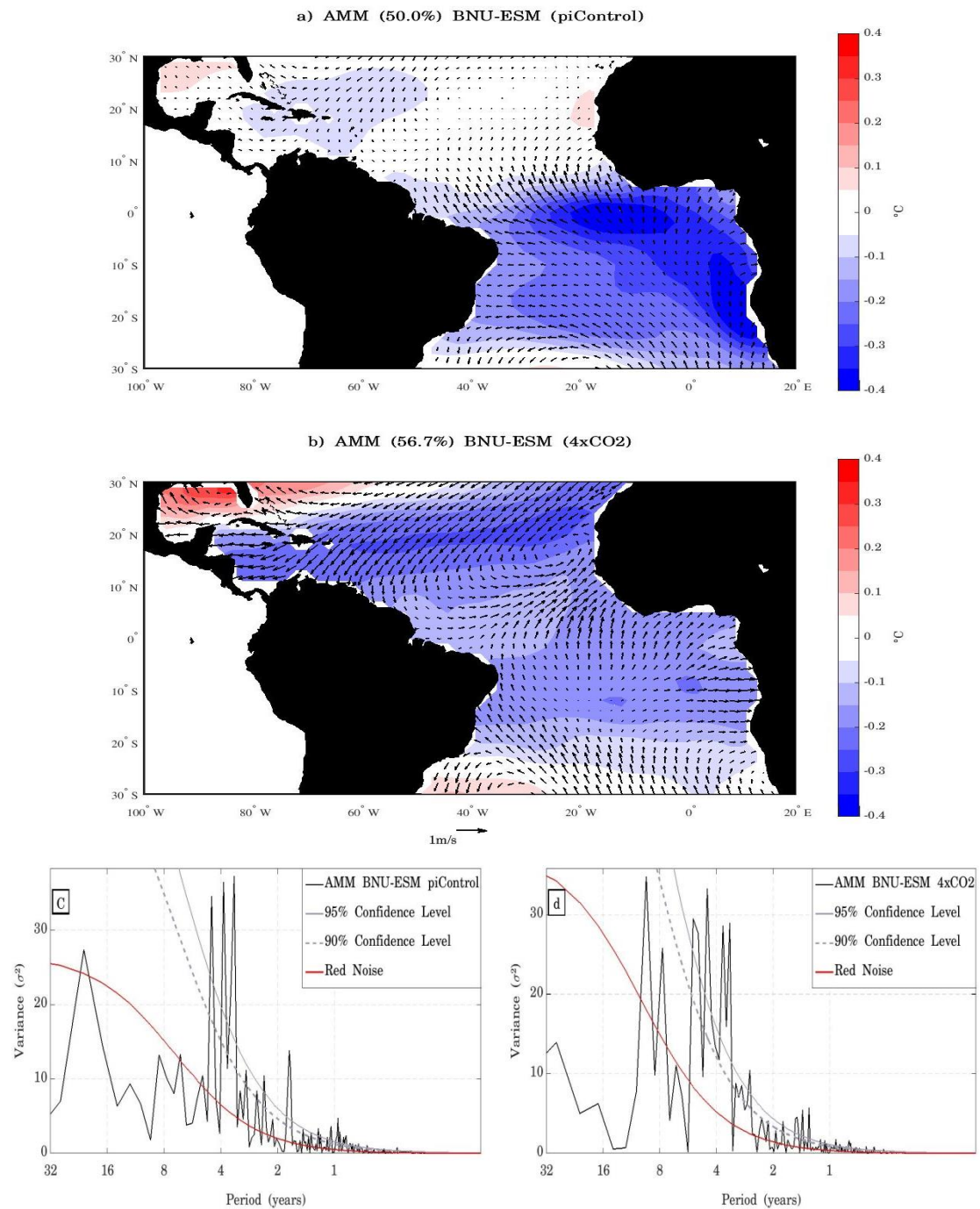
Figure 7.7 - The leading maximum covariance analysis (MCA) mode between SST anomalies (shading, $^{\circ}\text{C}$) and 10-m wind anomalies (arrows, m s^{-1}) over tropical Atlantic (30°S – 30°N) simulated by BESM-OA2.5.



(a) piControl and (b) 4xCO2. The mode is shown as the SSTA and 10-m wind anomalies regressed onto the SST normalized expansion coefficient (AMM-SST) time series ($^{\circ}\text{C}$ per standard deviation) for the period 91–150 years. The contour interval is 0.05°C . Power spectrum of the AMM-SST time series for (c) piControl and (d) 4xCO2, respectively. The solid red line represents the theoretical red noise spectrum, the dashed and solid gray lines represent the 90% and 95% confidence level, respectively. Note that the ordinate axis scales are different.

Source: by the author.

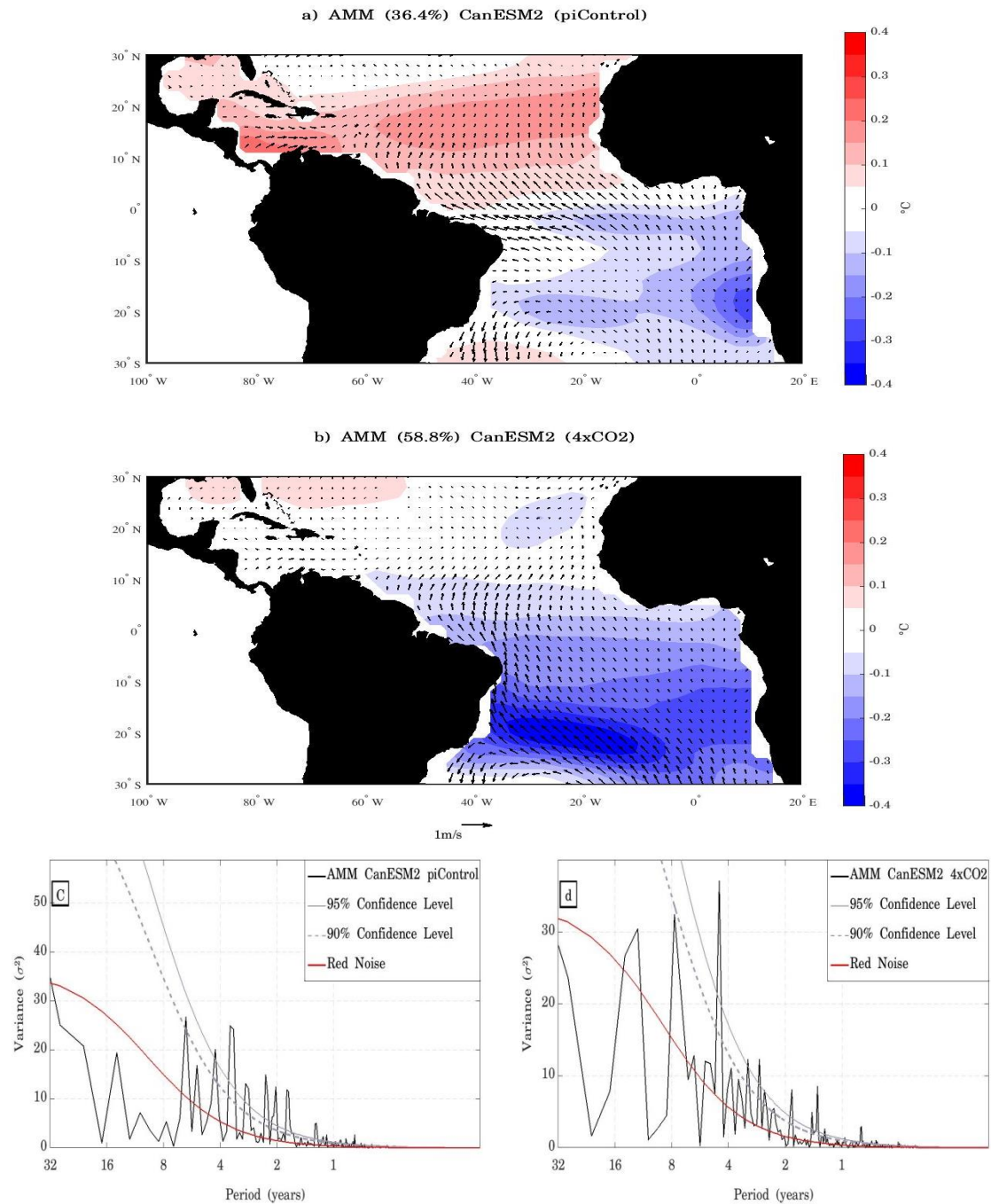
Figure 7.8 - The leading maximum covariance analysis (MCA) mode between SST anomalies (shading, $^{\circ}\text{C}$) and 10-m wind anomalies (arrows, m s^{-1}) over tropical Atlantic (30°S – 30°N) simulated by BNU-ESM.



(a) piControl and (b) 4xCO2. The mode is shown as the SSTA and 10-m wind anomalies regressed onto the SST normalized expansion coefficient (AMM-SST) time series ($^{\circ}\text{C}$ per standard deviation) for the period 91–150 years. The contour interval is 0.05°C . Power spectrum of the AMM-SST time series for (c) piControl and (d) 4xCO2, respectively. The solid red line represents the theoretical red noise spectrum, the dashed and solid gray lines represent the 90% and 95% confidence level, respectively. Note that the ordinate axis scales are different.

Source: by the author.

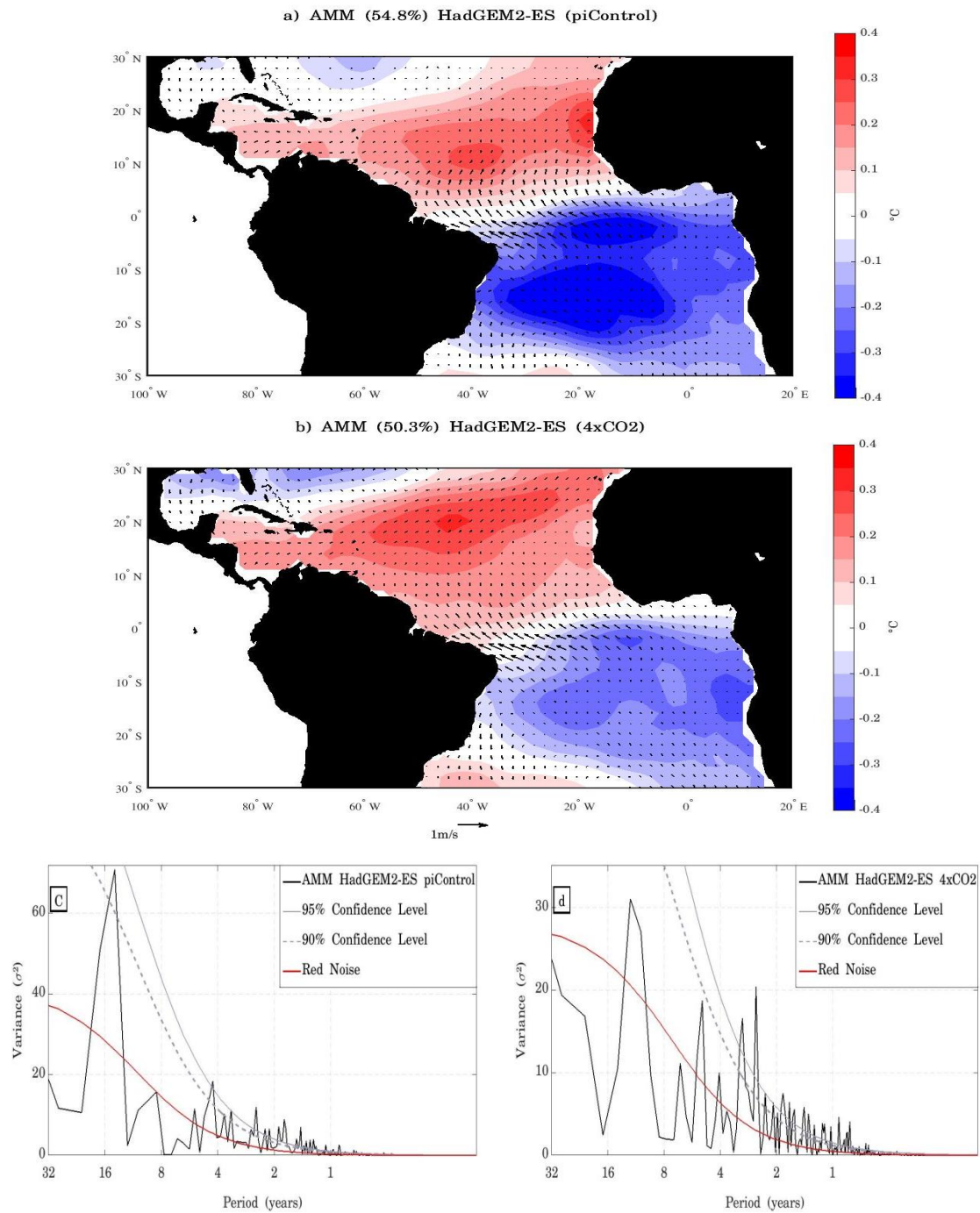
Figure 7.9 - The leading maximum covariance analysis (MCA) mode between SST anomalies (shading, °C) and 10-m wind anomalies (arrows, m s^{-1}) over tropical Atlantic (30° S–30° N) simulated by CanESM2.



(a) piControl and (b) 4×CO₂. The mode is shown as the SSTA and 10-m wind anomalies regressed onto the SST normalized expansion coefficient (AMM-SST) time series (°C per standard deviation) for the period 91–150 years. The contour interval is 0.05 °C. Power spectrum of the AMM-SST time series for (c) piControl and (d) 4×CO₂, respectively. The solid red line represents the theoretical red noise spectrum, the dashed and solid gray lines represent the 90% and 95% confidence level, respectively. Note that the ordinate axis scales are different.

Source: by the author.

Figure 7.10 - The leading maximum covariance analysis (MCA) mode between SST anomalies (shading, °C) and 10-m wind anomalies (arrows, m s^{-1}) over tropical Atlantic (30° S–30° N) simulated by HadGEM2-ES.



(a) piControl and (b) 4xCO2. The mode is shown as the SSTA and 10-m wind anomalies regressed onto the SST normalized expansion coefficient (AMM-SST) time series ($^{\circ}\text{C}$ per standard deviation) for the period 91–150 years. The contour interval is 0.05 $^{\circ}\text{C}$. Power spectrum of the AMM-SST time series for (c) piControl and (d) 4xCO2, respectively. The solid red line represents the theoretical red noise spectrum, the dashed and solid gray lines represent the 90% and 95% confidence level, respectively. Note that the ordinate axis scales are different.

Source: by the author.

7.6 Section Summary

Through idealized simulation are assessed potential changes that may occur to the AMM in a warmer planet and under different AMOC pattern. Using four state-of-the-art Earth System Models, it is compared the simulated AMM of abrupt $4\times\text{CO}_2$ experiment relative to the piControl experiment. The AMOC response is also analyzed.

The changes of the AMOC in response to the climate change scenarios and the associated reduction of the northward water transport to the higher latitudes have been widely studied (STOUFFER et al., 2006; IVERSEN et al., 2013; GIERZ; LOHMANN; WEI, 2015). Weaver et al., (2012) reports a reduction in the maximum strength of the AMOC which ranges from 36% to 44% at the end of 21th century, by analyzing the CMIP5 models under the RCP8.5 scenario. The models analyzed here show a substantial reduction of the AMOC strength and the ability to reach high-latitudes caused by the southward displacement of the upper limb of the upper overturning cell. However, any model has shown an abrupt collapse, in accordance with similar modeling experiments in which there is a significant increase of greenhouse gases (STOUFFER et al., 2006; WEAVER et al., 2012; CHENG; CHIANG; ZHANG, 2013; IVERSEN et al., 2013; GIERZ; LOHMANN; WEI, 2015). This indicates that, for these models, the AMOC shift from the warm mode to the cold mode is the response to an abrupt quadrupled of the atmospheric CO_2 concentration. It should be stressed the appearance of a strong southward water transport in the high-latitudes ($60^\circ\text{--}70^\circ\text{N}$) for all models. The reason for this phenomenon is not clear.

Although BNU-ESM piControl simulation is not able to reproduce the AMM interhemispheric gradient pattern, it reproduces a monopole over the TSA with an associated cross-equatorial wind anomalies field, somewhat mimicking the AMM pattern. The spatial pattern simulated by BNU-ESM abrupt $4\times\text{CO}_2$ simulation over Topical Atlantic is completely different from the one simulated in piControl. More interesting cases occur for BESM-OA2.5, CanESM2 and HadGEM2-ES. These three models simulate the AMM pattern in their respective piControl simulations. In the case of CanESM2, the AMM pattern is not fully reproduced in the $4\times\text{CO}_2$ simulation. This model lacks the AMM leading coupled variability in perturbed simulation

(Historical and abrupt $4\times\text{CO}_2$ simulations). BESM-OA2.5 and HadGEM2-ES simulate the AMM pattern for piControl and perturbed simulations, indicating that the AMM is not affected by a warming planet and by substantial changes in the northward ocean heat transport in the Atlantic basin.

To endorse this result, observational studies based on paleoclimate observational approaches can be useful. The last time the CO_2 concentration level on Earth's atmosphere was similar to modern values (~ 400 ppmv) is traced to Mid-Miocene, roughly ~ 15 million years ago (TRIPATI; ROBERTS; EAGLE, 2009). In that period it is estimated that the global surface air temperature was warmer than present values by 3 to 6 $^{\circ}\text{C}$ (TRIPATI; ROBERTS; EAGLE, 2009). Regarding similar AMOC conditions as simulated by $4\times\text{CO}_2$ simulation, there are studies which indicate that AMOC was shallower and weaker during the Last Glacial Maximum, Late Pleistocene, roughly $\sim 30\text{--}20$ kyr ago, therefore in its cold mode (see LYNCH-STIEGLITZ, 2017). By analyzing sediments deposited in a paleo-lake in northwestern Argentina, Trauth et al., (2003) infers the precipitation variability that occurred 30 kyr ago. The precipitation power spectrum reveals interannual and decadal variabilities (TRAUTH et al., 2003; Figure 4). It is advanced that this precipitation temporal variability is linked to SSTA, in which the interannual variability is related to ENSO and the decadal variability is related to AMM. Using present precipitation dataset for the same region the precipitation power spectral reveals a peak at 13 yr, which is well linked to the present AMM predominant periodicity, whereas the paleo power spectral reveals a peak at 16 yr, which is slightly higher than the periodicity observed in the 20th century but well within the decadal variability spectrum. These results support the robustness of the AMM as leading variability in the Tropical Atlantic even under significant changes in the ocean circulation and weakening of the northward ocean heat transport in the Atlantic that is simulated by BESM-OA2.5 and HadGEM2-ES. Such a result can be indicative that the AMM is not linked to ocean subsurface conditions. However, it should be highlighted that, among the variables analyzed, the AMOC simulated by the $4\times\text{CO}_2$ simulation is the only feature that resembles the AMOC conditions estimate for 30 kyr ago, since the surface air temperatures were ~ 5 $^{\circ}\text{C}$ below modern values (ANNAN; HARGREAVES, 2015) and the averages central to eastern equatorial Atlantic SSTs were 2–6 $^{\circ}\text{C}$ lower than modern values (TREND-STAD; PRELL, 2002).

8 CONCLUSIONS

The present thesis aimed to advance the understanding of the nature of the dominant decadal periodicity which characterizes the Atlantic Meridional Mode (AMM) and the robustness of this ocean-atmosphere tropical Atlantic variability under a perturbed climate scenario. Using observational and reanalysis datasets, different large-scale phenomena, with strong decadal variability that potentially influence the tropical Atlantic climate conditions, were statistically analyzed in order to address their link to the AMM decadal variability. To investigate the changes that the AMM may suffer under perturbed climate scenario, state-of-the-art Earth System Model simulations following the CMIP5 protocol (TAYLOR; STOUFFER; MEEHL, 2012) were used.

Simulations performed by the new version of the coupled ocean-atmosphere component of the Brazilian Earth System Model version 2.5 (BESM-OA2.5) are widely used throughout this work to investigate different features of the AMM. Therefore, it is presented the evaluation on how BESM-OA2.5 performs for the historical period when there are observations to compare with model's calculations. The most relevant climate patterns on interannual to decadal time scales simulated by BESM-OA2.5 are compared with the ones obtained from observations and reanalysis. Over the Pacific, the El Niño-Southern Oscillation (ENSO) is simulated with lower amplitude of variability than the observations and such weak ENSO seems to impact other Pacific variability patterns such as the Pacific Decadal Oscillation. Conversely, the major phenomena on the Atlantic basin are well represented in BESM-OA2.5 simulations. This is the case for the AMM that is very well simulated by the model in term of the spatial pattern and temporal variability. This can be related to the fact that the model simulates very well the NAO, which potentially influences the AMM formation. It is worth to note that this mode is considered poorly simulated by the models used in the IPCC/AR5 (FLATO et al., 2013). It is also relevant to highlight BESM-OA2.5 ability to represent the enhanced rainfall over cooler waters over the SW Tropical Atlantic, associated with the South Atlantic Convergence Zone (SACZ). The capacity of the model in simulating the AMM and SACZ is an important result since one of the main aims is the representation of modes that directly impacts the precipitation over South America. The Atlantic Meridional Overturning Circulation (AMOC) reproduced by BESM-OA2.5 has the meridional overturning structure

comparable with the ensemble AMOC simulated by the CMIP5's models. BESM's maximum AMOC strength average value is slightly lower than the average value that has been observed by the project RAPID, but well within the range of mean square root variability that is observed. Although the averaged maximum strength AMOC simulated by the CMIP5 models is within the mean range square root variability that is observed, most models tend to simulate strong AMOC, with a maximum strength above 20 Sv, and out of the range (ZHANG; WANG, 2013, Figure7). The NAO atmospheric variability, which is well simulated by the CMIP5 models (NING; BRADLEY, 2016) is also very well simulated by BESM-OA2.5. In the extra-tropics, BESM-OA2.5 is capable to reproduce fairly well major variabilities in both Hemispheres, as the Pacific-North American (PNA), the Pacific-South American (PSA) and the Southern Annular Mode (SAM) teleconnections patterns, comparable to CMIP5 models that reproduce the PNA (NING; BRADLEY, 2016) and the SAM (ZHENG et al., 2013).

One of the main objectives of this thesis was to study the relationship of the AMM and oceanic and atmospheric large-scale variabilities at low-frequencies. The oceanic variabilities and the AMM has been less explored for this aim and here sea surface temperature (SST) and the ocean heat content up to 300 m (OHC300) decadal variabilities are analyzed. Through the spatial correlation map, it is possible to conclude that the AMM is highly correlated to SST variabilities in the North Atlantic (south of Greenland), therefore, the AMM is linked to the AMO. The lead-lag analysis shows that the AMO precedes the AMM by 2–3 months. This conclusion corroborates the findings of Vimont and Kossin (2007), which uses the same kind of analysis but different datasets and time period (1950-2005). Here, it is used a centennial period that span the whole 20th century (1900–2010), therefore reinforcing the robustness of the AMO link to the AMM. The analyses of the OHC is based on its capacity to sustain a persistent sea subsurface temperature that can impact the ocean surface in longer time scale (FRAJKA-WILLIAMS; BEAULIEU; DUCHEZ, 2017). Moreover, the OHC300 tend to have low-frequency variability in the North Atlantic (ZHANG, 2008; SEIDOV et al., 2017) and the source of such decadal variability is likely related to the northward upper layer of the AMOC (KNIGHT et al., 2005; ZHANG, 2008). Based on this body of scientific information, the first hypothesis addressed by this thesis is that, although AMO precedes the AMM, they are both

influenced by the same external forcing, which is the AMOC variability. The analysis shows that there is no evidence that the OHC300 precedes the AMM, although some regions over the North Atlantic show that both variabilities are linked at zero-lag, in particular, the south of Greenland region and eastern part of Atlantic mid-latitudes. In the former region the AMM leads the OHC300 variability by 5–6 months and in the latter there is a symmetric lead-lag pattern. Therefore, it is concluded that the OHC300 decadal variability does not influence the AMM dominant decadal variability.

Comparing with the ocean counterpart, atmospheric large-scale variabilities or climate variabilities that reach the tropical Atlantic through atmospheric teleconnections (like ENSO) have received more attention on the potential influence that these phenomena can exert on the AMM. On interannual time scale ENSO is regarded as an important influence of the tropical Atlantic and in the AMM. Nonetheless, at decadal time scale the results presented in this thesis show lack of relationship between the two modes. This corroborates previous reports that indicate that ENSO is mainly a source of interannual influence (NOBRE; ZEBIAK; KIRTMAN, 2003; XIE; CARTON, 2004). The Interdecadal Pacific Oscillation (IPO) is also evaluated since its ability to impose a decadal influence globally (HENLEY et al., 2015). The results given by the analysis of the relationship between IPO and AMM on decadal time scale shows clearly absent covariability. The ENSO and IPO absent link to the AMM on decadal time scale indicate that the Pacific region has not a significant influence on the AMM dominant low-frequency variability. These results enhance the interest on the North Atlantic Oscillation (NAO) as a potential influence on the AMM dominant decadal periodicity. Most of the studies that analyzed the relationship between NAO and tropical Atlantic or specifically with AMM, concluded that NAO generates the conditions to trigger the AMM formation (XIE; TANIMOTO, 1998; CZAJA; VAN DER VAART; MARSHALL, 2002; CHIANG; VIMONT, 2004; HUANG; SHUKLA, 2005; HANDOY et al., 2006; PENLAND; HARTTEN, 2014). However, some studies suggest lack of a clear NAO influence on the AMM (RUIZ-BARRADAS; CARTON; NIGAM, 2000; WAINER; SERVAIN; CLAUZET, 2008; DOI; TOZUKA; YAMAGATA, 2010). Based on statistical analysis as lead-lag correlation and lead-lag regression maps, it is shown that the NAO exerts a significant influence on the AMM both on interannual and decadal time scales. This result, despite lack of

originality, is important to enrich the body of knowledge about the AMM predictability and its link to the NAO. Therefore, the second hypothesis formulated, which is related to the effectiveness of the NAO as an external forcing of the AMM on decadal time scale, is demonstrated.

The third hypothesis formulated in this study investigates the changes that AMM may suffer in terms of its spatio-temporal variability under a perturbed climate scenario. Using the idealized abrupt 4xCO₂ experiment as the perturbed climate scenario, simulations of four-state-of-the-art Earth System Models are compared with the respective piControl experiment (the unperturbed experiment). The abrupt 4xCO₂ experiment is an extreme scenario and imposes rapid changes to several phenomena of the climate system. In this study, it is particularly interested in perturbed ocean circulation in the Atlantic Ocean basin. The response of the Atlantic Ocean circulation is inferred by the changes occurred in the AMOC simulated by each model. Comparing the maximum AMOC time series in latitude/depth coordinates of its piControl maximum, the models show a reduction ranging from 43% to 66%, and all of them reaches a stationary state roughly 90 years after the perturbation it is imposed. All the structure of the AMOC changes, with a significant southward displacement of the upper limb of the upper overturning cell, which includes the most important layers concerning to the northward transport of warmer and salty water to the North Atlantic. These scenarios are consistent with AMOC cold mode that occurred in the last glaciation period. Interestingly, the BESM-OA2.5 and the HadGEM2-ES, two models that in their respective piControl simulations represents very well the AMM spatio-temporal variability, in the 4xCO₂ simulations the AMM does not show any significant changes. Conversely, the CanESM2 model, which also simulates the AMM reasonably well, shows that the AMM is not the leading mode in a perturbed climate. Nonetheless, Trauth et al., (2003) infers through proxy-data that the AMM was likely active 30 kyr ago, in Last Maximum Glaciation, a period in which the AMOC had a cold structure. Therefore, the results presented by BESM-OA2.5 and HadGEM2-ES should be regarded with interest and suggest that the AMM is not significantly influenced by the Atlantic Ocean circulation. This is a hypothesis that corroborates with the results obtained to answer the first hypothesis addressed by this thesis, in which it is shown that the ocean heat content decadal variability does not influence the AMM. Therefore, as a conclusion, the results of first and third

hypothesis seem to indicate that the Atlantic Ocean circulation, at least through this sort of analysis, does not have a significant influence on the AMM variability. Nevertheless, it should be noted that the 4xCO₂ result simulations can be model dependent, so more research should be done in this direction.

In summary, the thesis contributed by showing that the AMO and AMM are two modes that covaried throughout the period 1900–2010, in which the AMO clearly precedes the AMM. Whether the AMO excites the AMM is not concluded. This work concludes that the ocean heat content (0–300 m) decadal variability in the Atlantic Ocean does not influence the AMM on decadal time scale. However, it is not ruled out its influence through the ocean pathway in other time scales. Additionally, the results presented indicate that major climate phenomena as ENSO and IPO do not have a significant influence on the AMM on decadal time scale. The relationship between the NAO and the AMM, which is regarded as significant by several studies but have been questioned by some studies, is revisited in the thesis. The results show clearly that the NAO exerts an external influence on the AMM, both in interannual and decadal time scales. Thus, most of the studies about this subject are corroborated by our findings. Moreover, the analyses allow speculating about the potential cooperation of the AMO and NAO in generating the conditions to trigger the AMM predominantly on decadal time scale. Therefore, this thesis leaves this question: is the AMM dominant decadal periodicity modulated by the NAO and AMO covariability? Certainly, more research should be carried out to address the complexity inherent to this kind of problem. Finally, this thesis contributed to show that the AMM is likely to be a robust climate mode that is active in extreme climate system scenarios, in which the Atlantic Ocean circulation has been profoundly reshaped. Future work should address this topic, and more models simulations are needed to further conclusions.

REFERENCES

- ADLER, R. F.; HUFFMAN, G. J.; CHANG, A.; FERRARO, R.; XIE, P.-P.; JANOWIAK, J.; RUDOLF, B.; SCHNEIDER, U.; CURTIS, S.; BOLVIN, D.; GRUBER, A.; SUSSKIND, J.; ARKIN, P.; NELKIN, E. The version-2 Global Precipitation Climatology Project (GPCP) monthly precipitation analysis (1979–Present). **Journal of Hydrometeorology**, v. 4, n. 6, p. 1147–1167, 2003.
- ALEXANDER, M.; SCOTT, J. The influence of ENSO on air-sea interaction in the Atlantic. **Geophysical Research Letters**, v. 29, n. 14, p. 46-1-46-4, jul. 2002.
- AMAYA, D. J.; DEFLORIO, M. J.; MILLER, A. J.; XIE, S. P. WES feedback and the Atlantic Meridional mode: observations and CMIP5 comparisons. **Climate Dynamics**, v. 49, n. 5, p. 1665–1679, 2017.
- AMAYA, D. J.; FOLTZ, G. R. Impacts of canonical and Modoki El Niño on tropical Atlantic SST. **Journal of Geophysical Research: Oceans**, v. 119, n. 2, p. 777–789, fev. 2014.
- ANNAN, J. D.; HARGREAVES, J. C. A perspective on model-data surface temperature comparison at the Last Glacial Maximum. **Quaternary Science Reviews**, v.107, p.1-10, 2015. Disponível em: <<https://www.sciencedirect.com/science/article/pii/S0277379114003679>>. Acesso em: 16 abr. 2018
- ANTHES, R. A. A cumulus parameterization scheme utilizing a one-dimensional cloud model. **Monthly Weather Review**, v. 105, n. 3, p. 270–286, mar. 1977.
- ARAKAWA, A.; SCHUBERT, W. H. Interaction of a cumulus cloud ensemble with the large-scale environment, Part I. **Journal of the Atmospheric Sciences**, v.31, p.674-701, 1974.
- BA, J.; KEENLYSIDE, N. S.; LATIF, M.; PARK, W.; DING, H.; LOHMANN, K.; MIGNOT, J.; MENARY, M.; OTTERÅ, O. H.; WOUTERS, B.; SALAS Y MELIA, D.; OKA, A.; BELLUCCI, A.; VOLODIN, E. A multi-model comparison of Atlantic multidecadal variability. **Climate Dynamics**, v. 43, n. 9–10, p. 2333–2348, 30 nov. 2014.
- BARREIRO, M.; CHANG, P.; JI, L.; SARAVANAN, R.; GIANNINI, A. Dynamical elements of predicting boreal spring tropical Atlantic sea-surface temperatures. **Dynamics of Atmospheres and Oceans**, v. 39, n. 1/2 , p. 61–85, 2005.
- BARREIRO, M.; CHANG, P.; SARAVANAN, R. Simulated precipitation response to SST forcing and potential predictability in the region of the South Atlantic convergence zone. **Climate Dynamics**, v. 24, n. 1, p. 105–114, 2005.
- BARREIRO, M.; GIANNINI, A.; CHANG, P.; SARAVANAN, R. On the role of the South Atlantic atmospheric circulation in Tropical Atlantic variability. **Earth's Climate**, p. 143–156, 2004.

- BOOTH, B. B. B.; DUNSTONE, N. J.; HALLORAN, P. R.; ANDREWS, T.; BELLOUIN, N. Aerosols implicated as a prime driver of twentieth-century North Atlantic climate variability. **Nature**, v. 484, n. 7393, p. 228–232, 4 abr. 2012.
- BELLENGER, H.; GUILYARDI, E.; LELOUP, J.; LENGAIGNE, M.; VIALARD, J. ENSO representation in climate models: From CMIP3 to CMIP5. **Climate Dynamics**, v. 42, n. 7–8, p. 1999–2018, 2014.
- BRETHERTON, C. S.; SMITH, C.; WALLACE, J. M.; BRETHERTON, C. S.; SMITH, C.; WALLACE, J. M. An intercomparison of methods for finding coupled patterns in climate data. **Journal of Climate**, v. 5, n. 6, p. 541–560, jun. 1992.
- BUCKLEY, M. W.; MARSHALL, J. Observations, inferences, and mechanisms of the Atlantic Meridional overturning circulation: a review Martha W. **Reviews of Geophysics**, v. 54, p. 5–63, 2015.
- CAI, Y.; LENTON, T. M.; LONTZEK, T. S. Risk of multiple interacting tipping points should encourage rapid CO₂ emission reduction. **Nature Climate Change**, v. 6, n. 5, p. 520–525, 2016.
- CARTON, J. A.; CAO, X.; GIESE, B. S.; DA SILVA, A. M. Decadal and interannual SST variability in the Tropical Atlantic Ocean. **Journal of Physical Oceanography**, v. 26, p. 1165–1175, 1996.
- CARVALHO, L. M. V.; JONES, C.; LIEBMANN, B. The South Atlantic convergence zone: Intensity, form, persistence, and relationships with intraseasonal to interannual activity and extreme rainfall. **Journal of Climate**, v. 17, n. 1, p. 88–108, 2004.
- CAYAN, D. R. Latent and sensible heat flux anomalies over the northern oceans: the connection to monthly atmospheric circulation. **Journal of Climate**, v. 5, n. 4, p. 354–369, 1992.
- CHANG, P.; FANG, Y.; SARAVANAN, R.; JI, L.; SEIDEL, H. The cause of the fragile relationship between the Pacific El Niño and the Atlantic Niño. **Nature**, v. 443, n. 7109, p. 324–328, 2006a.
- CHANG, P.; JI, L.; SARAVANAN, R. A hybrid coupled model study of Tropical Atlantic variability. **Journal of Climate**, v. 14, n. 3, p. 361–390, fev. 2001.
- CHANG, P.; KI, L.; LI, H. A decadal climate variation in the tropical Atlantic Ocean from thermodynamic air-sea interactions. **Nature**, v. 385, n. 6, p. 516–518, 1997.
- CHANG, P.; YAMAGATA, T.; SCHOPF, P.; BEHERA, S. K.; CARTON, J.; KESSLER, W. S.; MEYERS, G.; QU, T.; SCHOTT, F.; SHETYE, S.; XIE, S.-P. Climate fluctuations of tropical coupled systems: the role of ocean dynamics. **Journal of Climate**, v. 19, n. 20, p. 5122–5174, 2006b.
- CHANG, P.; YAMAGATA, T.; SCHOPF, P.; BEHERA, S. K.; CARTON, J.; KESSLER, W. S.; MEYERS, G.; QU, T.; SCHOTT, F.; SHETYE, S.; XIE, S.-P. Climate fluctuations of tropical coupled systems: the role of ocean dynamics. **Journal of Climate**, v. 19, n. 20, p. 5122–5174, out. 2006c.

- CHARNEY, J. G.; STONE, P. H.; QUIRK, W. J. Drought in the Sahara: a biogeophysical feedback mechanism. **Science**, New York, v. 186, n. 4163, p. 531–3, nov. 1975.
- CHAVES, R. R.; NOBRE, P. Interactions between sea surface temperature over the South Atlantic Ocean and the South Atlantic Convergence Zone. **Geophysical Research Letters**, v. 31, n. 3, p. 1–4, 2004.
- CHENG, W.; CHIANG, J. C. H.; ZHANG, D. Atlantic meridional overturning circulation (AMOC) in CMIP5 Models: RCP and historical simulations. **Journal of Climate**, v. 26, n. 18, p. 7187–7197, 9 set. 2013.
- CHIANG, J. C. H.; KUSHNIR, Y.; GIANNINI, A. Deconstructing Atlantic ITCZ variability: influence of the local cross-equatorial SST gradient, and remote forcing from the eastern equatorial Pacific 3. **Journal of Geophysical Research**, v. 107, n. 6214, p. 1–63, 2002.
- CHIANG, J. C. H.; LINTNER, B. R. Mechanisms of remote tropical surface warming during El Niño. **Journal of Climate**, v. 18, n. 20, p. 4130–4149, out. 2005.
- CHIANG, J. C. H.; SOBEL, A. H. Tropical tropospheric temperature variations caused by ENSO and their influence on the remote tropical climate. **Journal of Climate**, v. 15, n. 18, p. 2616–2631, 2002.
- CHIANG, J. C. H.; VIMONT, D. J. Analogous Pacific and Atlantic Meridional modes of tropical atmosphere – ocean variability. **Journal of Climate**, v. 17, n. 21, p. 4143–4158, 2004.
- CHOU, M.-D.; SUAREZ, M. J. **A solar radiation parameterization for atmospheric studies**. Washington: NASA, 1999. (NASA Technical Report 104606, . 15).
- CHYLEK, P.; LI, J.; DUBEY, M. K.; WANG, M.; LESINS, G. Observed and model simulated 20th century Arctic temperature variability: Canadian Earth System Model CanESM2. **Atmospheric Chemistry and Physics Discussions**, v. 11, n. 8, p. 22893–22907, 2011.
- CLEMENT, A.; BELLOMO, K.; MURPHY, L. N.; CANE, M. A.; MAURITSEN, T.; RADEL, G.; STEVENS, B. The Atlantic Multidecadal Oscillation without a role for ocean circulation. **Science**, v. 350, n. 6258, p. 320–324, 2015.
- COLLINS, W. J.; BELLOUIN, N.; DOUTRIAUX-BOUCHER, M.; GEDNEY, N.; HALLORAN, P.; HINTON, T.; HUGHES, J.; JONES, C. D.; JOSHI, M.; LIDDICOAT, S. Development and evaluation of an Earth-system model–HadGEM2. **Geoscientific Model Development**, v. 4, n. 4, p. 997–1062, 2011.

COMPO, G. P.; WHITAKER, J. S.; SARDESHMUKH, P. D.; MATSUI, N.; ALLAN, R. J.; YIN, X.; GLEASON, B. E.; VOSE, R. S.; RUTLEDGE, G.; BESSEMOULIN, P.; BRONNIMANN, S.; BRUNET, M.; CROUTHAMEL, R. I.; GRANT, A. N.; GROISMAN, P. Y.; JONES, P. D.; KRUK, M. C.; KRUGER, A. C.; MARSHALL, G. J.; MAUGERI, M.; MOK, H. Y.; NORDLI, O.; ROSS, T. F.; TRIGO, R. M.; WANG, X. L.; WOODRUFF, S. D.; WORLEY, S. J. The twentieth century reanalysis project. **Quarterly Journal of the Royal Meteorological Society**, v. 137, n. 654, p. 1–28, 2011.

COOK, E. R.; DARRIGO, R. D.; BRIFFA, K. R. A reconstruction of the North Atlantic Oscillation using tree-ring chronologies from North America and Europe. **The Holocene**, v. 8, n. 1, p. 9–17, 27 jan. 1998.

CZAJA, A. Why is North Tropical Atlantic SST variability stronger in Boreal spring? **Journal of Climate**, v. 17, n. 15, p. 3017–3025, 2004.

CZAJA, A.; VAN DER VAART, P.; MARSHALL, J. A Diagnostic study of the role of remote forcing in Tropical Atlantic variability. **Journal of Climate**, v. 15, n. 22, p. 3280–3290, 2002.

DE OLIVEIRA VIEIRA, S.; SATYAMURTY, P.; ANDREOLI, R. V. On the South Atlantic Convergence Zone affecting southern Amazonia in austral summer. **Atmospheric Science Letters**, v. 14, n. 1, p. 1–6, jan. 2013.

DELWORTH, T. L.; CLARK, P. U.; HOLLAND, M.; JOHNS, W. E.; KUHNBRODT, T.; LYNCH-STIEGLITZ, J.; MORRILL, C.; SEAGER, R.; WEAVER, A. J.; ZHANG, R. The potential for abrupt change in the Atlantic Meridional overturning circulation. In: U.S. CLIMATE CHANGE SCIENCE PROGRAM. **Abrupt climate change** Reston, VA: U.S. Geological Survey, 2008. p. 258–359.

DELWORTH, T. L.; MANN, M. E. Observed and simulated multidecadal variability in the Northern Hemisphere. **Climate Dynamics**, v. 16, n. 9, p. 661–676, 2000a.

DELWORTH, T. L.; MANN, M. E. Observed and simulated multidecadal variability in the Northern Hemisphere. **Climate Dynamics**, v. 16, n. 9, p. 661–676, 5 set. 2000b.

DELWORTH, T. L.; ZENG, F.; VECCHI, G. A.; YANG, X.; ZHANG, L.; ZHANG, R. The North Atlantic Oscillation as a driver of rapid climate change in the Northern Hemisphere. **Nature Geoscience**, v. 9, n. 7, p. 509–512, jun. 2016.

DELWORTH, T.; MANABE, S.; STOUFFER, R. J. Interdecadal variations of the thermohaline circulation in a coupled ocean-atmosphere model. **Journal of Climate**, v. 6, n. 11, p. 1993–2011, 1 nov. 1993.

DESER, C.; ALEXANDER, M. A.; XIE, S.-P.; PHILLIPS, A. S. Sea surface temperature variability: patterns and mechanisms. **Annual Review of Marine Science**, v. 2, n. 1, p. 115–143, jan. 2010.

DOI, T.; TOZUKA, T.; YAMAGATA, T. Interannual variability of the Guinea Dome and its possible link with the Atlantic Meridional Mode. **Climate Dynamics**, v. 33, n. 7–8, p. 985–998, 2009.

- DOI, T.; TOZUKA, T.; YAMAGATA, T. The Atlantic meridional mode and its coupled variability with the Guinea dome. **Journal of Climate**, v. 23, n. 2, p. 455–475, 2010.
- DOMMENGET, D.; LATIF, M. Interannual to decadal variability in the Tropical Atlantic. **Journal of Climate**, v. 13, n. 4, p. 777–792, 2000.
- DOMMENGET, D.; LATIF, M. A cautionary note on the interpretation of EOFs. **Journal of Climate**, v. 15, n. 2, p. 216–225, jan. 2002.
- DRIJFHOUT, S.; VAN OLDENBORGH, G. J.; CIMATORIBUS, A. Is a decline of AMOC causing the warming hole above the North Atlantic in observed and modeled warming patterns? **Journal of Climate**, v. 25, n. 24, p. 8373–8379, 19 dez. 2012.
- EMANUEL, K. Increasing destructiveness of tropical cyclones over the past 30 years. **Nature**, v. 436, n. 7051, p. 686–688, ago. 2005.
- ENFIELD, D. B.; MAYER, D. A. Tropical Atlantic sea surface temperature variability and its relation to El Niño–Southern Oscillation. **Journal of Geophysical Research: Oceans**, v. 102, n. C1, p. 929–945, jan. 1997.
- EVAN, A. T.; FOLTZ, G. R.; ZHANG, D. Physical response of the tropical–subtropical North Atlantic Ocean to decadal–multidecadal forcing by African dust. **Journal of Climate**, v. 25, n. 17, p. 5817–5829, 2012.
- EVAN, A. T.; FOLTZ, G. R.; ZHANG, D.; VIMONT, D. J. Influence of African dust on ocean–atmosphere variability in the tropical Atlantic. **Nature Geoscience**, v. 4, n. 11, p. 762–765, 2011.
- EVAN, A. T.; VIMONT, D. J.; HEIDINGER, A. K.; KOSSIN, J. P.; BENNARTZ, R. The role of aerosols in the evolution of tropical North Atlantic Ocean temperature anomalies. **Science**, v. 324, n. 5928, p. 778–781, 2009.
- FARNETI, R. Modelling interdecadal climate variability and the role of the ocean. **Wires Climate Change**, v.8, n.1, e441, jan. 2017.
- FARNETI, R.; VALLIS, G. K. Mechanisms of interdecadal climate variability and the role of ocean–atmosphere coupling. **Climate Dynamics**, v. 36, n. 1, p. 289–308, 14 jan. 2011.
- FELDSTEIN, S. B. The timescale, power spectra, and climate noise properties of teleconnection patterns. **Journal of Climate**, v. 13, n. 24, p. 4430–4440, 15 dez. 2000.
- FERRIER, B. S.; JIN, Y.; LIN, Y.; BLACK, T.; ROGERS, E.; DIMEGO, G. Implementation of a 527 new grid-scale cloud and precipitation scheme in the NCEP Eta model. In: CONFERENCE ON WEATHER ANALYSIS AND FORECASTING, 19., CONFERENCE ON NUMERICAL WEATHER PREDICTION, 15., 2002. **Proceedings...** AMS, 2002.

- FIGUEROA, S. N.; BONATTI, J. P.; KUBOTA, P. Y.; GRELL, G. A.; MORRISON, H.; BARROS, S. R. M.; FERNANDEZ, J. P. R.; RAMIREZ, E.; CAPISTRANO, V. B.; ALVIM, D. S.; ENORÉ, D. P.; DINIZ, F. L. R.; BARBOSA, H. M. J.; MENDES, C. L.; PANETTA, J. The Brazilian Global Atmospheric Model (BAM): performance for tropical rainfall forecasting and sensitivity to convective scheme and horizontal resolution. **Weather and Forecasting**, v. 31, n. 5, p. 1547–1572, out. 2016.
- FLATO, G.; MAROTZKE, J.; ABIODUN, B.; BRACONNOT, P.; CHOU, S. C.; COLLINS, W.; COX, P.; DRIOUECH, F.; EMORI, S.; EYRING, V.; FOREST, C.; GLECKLER, P.; GUILYARDI, E.; JAKOB, C.; KATTSOV, V.; REASON, C.; RUMMUKAINEN, M. Evaluation of climate models. In: STOCKER, T. F.; QUIN, G.K; PLATTNER, M.; TIGNOR, S.K.; ALLEN, J. BOSCHUNG, A.; NAUELS, Y.; XIA, Y.; BEX, V.; MIDGLEY, P. M. (Eds.). **Climate change 2013: the physical science basis**. Cambridge: Cambridge University Press, 2013. p. 741–866.
- FOLLAND, C. K. Relative influences of the Interdecadal Pacific Oscillation and ENSO on the South Pacific Convergence Zone. **Geophysical Research Letters**, v. 29, n. 13, p. 2–5, 1 jul. 2002.
- FOLLAND, C.; PALMER, T.; PARKER, D. Sahel rainfall and worldwide sea temperatures 1901-85. **Nature**, v. 319, n. 30, p. 402–403, 1986.
- FOLTZ, G. R.; MCPHADEN, M. J. The role of oceanic heat advection in the evolution of tropical North and South Atlantic SST anomalies. **Journal of Climate**, v. 19, n. 23, p. 6122–6138, 2006.
- FOLTZ, G. R.; MCPHADEN, M. J. Trends in Saharan dust and tropical Atlantic climate during 1980-2006. **Geophysical Research Letters**, v. 35, n. 20, p. 1–5, 2008a.
- FOLTZ, G. R.; MCPHADEN, M. J. Impact of Saharan dust on tropical North Atlantic SST. **Journal of Climate**, v. 21, n. 19, p. 5048–5060, 2008b.
- FOLTZ, G. R.; MCPHADEN, M. J. Interaction between the Atlantic meridional and Niño modes. **Geophysical Research Letters**, v. 37, n. 18, L18064, 22 set. 2010.
- FOLTZ, G. R.; MCPHADEN, M. J.; LUMPKIN, R. A strong Atlantic Meridional mode event in 2009: the role of mixed layer dynamics*. **Journal of Climate**, v. 25, n. 1, p. 363–380, jan. 2012.
- FRAJKA-WILLIAMS, E.; BEAULIEU, C.; DUCHEZ, A. Emerging negative Atlantic Multidecadal Oscillation index in spite of warm subtropics. **Scientific Reports**, v. 7, n. 1, p. 1–8, 2017.
- GASTINEAU, G.; D’ANDREA, F.; FRANKIGNOUL, C. Atmospheric response to the North Atlantic Ocean variability on seasonal to decadal time scales. **Climate Dynamics**, v. 40, n. 9–10, p. 2311–2330, 2013.
- GASTINEAU, G.; FRANKIGNOUL, C. Influence of the North Atlantic SST variability on the atmospheric circulation during the twentieth century. **Journal of Climate**, v. 28, n. 4, p. 1396–1416, 2015.
- GERSHUNOV, A; BARNETT, T. Interdecadal modulation of ENSO teleconnections. **Bulletin of the American Meteorological Society**, v. 79, n. 12, p. 2715–2726, 1998.

- GIANNINI, A.; BIASUTTI, M.; VERSTRAETE, M. M. A climate model-based review of drought in the Sahel: desertification, the re-greening and climate change. **Global and Planetary Change**, v. 64, n. 3–4, p. 119–128, 2008.
- GIANNINI, A.; KUSHNIR, Y.; CANE, M. A. Interannual variability of Caribbean rainfall, ENSO, and the Atlantic Ocean. **Journal of Climate**, v. 13, n. 2, p. 297–311, jan. 2000.
- GIANNINI, A.; SARAVANAN, R.; CHANG, P. Oceanic forcing of Sahel rainfall on interannual to interdecadal time scales. **Science**, v. 302, n. 5647, p. 1027–1030, fev. 2003.
- GIAROLLA, E.; SIQUEIRA, L. S. P.; BOTTINO, M. J.; MALAGUTTI, M.; CAPISTRANO, V. B.; NOBRE, P. Equatorial Atlantic Ocean dynamics in a coupled ocean-atmosphere model simulation. **Ocean Dynamics**, v. 65, n. 6, p. 831–843, jun. 2015.
- GIERZ, P.; LOHMANN, G.; WEI, W. Response of Atlantic overturning to future warming in a coupled atmosphere-ocean-ice sheet model. **Geophysical Research Letters**, v. 42, n. 16, p. 6811–6818, 28 ago. 2015.
- GIORGETTA, M. A.; JUNGCLAUS, J.; REICK, C. H.; LEGUTKE, S.; BADER, J.; BÖTTINGER, M.; BROVKIN, V.; CRUEGER, T.; ESCH, M.; FIEG, K.; GLUSHAK, K.; GAYLER, V.; HAAK, H.; HOLLWEG, H.-D.; ILYINA, T.; KINNE, S.; KORNBLUEH, L.; MATEI, D.; MAURITSEN, T.; MIKOLAJEWICZ, U.; MUELLER, W.; NOTZ, D.; PITHAN, F.; RADDATZ, T.; RAST, S.; REDLER, R.; ROECKNER, E.; SCHMIDT, H.; SCHNUR, R.; SEGSCHNEIDER, J.; SIX, K. D.; STOCKHAUSE, M.; TIMMRECK, C.; WEGNER, J.; WIDMANN, H.; WIENERS, K.-H.; CLAUSSEN, M.; MAROTZKE, J.; STEVENS, B. Climate and carbon cycle changes from 1850 to 2100 in MPI-ESM simulations for the Coupled Model Intercomparison Project phase 5. **Journal of Advances in Modeling Earth Systems**, v. 5, n. 3, p. 572–597, jul. 2013.
- GOLDENBERG, S. B.; LANDSEA, C. W.; MESTAS-NUÑEZ, A. M.; GRAY, W. M. The recent increase in Atlantic hurricane activity: causes and implications. **Science**, v. 293, n. 5529, p. 474–479, 20 jul. 2001.
- GONG, D.; WANG, S. Definition of Antarctic oscillation index. **Geophysical Research Letters**, v. 26, n. 4, p. 459–462, 1999.
- GRELL, GEORG AND DÉVÉNYI, D. A. A generalized approach to parameterizing convection combining ensemble and data assimilation techniques. **Geophysical Research Letters**, v. 29, n. 14, p. 10–13, jul. 2002.
- GRIFFIES, S. M. **Elements of MOM4p1**. Silver Spring: NOAA, 2009.
- GRIMM, A. M. The El Niño impact on the summer monsoon in Brazil: regional processes versus remote influences. **Journal of Climate**, v. 16, n. 2, p. 263–280, jan. 2003.
- GUAN, B.; NIGAM, S. Analysis of atlantic SST variability factoring interbasin links and the secular trend: Clarified structure of the Atlantic multidecadal oscillation. **Journal of Climate**, v. 22, n. 15, p. 4228–4240, 1 ago. 2009.

- GULEV, S. K.; LATIF, M.; KEENLYSIDE, N.; PARK, W.; KOLTERMANN, K. P. North Atlantic Ocean control on surface heat flux on multidecadal timescales. **Nature**, v. 499, n. 7459, p. 464–467, 25 jul. 2013.
- HAARSMA, R. J.; CAMPOS, E.; HAZELEGER, W.; SEVERIJNS, C. Influence of the meridional overturning circulation on tropical atlantic climate and variability. **Journal of Climate**, v. 21, n. 6, p. 1403–1416, 2008.
- HAM, Y. G.; KUG, J. S.; PARK, J. Y. Two distinct roles of Atlantic SSTs in ENSO variability: North Tropical Atlantic SST and Atlantic Niño. **Geophysical Research Letters**, v. 40, n. 15, p. 4012–4017, 2013.
- HANDOH, I. C.; MATTHEWS, A. J.; BIGG, G. R.; STEVENS, D. P. Interannual variability of the tropical Atlantic independent of and associated with ENSO: part I. the North Tropical Atlantic. **International Journal of Climatology**, v. 26, n. 14, p. 1937–1956, nov. 2006.
- HANNACHI, A.; JOLLIFFE, I. T.; STEPHENSON, D. B. Empirical orthogonal functions and related techniques in atmospheric science: a review. **International Journal of Climatology**, v.27, n.9, p.1119-1152, jul. 2007.
- HARSHVARDHAN; DAVIES, R.; RANDALL, D. A.; CORSETTI, T. G. A fast radiation parameterization for atmospheric circulation models. **Journal of Geophysical Research**, v. 92, n. D1, p. 1009–1016, 1987.
- HASANEAN, H. M. Variability of the North Atlantic subtropical high and associations with tropical sea-surface temperature. **International Journal of Climatology**, v. 24, n. 8, p. 945–957, 30 jun. 2004.
- HASTENRATH, S. Decadal-scale changes of the circulation in the tropical atlantic sector associated with Sahel drought. **International Journal of Climatology**, v. 10, n. 5, p. 459–472, jul. 1990.
- HASTENRATH, S. Exploring the climate problems of Brazil's Nordeste: a review. **Climatic Change**, v. 112, n. 2, p. 243–251, maio 2012.
- HASTENRATH, S.; HELLER, L. Dynamics of climatic hazards in northeast Brazil. **Quarterly Journal of the Royal Meteorological Society**, v. 103, n. 435, p. 77–92, jan. 1977.
- HASTENRATH, S.; POLZIN, D. Long-term variations of circulation in the tropical Atlantic sector and Sahel rainfall. **International Journal of Climatology**, v. 31, n. 5, p. 649–655, 2011.
- HASTENRATH, S.; POLZIN, D. Variability of circulation and Sahel rainfall in the twentieth century. **International Journal of Climatology**, v. 34, n. 5, p. 1693–1698, 2014.
- HAZELEGER, W.; WOUTERS, B.; VAN OLDENBORGH, G. J.; CORTI, S.; PALMER, T.; SMITH, D.; DUNSTONE, N.; KRÖGER, J.; POHLMANN, H.; VON STORCH, J. S. Predicting multiyear North Atlantic Ocean variability. **Journal of Geophysical Research: Oceans**, v. 118, n. 3, p. 1087–1098, 2013.

- HENLEY, B. J.; GERGIS, J.; KAROLY, D. J.; POWER, S.; KENNEDY, J.; FOLLAND, C. K. A tripole index for the interdecadal Pacific Oscillation. **Climate Dynamics**, v. 45, n. 11–12, p. 3077–3090, 5 dez. 2015.
- HOERLING, M.; HURRELL, J.; EISCHEID, J.; PHILLIPS, A. Detection and attribution of twentieth-century northern and southern African rainfall change. **Journal of Climate**, v. 19, n. 16, p. 3989–4008, 2006.
- HOUGHTON, R. W.; TOURRE, Y. M. Characteristics of low-frequency sea surface temperature fluctuations in the Tropical Atlantic. **Journal of Climate**, v. 5, n. 7, p. 765–772, jul. 1992.
- HU, Z. Z.; HUANG, B. Physical processes associated with the tropical Atlantic SST gradient during the anomalous evolution in the Southeastern Ocean. **Journal of Climate**, v. 20, n. 14, p. 3366–3378, 2006.
- HU, Z. Z.; HUANG, B. Interferential impact of ENSO and PDO on dry and wet conditions in the U.S. great plains. **Journal of Climate**, v. 22, n. 22, p. 6047–6065, nov. 2009.
- HUANG, B. Remotely forced variability in the tropical Atlantic Ocean. **Climate Dynamics**, v. 23, n. 2, p. 133–152, 20 jul. 2004.
- HUANG, B.; BANZON, V. F.; FREEMAN, E.; LAWREMORE, J.; LIU, W.; PETERSON, T. C.; SMITH, T. M.; THORNE, P. W.; WOODRUFF, S. D.; ZHANG, H. M. Extended reconstructed sea surface temperature version 4 (ERSST.v4). part I: upgrades and intercomparisons. **Journal of Climate**, v. 28, n. 3, p. 911–930, fev. 2015.
- HUANG, B.; SCHOPF, P. S.; PAN, Z. The ENSO effect on the tropical Atlantic variability: a regionally coupled model study. **Geophysical Research Letters**, v. 29, n. 21, p. 2039, 2002.
- HUANG, B.; SHUKLA, J. Ocean – atmosphere interactions in the Tropical and Subtropical Atlantic Ocean. **Journal of Climate**, v. 18, n. 2004, p. 1652–1672, 2005.
- HUANG, H. P.; ROBERTSON, A. W.; KUSHNIR, Y. Atlantic SST gradient and the influence of ENSO. **Geophysical Research Letters**, v. 32, n. 20, p. 1–4, 2005.
- HUFFMAN, G. J.; ADLER, R. F.; BOLVIN, D. T.; GU, G. Improving the global precipitation record: GPCP version 2.1. **Geophysical Research Letters**, v. 36, n. 17, p. L17808, set. 2009.
- HURRELL, J. **The climate data guide: hurrell North Atlantic Oscillation (NAO) index (station-based)**. Disponível em: <https://climatedataguide.ucar.edu/climate-data/hurrell-north-atlantic-oscillation-nao-index-station-based>.
- HURRELL, J. W.; DESER, C. North Atlantic climate variability: the role of the North Atlantic cscillation. **Journal of Marine Systems**, , v.78, n.1, p.28-41, 2010.
Disponível em:
<<https://www.sciencedirect.com/science/article/pii/S0924796309003224>>. Acesso em: 21 abr. 2018

- HURRELL, J. W.; KUSHNIR, Y.; OTTERSEN, G.; VISBECK, M.; OTTERSON, G.; VISBECK, M. An overview of the North Atlantic oscillation. **The North Atlantic Oscillation: Climatic Significance and Environmental Impact**, v. 134, p. 263, 2003.
- HURRELL, J. W.; LOON, H. VAN. Decadal variations in climate associated with the North Atlantic Oscillation. **Climatic Change at High Elevation Sites**, v. 36, n. 3/4, p. 301–326, 1997.
- IVERSEN, T.; BENTSEN, M.; BETHKE, I.; DEBERNARD, J. B.; KIRKEVÅG, A.; SELAND, Ø.; DRANGE, H.; KRISTJÁNSSON, J. E.; MEDHAUG, I.; SAND, M.; SEIERSTAD, I. A. The Norwegian Earth System Model, NorESM1-M – part 2: climate response and scenario projections. **Geoscientific Model Development Discussions**, v. 6, n. 2, p. 389–415, 22 mar. 2013.
- JIMÉNEZ, P. A.; DUDHIA, J.; GONZÁLEZ-ROUCO, J. F.; NAVARRO, J.; MONTÁVEZ, J. P.; GARCÍA-BUSTAMANTE, E. A Revised Scheme for the WRF Surface Layer Formulation. **Monthly Weather Review**, v. 140, n. 3, p. 898–918, mar. 2012.
- JONES, C.; CARVALHO, L. M. V. Active and break phases in the South American monsoon system. **Journal of Climate**, v. 15, n. 8, p. 905–914, 2002.
- JOYCE, T. M.; FRANKIGNOUL, C.; YANG, J.; PHILLIPS, H. E. Ocean response and feedback to the SST dipole in the Tropical Atlantic. **Journal of Physical Oceanography**, v. 34, n. 11, p. 2525–2540, 2004.
- KAROLY, D. J. Southern hemisphere circulation features associated with El-Nino-Southern oscillation events. **Journal of Climate**, v. 2, p. 1239–1252, 1989.
- KIDSON, J. W. Interannual variations in the Southern Hemisphere Circulation. **Journal of Climate**, v. 1, n. 12, p. 939–953, 1988.
- KIDSTON, J.; SCAIFE, A. A.; HARDIMAN, S. C.; MITCHELL, D. M.; BUTCHART, N.; BALDWIN, M. P.; GRAY, L. J. Stratospheric influence on tropospheric jet streams, storm tracks and surface weather. **Nature Geoscience**, v. 8, n. 6, p. 433–440, 18 jun. 2015.
- KIM, S. T.; JIN, F. F. An ENSO stability analysis. Part II: Results from the twentieth and twenty-first century simulations of the CMIP3 models. **Climate Dynamics**, v. 36, n. 7, p. 1609–1627, 2011.
- KLEIN, S. A.; SODEN, B. J.; LAU, N.-C. Remote sea surface temperature variations during ENSO: evidence for a Tropical Atmospheric bridge. **Journal of Climate**, v. 12, n. 4, p. 917–932, abr. 1999.
- KNIGHT, J. R.; ALLAN, R. J.; FOLLAND, C. K.; VELLINGA, M.; MANN, M. E. A signature of persistent natural thermohaline circulation cycles in observed climate. **Geophysical Research Letters**, v. 32, n. 20, p. 1–4, 1 out. 2005.
- KOSSIN, J. P.; VIMONT, D. J. A more general framework for understanding atlantic hurricane variability and trends. **Bulletin of the American Meteorological Society**, v. 88, n. 11, p. 1767–1781, 2007.

- KRISHNAMURTHY, L.; KRISHNAMURTHY, V. Indian monsoon 's relation with the decadal part of PDO in observations and NCAR CCSM4. **International Journal of Climatology**, jul. 2016.
- KUCHARSKI, F.; BRACCO, A.; YOO, J. H.; MOLTENI, F. Atlantic forced component of the Indian monsoon interannual variability. **Geophysical Research Letters**, v. 35, n. 4, p. L04706, fev. 2008.
- KUSHNIR, Y.; SEAGER, R.; MILLER, J.; CHIANG, J. C. H. A simple coupled model of tropical Atlantic decadal climate variability. **Geophysical Research Letters**, v. 29, n. 23, p. 4814–4818, dez. 2002.
- LAMB, P. J. Large-scale Tropical Atlantic surface circulation patterns associated with Subsaharan weather anomalies. **Tellus**, v. 30, n. 3, p. 240–251, jun. 1978.
- LARGE, W. G.; YEAGER, S. G. The global climatology of an interannually varying air - sea flux data set. **Climate Dynamics**, v. 33, n. 2–3, p. 341–364, ago. 2009.
- LATIF MOJIB, M.; KEENLYSIDE, N. S. A perspective on decadal climate variability and predictability. **Deep-Sea Research Part II: Topical Studies in Oceanography**, v. 58, n. 17–18, p. 1880–1894, 1 set. 2011.
- LEATHERS, D. J.; YARNAL, B.; PALECKI, M. A.; LEATHERS, D. J.; YARNAL, B.; PALECKI, M. A. The Pacific/North american teleconnection pattern and United States Climate. part I: regional temperature and precipitation associations. **Journal of Climate**, v. 4, n. 5, p. 517–528, maio 1991.
- LEE, S.-K.; ENFIELD, D. B.; WANG, C. Why do some El Ninos have no impact on tropical North Atlantic SST? **Geophysical Research Letters**, v. 35, n. 16, p. 1968–1969, 2008.
- LEE, S.-K.; WANG, C. Tropical Atlantic decadal oscillation and its potential impact on the Equatorial Atmosphere–Ocean dynamics: a simple model study. **Journal of Physical Oceanography**, v. 38, n. 1, p. 193–212, jan. 2008.
- LENTON, T. M. Early warning of climate tipping points. **Nature Climate Change**, v. 1, n. 4, p. 201–209, 2011.
- LENTON, T. M.; HELD, H.; KRIEGLER, E.; HALL, J. W.; LUCHT, W.; RAHMSTORF, S.; SCHELLNHUBER, H. J. Tipping elements in the Earth System. **Proceedings of the National Academy of Sciences**, v. 105, n. 49, p. 1786–1793, 2008.
- LEVITUS, S. **Climatological atlas of the world ocean**. Silver Spring: NOAA , 2009. 173p.
- LEVITUS, S.; BURGETT, R.; BOYER, T. **World ocean atlas: Salinity**. Silver Spring: NOAA, 1994. V.3.
- LI, J.; SUN, C.; JIN, F. F. NAO implicated as a predictor of Northern Hemisphere mean temperature multidecadal variability. **Geophysical Research Letters**, v. 40, n. 20, p. 5497–5502, out. 2013.

LINDZEN, R. S.; NIGAM, S. On the role of sea surface temperature gradients in forcing low-level winds and convergence in the tropics. **Journal of the Atmospheric Sciences**, v. 44, n. 17, p. 2418–2436, set. 1987.

LIU, Z. Dynamics of interdecadal climate variability: a historical perspective. **Journal of Climate**, v. 25, n. 6, p. 1963–1995, 2012.

LIU, Z.; ZHANG, Q.; WU, L. Remote impact on Tropical Atlantic climate variability: statistical assessment and dynamic assessment*. **Journal of Climate**, v. 17, n. 7, p. 1529–1549, abr. 2004.

LOZIER, M. S. Overturning in the North Atlantic. **Annual Review of Marine Science**, v. 4, n. 1, p. 291–315, 2012.

LUMPKIN, R.; SPEER, K. Global ocean meridional overturning. **Journal of Physical Oceanography**, v. 37, n. 10, p. 2550–2562, 2007.

LYNCH-STIEGLITZ, J. The Atlantic Meridional overturning circulation and abrupt climate change. **Annual Review of Marine Science**, v. 9, n. 1, p. 83–104, 2017.

MAHAJAN, S.; SARAVANAN, R.; CHANG, P. The role of the wind-evaporation-sea surface temperature (WES) feedback in air-sea coupled tropical variability. **Atmospheric Research**, v. 94, n. 1, p. 19–36, set. 2009.

MAHAJAN, S.; SARAVANAN, R.; CHANG, P. Free and forced variability of the Tropical Atlantic Ocean: role of the wind–evaporation–sea surface temperature feedback. **Journal of Climate**, v. 23, n. 22, p. 5958–5977, nov. 2010.

MAHAJAN, S.; SARAVANAN, R.; CHANG, P. The role of the wind-evaporation-sea surface temperature (WES) feedback as a thermodynamic pathway for the equatorward propagation of high-latitude sea ice-induced cold anomalies. **Journal of Climate**, v. 24, n. 5, p. 1350–1361, 2011.

MANTUA, N. J.; HARE, S. R.; ZHANG, Y.; WALLACE, J. M.; FRANCIS, R. C. A Pacific interdecadal climate oscillation with impacts on salmon production. **Bulletin of the American Meteorological Society**, v. 78, n. 6, p. 1069–1079, jun. 1997.

MARENGO, J. A.; CALVALCANTI, I. F. A.; SATYAMURTY, P.; TROSNIKOV, I.; NOBRE, C. A.; BONATTI, J. P.; CAMARGO, H.; SAMPAIO, G.; SANCHES, M. B.; MANZI, A. O.; CASTRO, C. A. C.; D'ALMEIDA, C.; PEZZI, L. P.; CANDIDO, L. Assessment of regional seasonal rainfall predictability using the CPTEC/COLA atmospheric GCM. **Climate Dynamics**, v. 21, n. 5–6, p. 459–475, nov. 2003.

MARINI, C.; FRANKIGNOUL, C. An attempt to deconstruct the Atlantic Multidecadal Oscillation. **Climate Dynamics**, v. 43, n. 3–4, p. 607–625, 25 ago. 2014.

MARSHALL, J.; JOHNSON, H.; GOODMAN, J. A Study of the Interaction of the North Atlantic Oscillation with Ocean Circulation. **Journal of Climate**, v. 14, n. 7, p. 1399–1421, 1 abr. 2001.

MARTINEZ-VILLALOBOS, C.; VIMONT, D. J. The role of the mean state in meridional mode structure and growth. **Journal of Climate**, v. 29, n. 10, p. 3907–3921, 2016.

- MASINA, S.; DI PIETRO, P.; STORTO, A.; NAVARRA, A. Global ocean re-analyses for climate applications. **Dynamics of Atmospheres and Oceans**, v. 52, n. 1–2, p. 341–366, 1 set. 2011.
- MCCARTHY, G. D.; SMEED, D. A.; JOHNS, W. E.; FRAJKA-WILLIAMS, E.; MOAT, B. I.; RAYNER, D.; BARINGER, M. O.; MEINEN, C. S.; COLLINS, J.; BRYDEN, H. L. Measuring the Atlantic Meridional overturning circulation at 26°N. **Progress in Oceanography**, v. 130, p. 91–111, 2015.
- MCPHADEN, M. J.; ZEBIAK, S. E.; GLANTZ, M. H. ENSO as an integrating concept in earth science. **Science**, New York, v. 314, n. 5806, p. 1740–1745, 2006.
- MEHTA, V. M. Variability of the Tropical Ocean surface temperatures at decadal–multidecadal timescales. part I: the Atlantic Ocean. **Journal of Climate**, v. 11, n. 9, p. 2351–2375, set. 1998.
- MÉLICE, J.-L. J.-L.; SERVAIN, J. The tropical Atlantic meridional SST gradient index and its relationships with the SOI, NAO and Southern Ocean. **Climate Dynamics**, v. 20, n. 5, p. 447–464, 2003.
- MELLOR, G. L.; YAMADA, T. Development of a turbulence closure model for geophysical fluid problems. **Reviews of Geophysics**, v.20, n.4, p.851-875, 1982.
- MIKOLAJEWICZ, U.; VIZCAÍNO, M.; JUNGCLAUS, J.; SCHURGERS, G. Effect of ice sheet interactions in anthropogenic climate change simulations. **Geophysical Research Letters**, v. 34, n. 18, p. 1–5, 2007.
- MO, K. C.; PEAGLE, J. N. The Pacific-South American modes and their downstream effects. **International Journal of Climatology**, v. 21, n. 21, p. 1211–1229, 2001.
- MOHINO, E.; JANICOT, S.; BADER, J. Sahel rainfall and decadal to multi-decadal sea surface temperature variability. **Climate Dynamics**, v. 37, n. 3, p. 419–440, 2011.
- MOURA, A. D.; SHUKLA, J. On the dynamics of droughts in northeast Brazil: observations, theory and numerical experiments with a General Circulation Model. **Journal of the Atmospheric Sciences**, v. 38, n. 12, p. 2653–2675, dez. 1981.
- NAMIAS, J. Influence of northern hemisphere general circulation on drought in northeast Brazil. **Tellus**, v. 4, n. 4, p. 336–343, ago. 1972.
- NAVARRA, A.; SIMONCINI, V. **A guide to empirical orthogonal functions for climate data analysis**. Berlin: Springer, 2010. 151 p. ISBN(978-90-481-3701-5).
- NEWMAN, M.; ALEXANDER, M. A.; AULT, T. R.; COBB, K. M.; DESER, C.; DI LORENZO, E.; MANTUA, N. J.; MILLER, A. J.; MINOBE, S.; NAKAMURA, H.; SCHNEIDER, N.; VIMONT, D. J.; PHILLIPS, A. S.; SCOTT, J. D.; SMITH, C. A. The Pacific decadal oscillation, revisited. **Journal of Climate**, v. 29, n. 12, p. 4399–4427, 2016.
- NICHOLSON, S. E. The West African Sahel: a review of recent studies on the rainfall regime and its interannual variability. **ISRN Meteorology**, v. 2013, p. 1–32, 2013.

- NING, L.; BRADLEY, R. S. NAO and PNA influences on winter temperature and precipitation over the eastern United States in CMIP5 GCMs. **Climate Dynamics**, v. 46, n. 3–4, p. 1257–1276, fev. 2016.
- NOBRE, P.; DE ALMEIDA, R. A.; MALAGUTTI, M.; GIAROLLA, E. Coupled ocean-atmosphere variations over the South Atlantic Ocean. **Journal of Climate**, v. 25, n. 18, p. 6349–6358, 2012.
- NOBRE, P.; MARENGO, J.; CAVALCANTE, L.; OBREGON, G.; BARROS, V.; CAMILLONI, I.; CAMPOS, N.; FERREIRA, A. Seasonal-to-decadal predictability and prediction of South American climate. **Journal of Climatology**, p. 1–13, 2006.
- NOBRE, P.; SHUKLA, J. Variation of sea surface temperature, wind stress, and rainfall over the Tropical Atlantic and South America. **Journal of Climate**, v. 9, p. 2464–2479, 1996.
- NOBRE, P.; SIQUEIRA, L. S. P.; DE ALMEIDA, R. A. F.; MALAGUTTI, M.; GIAROLLA, E.; CASTELÃO, G. P.; BOTTINO, M. J.; KUBOTA, P.; FIGUEROA, S. N.; COSTA, M. C.; BAPTISTA, M.; IRBER, L.; MARCONDES, G. G. Climate simulation and change in the Brazilian climate model. **Journal of Climate**, v. 26, n. 17, p. 6716–6732, 2013.
- NOBRE, P.; ZEBIAK, S. E.; KIRTMAN, B. P. Local and remote sources of tropical Atlantic variability as inferred from the results of a hybrid ocean-atmosphere coupled model. **Geophysical Research Letters**, v. 30, n. 5, p. 10–13, 2003.
- NOGUÉS-PAEGLE, J.; MO, K. C. Alternating wet and dry conditions over South America during summer. **Monthly Weather Review**, v. 125, p. 279–291, 1997.
- OBUKHOV, A. M. Turbulence in an atmosphere with a non-uniform temperature. **Boundary-Layer Meteorology**, v. 2, n. 1, p. 7–29, 1971.
- OKUMURA, Y.; XIE, S.-P.; NUMAGUTI, A.; TANIMOTO, Y. Tropical Atlantic air-sea interaction and its influence on the NAO. **Geophysical Research Letters**, v. 28, n. 8, p. 1507–1510, 15 abr. 2001.
- OLSEN, J.; ANDERSON, N. J.; KNUDSEN, M. F. Variability of the North Atlantic oscillation over the past 5,200 years. **Nature Geoscience**, v. 5, n. 11, p. 808–812, 23 nov. 2012.
- PALMER, T. N. Influence of the Atlantic, Pacific and Indian Oceans on Sahel rainfall. **Nature**, v. 322, n. 6076, p. 251–253, 1986.
- PATRICOLA, C. M.; SARAVANAN, R.; CHANG, P. The impact of the El Niño–Southern Oscillation and Atlantic meridional mode on seasonal Atlantic tropical cyclone activity. **Journal of Climate**, v. 27, n. 14, p. 5311–5328, 2014.
- PENLAND, C.; HARTTEN, L. M. Stochastic forcing of north tropical Atlantic sea surface temperatures by the North Atlantic Oscillation. **Geophysical Research Letters**, v. 41, n. 6, p. 2126–2132, 28 mar. 2014.
- POLZIN, D.; HASTENRATH, S. Climate of Brazil's nordeste and tropical Atlantic sector: preferred time scales of variability. **Revista Brasileira de Meteorologia**, v. 29, n. 2, p. 153–160, jun. 2014.

- POTTAPINJARA, V.; GIRISHKUMAR, M. S.; SIVAREDDY, S.; RAVICHANDRAN, M.; MURTUGUDDE, R. Relation between the upper ocean heat content in the equatorial Atlantic during boreal spring and the Indian monsoon rainfall during June–September. **International Journal of Climatology**, v. 36, n. 6, p. 2469–2480, maio 2016.
- POWER, S.; CASEY, T.; FOLLAND, C.; COLMAN, A.; MEHTA, V. Inter-decadal modulation of the impact of ENSO on Australia. **Climate Dynamics**, v. 15, n. 5, p. 319–324, 4 maio 1999.
- PYPER, B. J.; PETERMAN, R. M. Comparison of methods to account for autocorrelation in correlation analyses of fish data. **Canadian Journal of Fisheries and Aquatic Sciences**, v. 55, n. 9, p. 2127–2140, 1998.
- RAHMSTORF, S. Ocean circulation and climate during the past 120,000 years. **Nature**, v. 419, p. 207–214, 2002.
- RAHMSTORF, S.; BOX, J. E.; FEULNER, G.; MANN, M. E.; ROBINSON, A.; RUTHERFORD, S.; SCHAFFERNICHT, E. J. Exceptional twentieth-century slowdown in Atlantic Ocean overturning circulation. **Nature Climate Change**, v. 5, n. 5, p. 475–480, 23 maio 2015.
- RAJAGOPALAN, B.; KUSHNIR, Y.; TOURRE, Y. M. Observed decadal midlatitudes and tropical Atlantic climate variability. **Geophysical Research Letters**, v. 25, n. 21, p. 3967–3970, 1998.
- ROBERTSON, A.; MECHOSO, C. Interannual and interdecadal variability of the South Atlantic Convergence Zone. **Monthly weather review**, v. 128, n. 8, p. 2947–2957, ago. 2000.
- ROBSON, J.; ORTEGA, P.; SUTTON, R. A reversal of climatic trends in the North Atlantic since 2005. **Nature Geoscience**, v. 9, n. 7, p. 513–517, 2016.
- RODRIGUES, R. R.; HAARSMA, R. J.; CAMPOS, E. J. D.; AMBRIZZI, T. The impacts of inter-El Niño variability on the tropical Atlantic and northeast Brazil climate. **Journal of Climate**, v. 24, n. 13, p. 3402–3422, 2011.
- RODRÍGUEZ-FONSECA, B.; JANICOT, S.; MOHINO, E.; LOSADA, T.; BADER, J.; CAMINADE, C.; CHAUVIN, F.; FONTAINE, B.; GARCÍA-SERRANO, J.; GERVOIS, S.; JOLY, M.; POLO, I.; RUTI, P.; ROUCOU, P.; VOLDOIRE, A. Interannual and decadal SST-forced responses of the West African monsoon. **Atmospheric Science Letters**, v. 12, n. 1, p. 67–74, 2011.
- RODRÍGUEZ-FONSECA, B.; POLO, I.; GARCÍA-SERRANO, J.; LOSADA, T.; MOHINO, E.; MECHOSO, C. R.; KUCHARSKI, F. Are Atlantic Niños enhancing Pacific ENSO events in recent decades? **Geophysical Research Letters**, v. 36, n. 20, 2009.
- ROGERS, J. C.; VAN LOON, H. Spatial variability of sea level pressure and 500 mb height anomalies over the Southern Hemisphere. **Monthly Weather Review**, v. 110, n. 10, p. 1375–1392, 1982.

- RUIZ-BARRADAS, A.; CARTON, J. A.; NIGAM, S. Structure of Interannual-to-decadal climate variability in the Tropical Atlantic sector. **Journal of Climate**, v. 13, n. 18, p. 3285–3297, set. 2000.
- SARAVANAN, R.; CHANG, P. Interaction between Tropical Atlantic Variability and El Niño–Southern oscillation. **Journal of Climate**, v. 13, n. 13, p. 2177–2194, jul. 2000.
- SARAVANAN, R.; CHANG, P. Thermodynamic coupling and predictability of tropical sea surface temperature. In: WANG, C.; XIE, S. P.; CARTON, J. A. (Eds.). **Earth's climate: the ocean-atmosphere interaction**. Washington: AGU, 2004. p. 171–180.
- SCAIFE, A. A.; KNIGHT, J. R.; VALLIS, G. K.; FOLLAND, C. K. A stratospheric influence on the winter NAO and North Atlantic surface climate. **Geophysical Research Letters**, v. 32, n. 18, p. 1–5, 28 set. 2005.
- SCHLESINGER, M. E.; RAMANKUTTY, N. An oscillation in the global climate system of period 65–70 years. **Nature**, v. 367, n. 6465, p. 723–726, 24 fev. 1994.
- SEAGER, R.; KUSHNIR, Y.; CHANG, P.; NAIK, N.; MILLER, J.; HAZELEGER, W. Looking for the role of the ocean in Tropical Atlantic decadal climate variability. **Journal of Climate**, v. 14, n. 5, p. 638–655, 2001.
- SEIDOV, D.; MISHONOV, A.; REAGAN, J.; PARSONS, R. Multidecadal variability and climate shift in the North Atlantic Ocean. **Geophysical Research Letters**, v. 44, n. 10, p. 4985–4993, 2017.
- SERVAIN, J. Simple climatic indices for the tropical Atlantic Ocean. **Journal of Geophysical Research**, v. 98, n. C8, p. 137–146, 1991.
- SERVAIN, J.; WAINER, I.; MCCREARY, J. P.; DESSIER, A. Relationship between the equatorial and meridional modes of climatic variability in the tropical Atlantic. **Geophysical Research Letters**, v. 26, n. 4, p. 485–488, 1999.
- SMIRNOV, D.; VIMONT, D. J. Variability of the Atlantic Meridional Mode during the Atlantic hurricane season. **Journal of Climate**, v. 24, n. 5, p. 1409–1424, 2011.
- SMIRNOV, D.; VIMONT, D. J. Extratropical forcing of tropical atlantic variability during boreal summer and fall. **Journal of Climate**, v. 25, n. 6, p. 2056–2076, 2012.
- STOCKER, T. F.; QIN, D.; PLATTNER, G.-K.; TIGNOR, M.; ALLEN, S. K.; BOSCHUNG, J.; NAUELS, A.; XIA, Y.; BEX, V.; MIDGLEY, P. M. (Eds.). **Climate change 2013: the physical science basis**. Cambridge: Cambridge University Press, 2013. 1535p. ISBN (9781107415324).
- STOUFFER, R. J.; BROCCOLI, A. J.; DELWORTH, T. L.; DIXON, K. W.; GUDGEL, R.; HELD, I.; HEMLER, R.; KNUTSON, T.; LEE, H. C.; SCHWARZKOPF, M. D.; SODEN, B.; SPELMAN, M. J.; WINTON, M.; ZENG, F. GFDL's CM2 global coupled climate models. part IV: idealized climate response. **Journal of Climate**, v. 19, n. 5, p. 723–740, 2006.
- STRAUS, D. M.; SHUKLA, J. Does ENSO force the PNA? **Journal of Climate**, v. 15, n. 17, p. 2340–2358, set. 2002.

- SUN, C.; KUCHARSKI, F.; LI, J.; JIN, F. F.; KANG, I. S.; DING, R. Western tropical Pacific multidecadal variability forced by the Atlantic multidecadal oscillation. **Nature Communications**, v. 8, n. 15998, p. 1–10, 2017.
- SUN, C.; LI, J.; JIN, F. F. A delayed oscillator model for the quasi-periodic multidecadal variability of the NAO. **Climate Dynamics**, v. 45, n. 7–8, p. 2083–2099, 6 out. 2015.
- SUTTON, R. T.; JEWSON, S. P.; ROWELL, D. P. The elements of climate variability in the tropical Atlantic region. **Journal of Climate**, v. 13, n. 1977, p. 3261–3284, 2000.
- TANIMOTO, Y.; XIE, S.-P. Inter-hemispheric decadal variations in SST, surface wind, heat flux and cloud cover over the Atlantic Ocean. **Journal of the Meteorological Society of Japan**, v. 80, n. 5, p. 1199–1219, 2002.
- TARASOVA, T. A.; BARBOSA, H. M. J.; FIGUEROA, S. N. **Incorporation of new solar radiation scheme into CPTEC GCM**. São José dos Campos: INPE, 2006.
- TAYLOR, K. E.; STOUFFER, R. J.; MEEHL, G. A. An overview of CMIP5 and the experiment design. **Bulletin of the American Meteorological Society**, p. 485–498, abr. 2012.
- THOMPSON, D. W. J.; WALLACE, J. M. Annular mode in the extratropical circulation. part I : month-to-month variability. **Journal of Climate**, v. 13, n. 689, p. 1000–1016, 2000.
- TIEDTKE, M. The sensitivity of the time-mean large-scale flow to cumulus convection in the ECMWF model. In: WORKSHOP ON CONVECTION IN LARGE-SCALE NUMERICAL MODELS, 28., 1983. **Proceedings...** ECMWF, 1983.
- TIMMERMAN, A.; LATIF, M. Northern hemispheric interdecadal variability: a coupled air-sea mode. **Journal of Climate**, v. 11, n. 8, p. 1906–1931, ago. 1998.
- TOURRE, Y. M.; PAZ, S.; KUSHNIR, Y.; WHITE, W. B. Low-frequency climate variability in the Atlantic basin during the 20th century. **Atmospheric Science Letters**, v. 11, n. 3, p. 180–185, 10 mar. 2010.
- TOURRE, Y. M.; RAJAGOPALAN, B.; KUSHNIR, Y. Dominant patterns of climate variability in the Atlantic Ocean during the last 136 years. **Journal of Climate**, v. 12, n. 8 PART 1, p. 2285–2299, ago. 1999.
- TRAUTH, M. H.; BOOKHAGEN, B.; MARWAN, N.; STRECKER, M. R. Multiple landslide clusters record quaternary climate changes in the northwestern Argentine Andes. In: PALAEOGEOGRAPHY, PALAEOCLIMATOLOGY, PALAEOECOLOGY, 2003. **Proceedings...** 2003. Disponível em: <http://helios.geog.ucsb.edu/~bodo/pdf/trauth03_landslide_clusters.pdf>. Acesso em: 15 maio. 2018
- TREND-STAD, M.; PRELL, W. L. Sea surface temperature at the last glacial maximum: a reconstruction using the modern analog technique. **Paleoceanography**, v. 17, n. 4, p. 1–18, 1 dez. 2002.

TRIPATI, A. K.; ROBERTS, C. D.; EAGLE, R. A. Coupling of CO₂ and ice sheet stability over major climate transitions of the last 20 million years. **Science**, v. 326, n. 5958, p. 1394–1397, 4 dez. 2009.

UNITED NATIONS. **World Population 2015**. Disponível em: https://esa.un.org/unpd/wpp/Publications/Files/World_Population_2015_Wallchart.pdf

VEIGA, S. M. F.; NOBRE, ; GIAROLLA, E.; BAPTISTA JÚNIOR, M.; MARQUEZ, A. L.; FIGUEROA, S. N.; BONATTI, J. P.; KUBOTA, P. Y.; NOBRE, C. A. The Brazilian Earth System Model version 2.5: evaluation of its CMIP5 historical simulation. **Geoscientific Model Development Discussions**, 2018. DOI:<10.5194/gmd-2018-91>. Disponível em:<<http://dx.doi.org/10.5194/gmd-2018-91>>.

VENEGAS, S. **Statistical methods for signal detection in climate**. Denmark: University of Copenhagen, 2001. (Technical Report, Danish Center for Earth System Science, 2.).

VIMONT, D. J. The contribution of the interannual ENSO cycle to the spatial pattern of decadal ENSO-like variability. **Journal of Climate**, v. 18, n. 12, p. 2080–2092, 2005.

VIMONT, D. J. Transient growth of thermodynamically coupled variations in the tropics under an equatorially symmetric mean state. **Journal of Climate**, v. 23, n. 21, p. 5771–5789, 2010.

VIMONT, D. J.; KOSSIN, J. P. The Atlantic Meridional mode and hurricane activity. **Geophysical Research Letters**, v. 34, n. 7, p. 1–5, 2007.

WAINER, I.; SERVAIN, J.; CLAUZET, G. Is the decadal variability in the tropical Atlantic a precursor to the NAO? **Annales Geophysicae**, v. 26, n. 12, p. 4075–4080, 2008.

WAINER, I.; SOARES, J. North northeast Brazil rainfall and its decadal-scale relationship to wind stress and sea surface temperature. **Geophysical Research Letters**, v. 24, n. 3, p. 277–280, fev. 1997.

WALLACE, J. M.; GUTZLER, D. S. Teleconnections in the geopotential height field during the Northern Hemisphere winter. **Monthly Weather Review**, v. 109, p. 784–812, abr. 1981.

WANG, C. ENSO, Atlantic climate variability, and the walker and hadley circulations. In: DIAZ, H.F.; BRADLEY, R.S. (Eds.). **The hadley circulation: present, past and future**. Dordrecht: Springer, 2004. p. 173–202.

WANG, C.; KUCHARSKI, F.; BARIMALALA, R.; BRACCO, A. Teleconnections of the tropical Atlantic to the tropical Indian and Pacific Oceans: a review of recent findings. **Meteorologische Zeitschrift**, v. 18, n. 4, p. 445–454, 2009.

WANG, S.; HUANG, J.; HE, Y.; GUAN, Y. Combined effects of the Pacific decadal oscillation and El Niño-Southern oscillation on global land dry-wet changes. **Scientific Reports**, v. 4, n. 1, p. 6651, 17 maio 2014.

- WANG, X.; LI, J.; SUN, C.; LIU, T. NAO and its relationship with the Northern Hemisphere mean surface temperature in CMIP5 simulations. **Journal of Geophysical Research**, v. 122, n. 8, p. 4202–4227, 27 abr. 2017.
- WANNER, H.; BRÖNNIMANN, S.; CASTY, C.; LUTERBACHER, J.; SCHMUTZ, C.; DAVID, B. North Atlantic oscillation: concepts and studies. **Surveys in Geophysics**, v. 22, n. 1984, p. 321–382, 2001.
- WEAVER, A. J.; SEDLÁČEK, J.; EBY, M.; ALEXANDER, K.; CRESPI, E.; FICHEFET, T.; PHILIPPON-BERTHIER, G.; JOOS, F.; KAWAMIY, M.; MATSUMOTO, K.; STEINACHER, M.; TACHIIRI, K.; TOKOS, K.; YOSHIMORI, M.; ZICKFELD, K. Stability of the Atlantic meridional overturning circulation: a model intercomparison. **Geophysical Research Letters**, v. 39, n. 20, 28 out. 2012.
- WEN, N.; FRANKIGNOUL, C.; GASTINEAU, G. Active AMOC–NAO coupling in the IPSL-CM5A-MR climate model. **Climate Dynamics**, v. 47, n. 7–8, p. 2105–2119, 2016.
- WILKIS, D. S. **Statistical methods in the atmospheric sciences**. 3. ed. [S.l.]: Academic Press, 2011. 704 p. ISBN(9780127519661).
- WINTON, M. A reformulated three-layer sea ice model. **Journal of Atmospheric and Oceanic Technology**, v. 17, n. 4, p. 525–531, abr. 2000.
- WU, L.; HE, F.; LIU, Z.; LI, C. Atmospheric teleconnections of tropical atlantic variability: interhemispheric, tropical-extratropical, and cross-basin interactions. **Journal of Climate**, v. 20, n. 5, p. 856–870, 2007.
- WU, L.; LIU, Z. Is Tropical Atlantic variability driven by the North Atlantic oscillation? **Geophysical Research Letters**, v. 29, n. 13, p. 29–32, 2002.
- WU, L.; ZHANG, Q.; LIU, Z. Toward understanding tropical Atlantic variability using coupled modeling surgery. **Earth Climate: Ocean-Atmosphere Interaction and Climate Variability**, v. 147, p. 157–170, 2004.
- WU, X.; MAO, J. Interdecadal variability of early summer monsoon rainfall over South China in association with the Pacific Decadal Oscillation. **International Journal of Climatology**, v.37, n.2, p.706-721, abr. 2016.
- WU, Z.; LI, J.; JIANG, Z.; HE, J.; ZHU, X. Possible effects of the North Atlantic Oscillation on the strengthening relationship between the East Asian Summer monsoon and ENSO. **International Journal of Climatology**, v. 32, n. 5, p. 794–800, 2012.
- XIE, S.-P. A dynamic ocean: atmosphere model of the Tropical Atlantic decadal variability. **Journal of Climate**, v. 12, n. 1, p. 64–71, 1999.
- XIE, S.-P.; TANIMOTO, Y. A pan-Atlantic decadal climate oscillation. **Geophysical Research Letters**, v. 25, n. 15, p. 2185–2155, 1998.
- XIE, S. P.; CARTON, J. A. Tropical Atlantic variability: patterns, mechanisms, and impacts. **Geophysical Monograph Series**, v. 147, p. 121–142, 2004.

- XUE, Y.; SELLERS, P.; KINTER, J.; SHUKLA, J. A simplified biosphere model for global climate studies. **Journal Of Climate**, v.4, p.345-364, mar. 1991.
- YANG, C.; MASINA, S.; STORTO, A. Historical ocean reanalyses (1900–2010) using different data assimilation strategies. **Quarterly Journal of the Royal Meteorological Society**, v. 143, n. 702, p. 479–493, jan. 2017.
- YANG, Y.; XIE, S. P.; WU, L.; KOSAKA, Y.; LI, J. ENSO forced and local variability of North Tropical Atlantic SST: model simulations and biases. **Climate Dynamics**, p. 1–14, 2017.
- YU, B.; ZWIERS, F. W. The impact of combined ENSO and PDO on the PNA climate: A 1,000-year climate modeling study. **Climate Dynamics**, v. 29, n. 7–8, p. 837–851, out. 2007.
- YU, R.; ZHOU, T. Impacts of winter-NAO on March cooling trends over subtropical Eurasia continent in the recent half century. **Geophysical Research Letters**, v. 31, n. 12, p. 3–6, 2004.
- YUAN, X.; YONEKURA, E. Decadal variability in the Southern Hemisphere. **Journal of Geophysical Research**, v. 116, p. 1–12, 2011.
- YUKIMOTO, S.; ENDOH, M.; KITAMURA, Y.; KITO, A.; MOTOI, T.; NODA, A. ENSO-like interdecadal variability in the Pacific Ocean as simulated in a coupled general circulation model. **Journal of Geophysical Research: Oceans**, v. 105, n. C6, p. 13945–13963, jun. 2000.
- ZEBIK, S. E. Air–Sea Interaction in the Equatorial Atlantic Region. **Journal of Climate**, v.6, p.1567-1586, 1993.
- ZENG, N.; NEELIN, J. D.; LAU, K.-M.; TUCKER, C. J. Enhancement of interdecadal climate variability in the Sahel by vegetation interaction. **Science**, v. 286, n. 5444, p. 1537–1540, 1999.
- ZHANG, L.; MA, H.; WU, L. Dynamics and mechanisms of decadal variability of the Pacific-South America mode over the 20th century. **Climate Dynamics**, v. 46, n. 11–12, p. 3657–3667, jun. 2016.
- ZHANG, L.; WANG, C. Multidecadal North Atlantic sea surface temperature and Atlantic meridional overturning circulation variability in CMIP5 historical simulations. **Journal of Geophysical Research: Oceans**, v. 118, n. 10, p. 5772–5791, 1 out. 2013.
- ZHANG, R. Coherent surface-subsurface fingerprint of the Atlantic meridional overturning circulation. **Geophysical Research Letters**, v. 35, n. 20, p. L20705, 24 out. 2008.
- ZHANG, W.; VECCHI, G. A.; VILLARINI, G.; MURAKAMI, H.; ROSATI, A.; YANG, X.; JIA, L.; ZENG, F. Modulation of western North Pacific tropical cyclone activity by the Atlantic Meridional Mode. **Climate Dynamics**, v. 48, n. 1–2, p. 631–647, jan. 2017.
- ZHANG, Y.; WALLACE, J. M.; BATTISTI, D. S. ENSO-like interdecadal variability: 1900-93. **Journal of Climate**, v. 10, n. 5, p. 1004–1020, maio 1997.

ZHENG, F.; LI, J.; CLARK, R. T.; NNAMCHI, H. C. Simulation and projection of the Southern Hemisphere annular mode in CMIP5 models. **Journal of Climate**, v. 26, n. 24, p. 9860–9879, 2013.

ZHU, J.; HUANG, B.; WU, Z. The role of ocean dynamics in the interaction between the Atlantic Meridional and Equatorial modes. **Journal of Climate**, v. 25, n. 10, p. 3583–3598, maio 2012.